

**Study of fully hadronic $t\bar{t}$ decays and their
separation from QCD multijet background
events in the first year of the ATLAS
experiment**

Dissertation der Fakultät für Physik
der
Ludwig-Maximilians-Universität München

vorgelegt von
Marion Lambacher
geboren in Pfarrkirchen

München, den 27. Juli 2007

1. Gutachter: Prof. Dr. Otmar Biebel
2. Gutachter: Prof. Dr. Martin Faessler

Tag der mündlichen Prüfung: 26.10.2007

*Vultus fortunae variatur imagine lunae crescit,
decrescit constans persistere nescit.*

*To my husband
and in loving memory to my mom*

Abstract

The LHC is a top quark factory producing $t\bar{t}$ events at a cross section of 833 pb in NLO. This corresponds to about $8 \cdot 10^6$ $t\bar{t}$ events in the first nominal year of the LHC at the initial low integrated luminosity of 10 fb^{-1} being delivered. Approximately 44 % of the $t\bar{t}$ pairs decay hadronically into six jets. QCD multijet events with four to six final state partons are the main background to these $t\bar{t}$ events with a cross section many orders of magnitude above the $t\bar{t}$ multijet cross section.

This study deals with the generation of fully hadronic $t\bar{t}$ events and QCD multijet events with up to six final state partons and their measurement in the ATLAS detector via fast parameterized simulation. The characteristics of the QCD events with respect to the $t\bar{t}$ signals are discussed and a cut-based selection for the separation of the $t\bar{t}$ events from the QCD background is introduced. The presented analysis is designed to use the physical and technical information available in the start-up period of the LHC. The extraction of the $t\bar{t}$ events results in more than 3000 remaining fully hadronic $t\bar{t}$ events which can be separated from the QCD multijet background in the first year of the LHC. This analysis also includes the reconstruction of the top-mass peak from fully hadronic $t\bar{t}$ events in the start-up period of the LHC and gives an estimate of the relative statistical uncertainty for the determination of the $t\bar{t}$ production cross section of approximately 4 % at an integrated luminosity of 10 fb^{-1} .

Zusammenfassung

Das LHC ist eine top quark Fabrik, in der $t\bar{t}$ Ereignisse mit einem Wirkungsquerschnitt von 833 pb in NLO erzeugt werden. Dies entspricht ca. $8 \cdot 10^6$ $t\bar{t}$ Ereignissen im ersten nominalen Jahr des LHC bei einer noch niedrigen integrierten Luminosität von 10 fb^{-1} . Rund 44 % dieser top-antitop Paare zerfallen rein hadronisch in sechs Jets. QCD multijet Ereignisse mit vier bis sechs Partonen im Endzustand stellen den Hauptuntergrund für diesen $t\bar{t}$ Zerfallskanal dar mit einem um mehrere Größenordnungen höheren Wirkungsquerschnitt.

Diese Studie befasst sich mit der Generierung von rein hadronischen $t\bar{t}$ Ereignissen sowie von QCD multijet Ereignissen mit bis zu sechs Partonen im Endzustand und ihrer Messung im ATLAS Detektor mittels schneller, parametrisierter Simulation. Es werden die charakteristischen Eigenschaften der QCD Ereignisse in Hinblick auf die hadronischen $t\bar{t}$ Ereignisse diskutiert und eine Selektion mit Schnitten zur Abtrennung der top Signale von den QCD Ereignissen vorgestellt, die auf die verfügbare Detektorinformation in der Startphase des LHC abgestimmt ist.

Die Separierung der $t\bar{t}$ Ereignisse resultiert in einer Anzahl von mehr als 3000 verbleibenden rein hadronischen $t\bar{t}$ Paaren, die im ersten Jahr des LHC vom QCD Untergrund separiert werden können. Diese Arbeit behandelt ebenfalls die Rekonstruktion des Topmassen Peaks aus rein hadronischen $t\bar{t}$ Ereignissen im ersten Jahr des LHC und gibt eine Abschätzung für die zu erwartende relative statistische Unsicherheit bei der Bestimmung des Produktions-Wirkungsquerschnitts der top Ereignisse an, die bei einer integrierten Luminosität von 10 fb^{-1} bei etwa 4 % liegt.

Contents

1	Introduction	1
2	Theory	3
2.1	The Standard Model of elementary particle physics	3
2.2	Quantum Chromo Dynamics	5
2.2.1	The colour-charge of the strong interaction	5
2.2.2	The strength of the strong interaction	6
2.3	Hadronization	8
2.4	The structure of the proton	10
2.5	General properties of the top quark	11
2.5.1	Top quark production	12
2.5.2	Top quark decay	13
2.5.3	Particularities of the fully hadronic decay mode	14
3	LHC and the ATLAS detector	17
3.1	The Large Hadron Collider	17
3.2	Design and functionality of the ATLAS detector	18
3.3	The electromagnetic and the hadronic calorimeter	20
4	Characterization of the background to fully hadronic $t\bar{t}$ events	23
4.1	The QCD multijet background	23
4.2	W and Z pair production	25
4.3	τ lepton decays	27
5	The k_T algorithm	29
5.1	Production of jets	29
5.2	Jet reconstruction with the k_T algorithm	31
5.2.1	Jet resolution variables	31
5.2.2	The recombination scheme	32
5.2.3	The reconstruction mode	32
5.2.4	The reconstruction in exclusive mode	33
5.3	Comparison between k_T and Cone algorithm	34
6	Monte Carlo generators	39
6.1	ALPGEN	39
6.1.1	Choice of the subprocess	39
6.1.2	Operational mode and input structure	42

6.1.3	Jet – parton matching	43
6.2	PYTHIA 6.2	45
6.2.1	Simulation of $t\bar{t}$ multijet events	45
6.2.2	Reprocessing of QCD multijet background events	48
6.3	Athena - an ATLAS framework	49
6.3.1	Transformation of PYTHIA events for further processing in Athena	50
6.3.2	ATLFAST - a software package of the Athena framework	50
6.3.3	AOD analysis with AnalysisSkeleton	52
6.3.4	Athena Full Simulation	52
6.4	Jet reconstruction algorithms in PYTHIA 6.2 and Athena	53
7	Fully hadronic $t\bar{t}$ events and QCD multijet background events	55
7.1	Modified subroutine UPVETO	55
7.2	Fully hadronic $t\bar{t}$ events and QCD multijet background events in Athena	57
7.2.1	Determination of the cut-off parameter d_{Cut}	57
7.2.2	Produced signal and background events	60
7.2.3	General properties of signal and background events	61
7.2.4	Comparison of fully hadronic $t\bar{t}$ events from full simulation and fast simulation	70
7.3	Analysis of $t\bar{t}$ and background events at generator level	73
7.3.1	Determination of the cut-off parameter d_{Cut}	74
7.3.2	Pile-up studies	75
8	Separation of fully hadronic $t\bar{t}$ events from the QCD background	83
8.1	Separation by means of a cut analysis	83
8.1.1	Interpretation of the results from the cut analysis	100
8.2	Separation by the determination of the top-mass peak	101
8.2.1	Interpretation of the top-mass peak results	112
9	Summary	115
A	Limitation of the phase space for the production of $t\bar{t}$ events	117
B	QCD multijet events reconstructed with the Cone Algorithm	121
C	Pulser test of ATLAS BOS-MDT muon chambers	127
C.1	Abstract	127
C.2	Introduction	127
C.3	Setup of the pulser test	128
C.4	Measurements and results	128
C.4.1	Attenuation distributions of mezzanine cards and single channels	128
C.4.2	Cross-talk between tubes	130
C.4.3	Pulser test on single tubes	131
C.4.4	Comparison between pulser test at chambers in the cosmic ray measurement facility and in the preparation room	134
C.5	Comparison to simulation	135
C.6	Summary and conclusion	139

List of images	141
List of tables	147
Bibliography	149
Acknowledgments	155
Curriculum Vitae	157

Chapter 1

Introduction

Elementary particle physics explains the structure of matter and characterizes the known particles with their fundamental interactions. Despite its successful description of the observed phenomena, there are still many open questions and therefore, particle physics and with it the Standard Model is under continuous research and development. New approaches which reach beyond the current limits of the Standard Model of today are constantly evolved and studied. Most extensions of the Standard Model predict particles which could not be observed so far as they have a very large mass. Therefore, the achievement of even higher collision energies is one of the main goals of modern particle physics as it offers the opportunity to search for new (heavy) particles – like the Higgs Boson – which have not been observed but only predicted so far.

The Large Hadron Collider and with it the ATLAS experiment herald a completely new era for particle physics. With the ability to reach collision energies of up to 14 TeV, recent technical developments and new analyzing techniques it will be possible to measure and analyze the properties of the known particles, like the top quark, and their decays with unprecedented accuracy and to discover new physics beyond the Standard Model.

However, the large energy reached at the LHC causes the events, such as top quark multijet and QCD multijet events as studied in this thesis, to be produced with a boost. Hence, a completely new situation is faced in contrast to the studies at the Tevatron at Fermilab where the collision energy is much smaller and the top quarks are produced almost in their rest system. As a consequence, new analysis methods have to be developed to accommodate the new situation encountered at the LHC.

Fully hadronic $t\bar{t}$ events and QCD multijet events have an almost identical final state topology. However, QCD events have a much larger production cross section than the $t\bar{t}$ events and therefore, it is a tricky task to separate the desired $t\bar{t}$ events from the QCD background. This thesis describes the development of an analysis for $t\bar{t}$ events and their separation from QCD multijet background events which can be applied already during the early phase of LHC data taking. In this start-up period the detector will not be well understood and quite a few components may not perform perfectly. Thus, a complete analysis and understanding of the characteristics of fully hadronic $t\bar{t}$ events by accessing all the technical features of the detector, like a proper alignment of its components or a reliable energy calibration of the calorimeters, will probably not be

realizable in the first year of the LHC. This study accommodates this fact, using the technical and physical information available in this start-up period.

The underlying theoretical aspects of this analysis, among them an introduction in the characteristics of the top quark, are explained in Chapter 2. An overview of the LHC and the ATLAS detector, above all the calorimeter which is the most important detector component for the study of fully hadronic $t\bar{t}$ and QCD multijet events, is given in Chapter 3. Chapter 4 outlines, in addition to the studied QCD multijet background, further possible background events to the fully hadronic $t\bar{t}$ signals. The software used for generating and processing the events of interest is described in Chapter 5 and 6. In Chapter 7 the information accessible in the first year of the LHC for the study of $t\bar{t}$ and QCD multijet background events is used for analyzing the properties of the regarded events and for finding first "differences" between the signal and the background. The knowledge gained serves as input for the separation of the fully hadronic $t\bar{t}$ events from the QCD background, which is presented in Chapter 8. Finally, Appendix C presents a newly developed pulser test to check the functionality of the muon chambers which were calibrated at the cosmic ray measurement facility of the LMU.

Chapter 2

Theory

The theoretical aspects underlying this thesis can all be described by the Standard Model of elementary particle physics, a theoretical framework characterizing the particles and their fundamental interactions. In this regard the cornerstones of this analysis are the physics of the top quark as well as the strong interaction, the Quantum Chromo Dynamics (QCD), which rules the fully hadronic final state of a $t\bar{t}$ signal event and also its main (QCD multijet) background.

Additionally, in the following pages the attention will be turned to the hadronization of quarks and gluons into colour-neutral composite particles which constitute the basic elements of jet physics and jet reconstruction (see Chapter 5).

2.1 The Standard Model of elementary particle physics

The Standard Model comprises the twelve fermions (particles with spin $\frac{1}{2}$), as outlined in Table 2.1, and the unified theory of the electroweak interaction¹ as well as the strong interaction (QCD) which describe how these particles interact. Gravity is not included in the Standard Model.

The fermions are classified into six leptons and six quarks which can be grouped in three generations of two leptons and two quarks each plus the corresponding antiparticles, respectively. The antiparticles have the same features as the particles but carry opposite charges, quantum numbers and colour [1]. The stable matter, which forms the visible universe, consists of fermions of the first generation, exclusively [2]. The decisive difference in the three generations of fermions is based on the mass of the constituents. The top quark with a mass of about $m_t = 174$ GeV [3]² belongs to the third generation. The next lightest quark is the b -quark with a mass of about $m_b = 4.2$ GeV [3]. Because of its heaviness the top has an exceptional position among the elementary particles.

The interaction of the elementary particles is characterized by the twelve force-carrying gauge bosons which are spin 1 particles. They differ fundamentally from the quarks and leptons. The range of the interactions is coupled to the mass of the corresponding gauge bosons³ (see Table 2.2). For the electromagnetic force it is the

¹The unified theory includes therefore the weak and the electromagnetic force.

²Thus, the top quark weights more than 300000 times as much as an electron.

³This applies not for the gauge bosons of the strong interactions, the gluons, see Section 2.2.

massless photon, which leads to an infinite range of this interaction. For the weak force (range $\approx 10^{-18}$ m) there are the W^+ and the W^- boson ($m_{W^\pm} = 81$ GeV) as well as the Z boson ($m_Z = 90$ GeV). The transmitters of the strong force are eight massless gluons. Although their mass equals to zero, the range of the strong interaction is not infinite due to the self-interaction of the gluons (see Section 2.2.1).

Fermions		
Leptons		
$\begin{pmatrix} \nu_e \\ e^- \end{pmatrix}_L$	$\begin{pmatrix} \nu_\mu \\ \mu^- \end{pmatrix}_L$	$\begin{pmatrix} \nu_\tau \\ \tau^- \end{pmatrix}_L$
e^-_R	μ^-_R	τ^-_R
Quarks		
$\begin{pmatrix} u \\ d' \end{pmatrix}_L$	$\begin{pmatrix} c \\ s' \end{pmatrix}_L$	$\begin{pmatrix} t \\ b' \end{pmatrix}_L$
u_R d'_R	c_R s'_R	t_R b'_R

Table 2.1: The three particle generations in the Standard Model of elementary particle physics. L is for the left-handed particles (momentum p of the particle is anti-parallel to its spin), R stands for the right-handed particles (momentum is parallel to the spin). The prime marks particles which are a mixture of mass eigen-states. Only the left-handed particles participate in the weak interaction.

Interaction	Couples to	Gauge boson	Mass [GeV/c^2]	Range [m]
Strong	Colour	8 gluons	0	$\approx 10^{-15}$
Electromagnetic	Electrical charge	Photon	0	∞
Weak	Weak charge	W^\pm, Z	$\approx 10^2$	$\approx 10^{-18}$

Table 2.2: Interactions in the Standard Model of elementary particle physics.

However, the Standard Model as described above does not explain a very important property of the particles, their mass. For being able to explain the masses the theory predicts the existence of another scalar particle, the Higgs Boson (H) named after the Scottish physicist Peter W. Higgs, who proposed the so-called Higgs-mechanism corresponding to a spontaneous symmetry breaking of the electroweak gauge symmetry, noted below. Based on the principle of the symmetry breaking the Higgs mechanism

leads to the masses of the bosons⁴. The masses of the fermions can then be explained by *Yukawa couplings* [5, 6] to the field of the Higgs boson (Higgs field).

The Higgs boson is expected to have no intrinsic spin nor electrical charge. Up to now the Higgs has not been observed yet, but a lower mass limit of 114.4 GeV could be estimated at LEP2 [7].

The theory of the Standard Model bases upon the principle of local gauge invariance. The solutions of the Lagrangian are invariant under local transformations of the corresponding symmetry groups. This invariance corresponds to a symmetry and causes the conservation of the quantum numbers.

The symmetry group of the strong force is the $SU(3)_C$, where C corresponds to colour, the charge of the particles in the strong interaction. The electroweak force is defined by the $SU(2)_L$ symmetry group and the group of the weak hypercharge $U(1)_Y$. Thus, all interactions in the Standard Model are specified via the $U(1)_Y \otimes SU(2)_L \otimes SU(3)_C$ gauge group.

2.2 Quantum Chromo Dynamics

The QCD is the quantumfield-theoretical description of the strong interaction of quarks⁵ and gluons. In principle, the QCD is deduced from the Quantum Electro Dynamics (QED), the theory of electrically charged particles. Though, it is much more complicated, as the strong interaction comprises three different types of charge which are conventionally denoted as the colours red (r), blue (b) and green (g) with the corresponding anticolours (\bar{r} , \bar{b} , \bar{g}), carried by antiquarks.

2.2.1 The colour-charge of the strong interaction

The QED introduces only one single kind of charge (electrical charge ± 1), the corresponding gauge boson is electrically neutral, there is no direct interaction between photons. The QCD, however, includes the three different colour-charges, as mentioned above, and eight gauge bosons carrying a combination of colour and anticolour. This leads to the fact that gluons interact among each other in addition to their coupling to the colour-charge of the quarks.

Due to the underlying $SU(3)_C$ group-theory the 3×3 colour combinations constitute a colour octet and a singlet. All colour states derive from the octet, corresponding the octet of gluons [1] which leads to the eight gauge bosons of the strong interaction. Table 2.3 shows a possible combination of these colour-states.

colour-octet								
r^-g	\bar{b}	$g\bar{b}$	g^-r	b^-r	$b^-g\sqrt{\frac{1}{2}}$	$(r^-r - g^-g)$	$\sqrt{\frac{1}{6}}$	$(r^-r + g^-g - 2\bar{b}\bar{b})$

Table 2.3: States of the colour-octet. The states form a system of so-called base-states.

⁴A detailed description of the Higgs mechanism can be found in [4].

⁵Of the twelve fermions, which are described in the Standard Model, only the quarks can strongly interact as they are the only fermions which carry colour-charge.

The colour-singlet

$$\sqrt{\frac{1}{3}} (\bar{r}\bar{r} + g\bar{g} + b\bar{b})$$

is symmetrically composed of the three colours and anticolours. It is invariant under rotations in the colour space. Thus, it is colour-neutral and does not couple to colour-charged particles [1].

Figure 2.1 shows the fundamental Feynman diagrams of the strong interaction which emphasize that, besides from the emission and absorption of gluons, the QCD also includes the self-interaction of gluons.

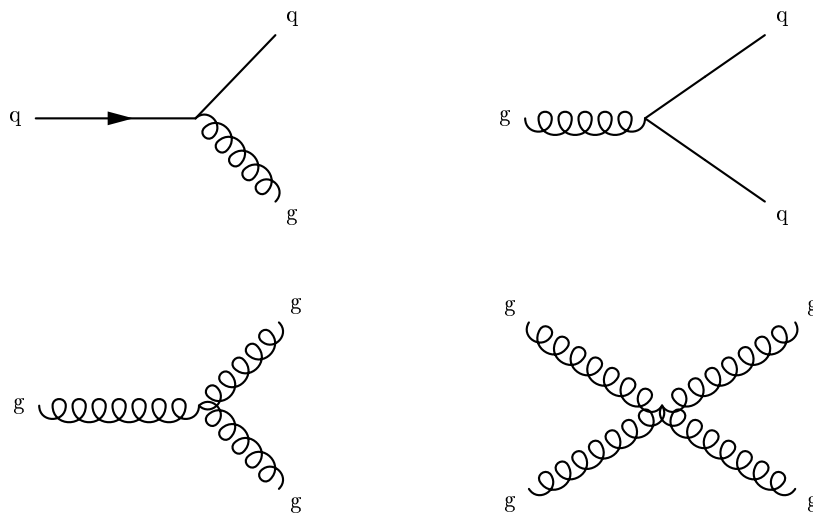


Figure 2.1: Fundamental interaction Feynman diagrams of the QCD. Top left: Emission of a gluon. Top right: Splitting up of a gluon into a pair of quarks. Bottom left: Self-coupling of three gluons. Bottom right: Self-coupling of four gluons.

2.2.2 The strength of the strong interaction

Quarks or in general colour-charged particles cannot be observed individually but they are confined by the strong interaction to form colour-neutral hadrons. This is the concept of the *confinement* [8]. The colour-neutral particles enclosing the quarks and gluons are the mesons, which comprise a pair of quark and antiquark⁶, and the baryons, which are composed of three quarks⁷.

The strength of the strong interaction is characterized by the strong coupling constant

$$\alpha_s = \frac{g_s^2}{4\pi}$$

with g_s being the colour-charge.

α_s is not a real constant but it varies subject to the distance from the charge source.

⁶An example for a meson is the π^+ composed of $u\bar{d}$.

⁷The probably best known baryons are the proton (uud) and the neutron (ddu).

This can be ascribed to the behaviour of the vacuum in the presence of colour-charged particles. The vacuum is not empty but has a very complicated structure. Therefore, it may be polarized by the colour-charge of the quarks and gluons (vacuum polarization) and acts similar to a paramagneticum for colour-charges [9]. This way the bare charge gets anti-screened and the visible charge becomes dependent on the energy and the distance of the particles.

Consequently, for high p_T -transfers⁸ Q^2 and thus, for very small distances to the charge source the interaction α_s becomes small, as exemplified in Figure 2.2:

$$\lim_{Q^2 \rightarrow \infty} \alpha_s(Q^2) \rightarrow 0$$

This is the *asymptotic freedom* which is the regime of perturbation theory calculations applying Feynman diagrams. The asymptotic freedom implies that at small distances quarks can be regarded as "quasi-free", barely-interacting particles.

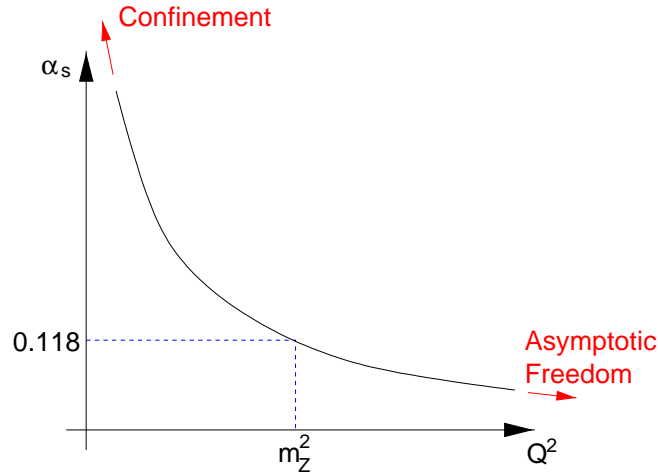


Figure 2.2: Running of the strong coupling constant α_s in dependency of the energy scale Q^2 .

For decreasing transferred Q^2 (increasing distance between the particles) the potential of interaction between colour-charged particles rises to infinity (see Figure 2.2):

$$\lim_{Q^2 \rightarrow \Lambda_{QCD}} \alpha_s(Q^2) \rightarrow \infty$$

Λ_{QCD} is the only free parameter of the QCD with a value of a few hundred MeV. This is the region of the quark confinement based on the self-interaction of the gluons [1]. When the particles separate more and more the interacting gluon fields develop strings of colour-charge. As a consequence, the energy density between the particles increases more and more till the density is high enough and $q\bar{q}$ pairs and gluons are created out of the vacuum⁹. These particles interact further and are finally enclosed in

⁸ Q^2 is the energy scale of an event (" p_T -transfer").

⁹At this point it is energetically more favourable to produce new colour-charged particles out of the vacuum than to let the quarks further separate from each other.

hadrons (confinement).

By comparison, when two electrically-charged particles separate, the electric fields between them decrease rapidly, which prompts for example electrons being unbound from nuclei.

2.3 Hadronization

Due to the colour confinement quarks and gluons cannot exist individually but form colour-neutral hadrons, as outlined in the previous section. The process of forming colour-neutral particles is called *hadronization*. Thereby, the quarks and gluons¹⁰ join with the colour-charged particles which have been created out of the vacuum, as it is illustrated in Figure 2.3.

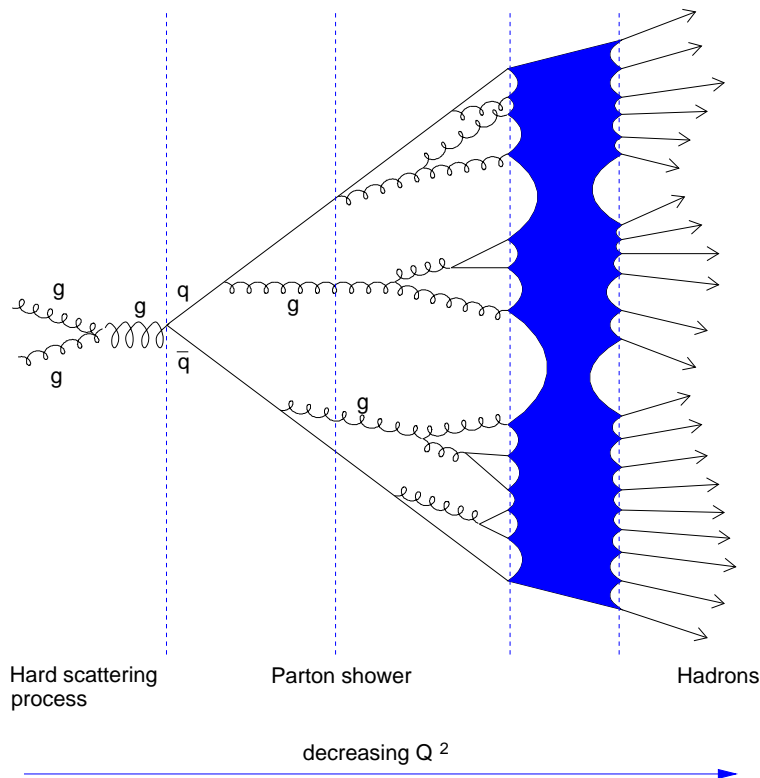


Figure 2.3: Hadronization of quarks and gluons into colour-neutral hadrons.

The hadronization is a long-distance process and implies only small momenta transfers. Thus, the flow of the quantum numbers and the energy transfers at hadron level¹¹ are supposed to result from the flows at parton level [10] (*local parton-hadron duality* [11]).

¹⁰Quarks and gluons are also denoted as "partons".

¹¹Hadron level denotes that the quarks and gluons are enclosed in stable particles (hadrons). Thus, it is the state of quarks and gluons (partons) after hadronization has taken place.

Up to now, an explicit calculation of the hadronization is not possible as the involved confinement cannot be described by means of perturbation theory. Instead, one implements the process of hadronization via complex phenomenological models.

Two such models are frequently used for the description of the hadronization:

- **The Cluster model:** Due to the "colour-interaction" (colour flow) between the colour-charged particles, the colour-charged quarks and gluons form colour-neutral clusters, as denoted in Figure 2.4. These clusters are comparable to very massive colour-neutral particles which decay into the known hadrons of elementary particle physics.

More information about the Cluster model of hadronization can be found in [10].

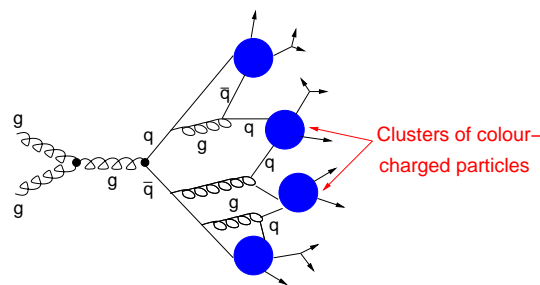


Figure 2.4: Cluster model of hadronization: Due to the colour flow the colour-charged particles bunch to neutral clusters.

- **The (Lund) String model:** This model regards the colour-charged particles as being connected by field lines which are attracted by the gluon self-interaction [12]. Thus, a colour string forms between the particles, as shown in Figure 2.5, with a string constant of $\kappa \approx 1 \frac{\text{GeV}}{\text{fm}}$. When the particles separate from each other the colour string is stretched. If the energy stored in the string is sufficiently high, the string may break by creating a quark-antiquark pair. When the energy becomes insufficient the remaining strings are colour-neutral hadrons [9]. The string model (see also [10]) is used for the description of the hadronization in the PYTHIA [13] Monte Carlo events considered for this analysis (see Chapter 6).

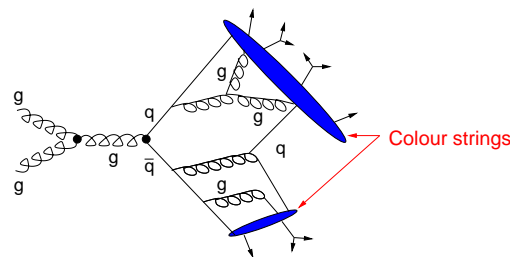


Figure 2.5: String model of hadronization: A colour string is formed between quarks and antiquarks which breaks when separating the particles from each other.

2.4 The structure of the proton

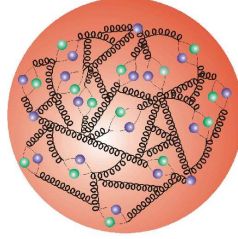


Figure 2.6: Composition of the proton of partons (quarks and gluons). [14]

The composition of the nucleons, i.e. proton and neutron (see Figure 2.6), depicted in Feynman's *parton model* [15, 16], is explained by structure functions, as shown in Figure 2.7.

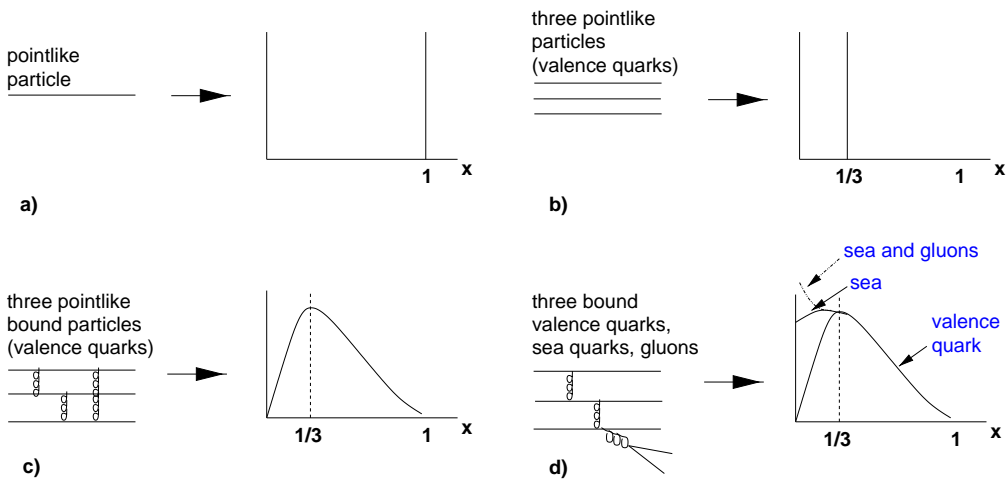


Figure 2.7: Structure functions: a) Structure function of a pointlike particle. b) Structure function of a particle consisting of three pointlike constituents. c) Structure function of a particle consisting of three bound quarks. d) Structure function of the proton which consists of three *valence quarks* (uud), *sea quarks* and *gluons*. The variable x denotes the fraction of the proton's momentum, carried by the partons.

In this context the structure function¹² $F_2(x)$ defines the exact structure of the proton [17]. Considering the fact that a proton consists of pointlike particles, its structure function can be regarded as overlay of the partons (quarks and gluons) i with charge e_i and fraction x of the proton's momentum [9], respectively:

$$F_2(x) = \sum_i e_i^2 x f_i(x) \quad (2.1)$$

¹²Due to longitudinal and transverse polarization one distinguishes the two functions $F_1(x)$ and $F_2(x)$ [9] which are related by the Callan-Cross relation $2xF_1(x) = F_2(x)$.

Thereby, $f_i(x)$ is the momentum distribution of the i -th parton, corresponding to the probability that the regarded parton carries the fraction x of the proton's momentum. $f_i(x)$ is denoted *parton density function (PDF)*.

Figure 2.8 left illustrates the factorization of a proton-proton scattering process with PDF-fraction f and hard collision σ_{ij} : Two partons (with momentum fraction x_1 and x_2 , respectively) interact strongly. The momentum distribution of the partons is given by the corresponding parton density function $f(x_1)$ and $f(x_2)$, accordingly.

A certain parton distribution function for the different constituents of the proton at a given Q^2 is denoted in Figure 2.8 right. In this regard x indicates the partons' particular fraction of the longitudinal momentum of the proton. For small x the gluons prevail, whereas with rising x the fraction of up and down quarks in the proton increases up to maximum for the up quarks at about 0.25.

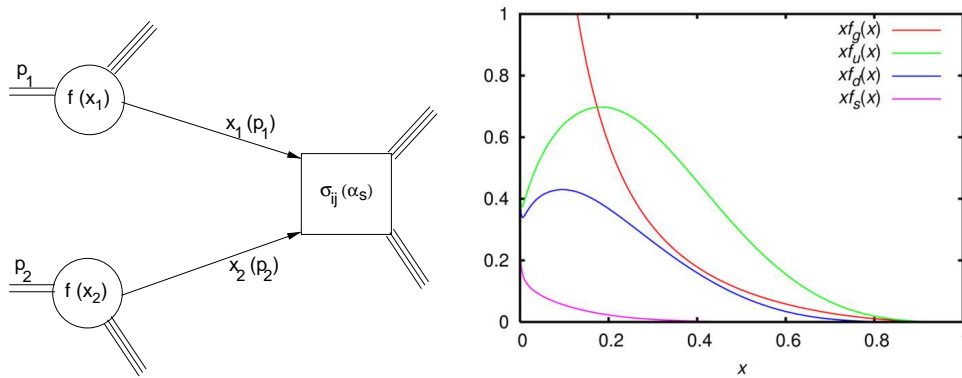


Figure 2.8: Left: Graphical illustration of a proton-proton scattering process in PDF-fraction f . Right: CTEQ6 [18] parton distribution functions for $Q^2 = 2$ GeV plotted for the longitudinal momentum fraction x . The red line indicates the PDF for gluons, the green line for up quarks. The down quarks are illustrated in blue and the strange quarks in violet.

The PDF finally serves as input for the calculation of the partons' luminosities for the hard collision [19]. The cross section of the hard scattering is dependent on the strong coupling constant α_s , which in turn depends on the momentum transfer p_T of the hard scattering.

More information about the parton density and the proton structure function can be found in [9, 19, 20].

2.5 General properties of the top quark

The top quark was detected as recently as 1995 by the CDF and the $D\bar{O}$ experiments at the Tevatron collider at Fermilab [21, 22].

As already mentioned, it belongs to the third quark generation of the Standard Model and is a quark with a charge of $+\frac{2}{3}e$, where e is the elementary charge. With a mass of 174.2 GeV [3] the top is the most massive quark and it is the only fermion with a

Yukawa coupling¹³ close to unity [23].

According to the Standard Model top quarks are produced predominantly via the (flavour-preserving) strong interaction but nevertheless, the top quarks decay weakly.

2.5.1 Top quark production

The valence quarks of the protons (uud), colliding at the LHC, do not provide anti-quarks. As a consequence, antiparticles only exist in the *sea* of the protons. As – according to the parton density functions – the fraction of gluons in the proton rises with increasing Q^2 [9] (see also Figure 2.9), it applies that at the very high energies of the LHC¹⁴ the most frequent particles within the proton are the gluons.

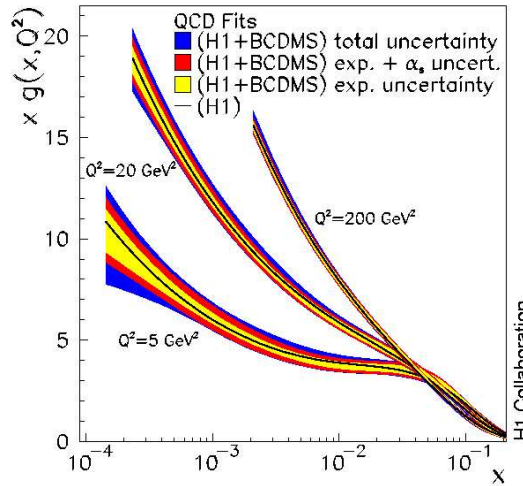


Figure 2.9: Gluon distribution at different Q^2 as a function of the momentum fraction x the gluon carries inside the proton. The fraction of gluons in the proton rises at small x with increasing Q^2 . [24]

Hence, about 87 % of all $t\bar{t}$ events at the LHC will be produced via gluon fusion, as shown in Figure 2.10. At the Tevatron, however, protons (uud) and antiprotons ($\bar{u}\bar{u}\bar{d}$) collide and thus, half of the valence quarks (namely the valence quarks of the antiproton) are antiparticles. Besides, the centre-of-mass energy of the colliding (anti)protons is much smaller¹⁵ than in the case of the LHC. Consequently, gluon fusion produces only 15 % of all $t\bar{t}$ events at the Tevatron.

In addition to gluon fusion top quark events can be produced via $q\bar{q}$ annihilation. This process is illustrated by the Feynman diagram in Figure 2.11. While $q\bar{q}$ annihilation provides only a small fraction of $t\bar{t}$ events at the LHC (≈ 13 %), most of the $t\bar{t}$ events at the Tevatron – almost 85 % – are produced via this reaction.

¹³The Yukawa coupling of the top quark is expressed via $g_t^2 = \frac{2M_t^2}{v^2}$ with $v = 246$ GeV as the expectation value of the Higgs in the vacuum.

¹⁴The centre-of-mass energy at the LHC is expected to be 14 TeV.

¹⁵ $\sqrt{s} = 1.96$ TeV at Run II.

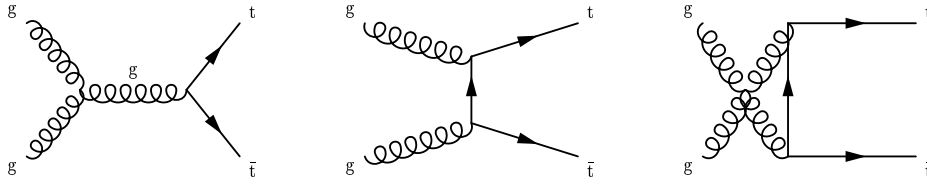


Figure 2.10: Feynman diagrams for the production of $t\bar{t}$ events via gluon fusion.

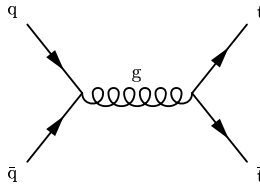


Figure 2.11: Additional Feynman diagram for the production of $t\bar{t}$ events: $q\bar{q}$ annihilation.

Altogether the expected $t\bar{t}$ cross section at the LHC amounts to

$$\sigma(pp \rightarrow t\bar{t}) = 833 \text{ pb} \quad (2.2)$$

in next-to-leading order (NLO) [25]. This comes up to $8 \cdot 10^6$ $t\bar{t}$ events per year at an integrated luminosity of 10 fb^{-1} [26] corresponding to the expected luminosity at the beginning of the LHC and the ATLAS experiment¹⁶.

2.5.2 Top quark decay

The top quark has a very short lifetime:

$$\tau_{top} = O(10^{-24} \text{ s}) \quad (2.3)$$

Therefore, it cannot hadronize as the formation of bound states takes about 10^{-23} s [27]. This fact allows to test the interactions and couplings, as described in the Standard Model, with "pure", thus "unhadronized" samples.

According to the Standard Model the top decays almost exclusively into a W boson and a b -quark, i.e. $t \rightarrow Wb$. Hence, the final state topology of a $t\bar{t}$ event depends on the decay of the W boson. Three different cases have to be distinguished (see also Figure 2.12):

- 1) Fully hadronic decay: $t\bar{t} \rightarrow W^+b W^-\bar{b} \rightarrow q\bar{q}' q\bar{q}' b\bar{b}$

The hadronic decay – exclusively covered in this thesis – is the most frequent $t\bar{t}$ event topology and is outlined in more detail in the following subsection.

Its branching ratio corresponds to 44.4 % of all $t\bar{t}$ events. The fully hadronic or multijet decay shows six (or more) jets in the final state.

¹⁶This integrated luminosity amounts to one year of LHC with $L = 10^{33} \text{ cm}^{-2}\text{s}^{-1}$ [27].

2) Leptonic decay: $t\bar{t} \rightarrow W^+b W^- \bar{b} \rightarrow l^+ \nu l^- \bar{\nu} b\bar{b}$

The two W bosons decay into charged lepton and neutrino, respectively. Consequently, the final state comprises two jets originating from the two b -quarks, two charged leptons and missing energy arising from the two neutrinos which pass the detector without any interaction and which in consequence cannot be identified directly. The branching ratio of the leptonic (or di-lepton) decay arises to 4.9 % [27]¹⁷ which comprises about 400000 dijet events in the first year of LHC [27].

3) Semileptonic decay: $t\bar{t} \rightarrow W^+b W^- \bar{b} \rightarrow l\nu q\bar{q} b\bar{b}$

In the semileptonic decay one W decays into charged lepton and neutrino, the other one into a pair of quark and antiquark. The final state exhibits four jets, one charged lepton and also missing energy. The corresponding branching ratio (which does not include the case of τ +jets) adds up to 29.6 % of all $t\bar{t}$ events. Thus, about 2.5 million semileptonic events per year are expected at the LHC for an integrated luminosity of about 10 fb^{-1} [27].

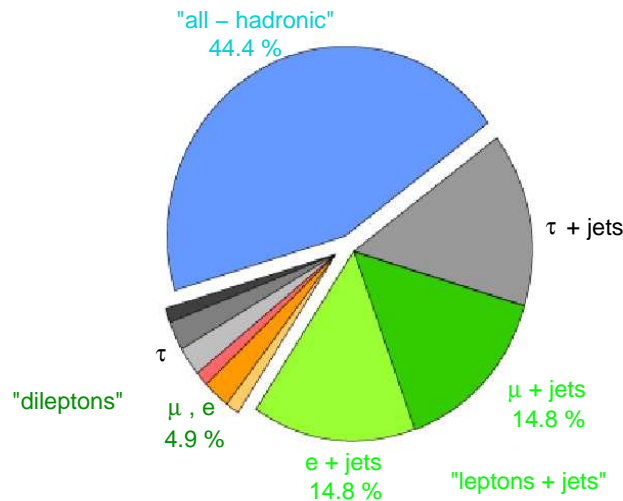


Figure 2.12: Branching fractions of the $t\bar{t}$ decay. 44.4 % of all events decay fully hadronically ("all-hadronic" final state). In 29.6 % the W bosons decay semileptonically (e+jets and μ +jets, respectively), whereas in only 4.9 % the W bosons decay leptonically into electron and neutrino or muon and neutrino. Note, that these branching ratios do neither include the decay into τ +jets nor the leptonic decay into τ leptons.

2.5.3 Particularities of the fully hadronic decay mode

The fully hadronic events, illustrated in Figure 2.13, make up the largest amount of $t\bar{t}$ events. The corresponding branching ratio of more than 44 % indicates a number of

¹⁷This description of the leptonic mode includes only the decay of the W bosons into electron and muon. The decay into tau (τ) leptons is much more complicated due to the different τ decays and is thus not included in the branching ratio introduced.

$3.7 \cdot 10^6$ $t\bar{t}$ multijet events per year at an integrated luminosity of 10 fb^{-1} [27]. The signature of these events shows six or more jets with high transverse jet-momenta $p_{T,jet}$ [28]. Two of these jets originate from the b -quarks. Four jets descend from the quarks coming from the decay of the W bosons. Further jets may appear due to gluon radiation off the quarks, but all in all the fully hadronic final state of a $t\bar{t}$ event is dominated by the hadronization of quarks, not by gluon radiation [28].

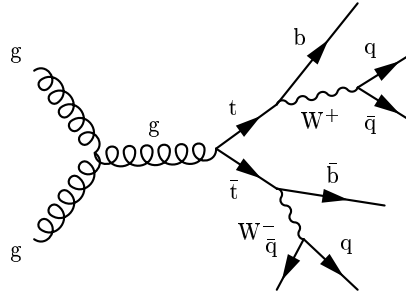


Figure 2.13: Feynman diagram for the fully hadronic $t\bar{t}$ decay.

The $t\bar{t}$ multijet events suffer from a huge background of events which can also have six or more jets, especially the QCD multijet background [27], discussed in Chapter 4. In contrast to the jets in fully hadronic $t\bar{t}$ events the jets in QCD background events originate predominantly from gluon radiation (see Chapter 4).

The separation of the fully hadronic $t\bar{t}$ events from these background events, which have a cross section many orders of magnitude above the $t\bar{t}$ cross section, is the main topic of this thesis.

Chapter 3

LHC and the ATLAS detector

Circular particle colliders like LEP¹, which were operated with electrons and positrons, were strongly limited in the achievable centre-of-mass energy by synchrotron radiation [29]. Therefore, in the last stage of expansion LEP could collide electrons and positrons with centre-of-mass energies of (merely) 209 GeV (LEP2).

The reachable energy can be increased by colliding particles with a much larger rest mass, where the effects of synchrotron radiation become negligible [29].

Consequently, colliders clashing non-elementary particles, like protons and antiprotons², as in the case of the Tevatron at the Fermilab, enormously increase the range of energies within reach. With the construction of the Large Hadron Collider (LHC) at the European particle laboratory CERN³ a new chapter of elementary particle physics has begun, where it will be possible to attain centre-of-mass energies of up to 14 TeV.

3.1 The Large Hadron Collider

The LHC is designed for colliding two counter-rotating beams of protons. Each beam is injected at 450 GeV and is then accelerated up to an energy of 7 TeV. The beams move around the LHC ring inside a continuous vacuum. They are guided by superconducting magnets.

As the protons are no elementary particles the available centre-of-mass energy corresponds to the energies of their constituents, thus quarks and gluons, which carry only a fraction of the protons' energies. A high luminosity ($\approx 10^{34} \text{ cm}^{-2}\text{s}^{-1}$) is aimed in order to increase the number of collisions and consequently to get as many highly energetic collisions between the protons' constituents as possible. This high luminosity can be reached by means of very narrow bunches of particles with bunch-radii of about $15 \mu\text{m}$ at the interaction point, a number of 10^{11} protons per bunch and bunch crossings every 25 ns [29].

The first beam crossings are expected to take place in spring 2008, the first collisions at 14 TeV will probably occur in July 2008 [30].

The LHC will host four main experiments, as it is shown in Figure 3.1: The two

¹Large Electron Positron Collider

²The rest mass of a proton amounts to $m = 938 \frac{\text{MeV}}{c^2}$, which exceeds the rest mass of the electron by a factor of about 2000.

³CERN is the acronym for **C**entre **E**uropéenne pour la **R**écherche **N**ucléaire.

multipurpose experiments ATLAS and CMS, LHCb which measures the properties of particles containing bottom quarks, and ALICE studying collisions of heavy ions and for which LHC will temporarily be run with heavy ions.

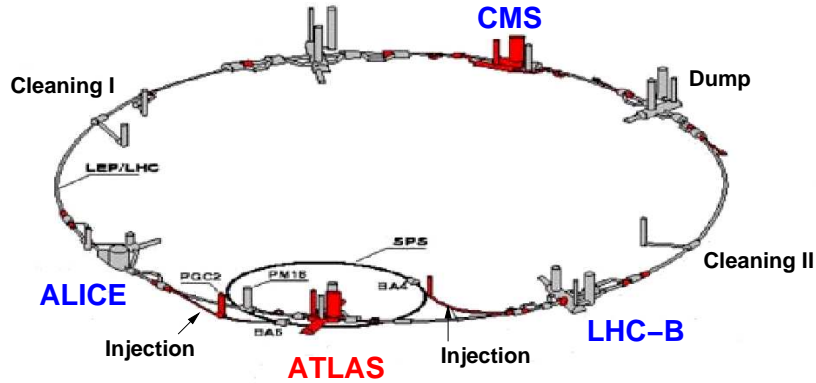


Figure 3.1: Schematic overview of the LHC ring with the four experiments CMS, LHCb, ATLAS and ALICE.

3.2 Design and functionality of the ATLAS detector

The aim of large collider experiments, like the ATLAS⁴ experiment, is to investigate the composition of matter and the fundamental interactions and thus, to test the Standard Model of elementary particle physics. Furthermore, it is intended to discover "new" elementary particles like the Higgs Boson or supersymmetric (SUSY) particles. The ATLAS detector, which is shown in Figure 3.2, is a multipurpose experiment, constructed in several layers, all enclosing the vertex of the two colliding beams.

The inner detector, surrounding the beam pipe and thus, representing the layer closest to the collision point, consists of tightly integrated, radiation tolerant, solid-state detectors [31]. Its function is to track the particles – generated in the beam collisions – including the observation of short-lived particles, such as τ leptons and hadrons containing bottom quarks, by their decay.

The inner detector consists of three subdetectors, covering⁵ $|\eta| \leq 2.5$. The inner sub-detector is made of three layers of silicon pixel detectors. The Silicon Central Tracker (SCT) consists of four double layers of silicon strips [32]. The outer sub-detector – the Transition Radiation Tracker (TRT) – is composed of several layers of straw tubes, interfused with a radiator, stimulating the transition radiation of electrons [32]. The whole inner detector is embedded in a magnetic field of about 2 T allowing the determination of the momentum of charged particles.

⁴A Toroidal LHC ApparatuS

⁵ $|\eta|$ is the pseudorapidity and is defined via $|\eta| = -\ln(\tan\frac{\theta}{2})$.

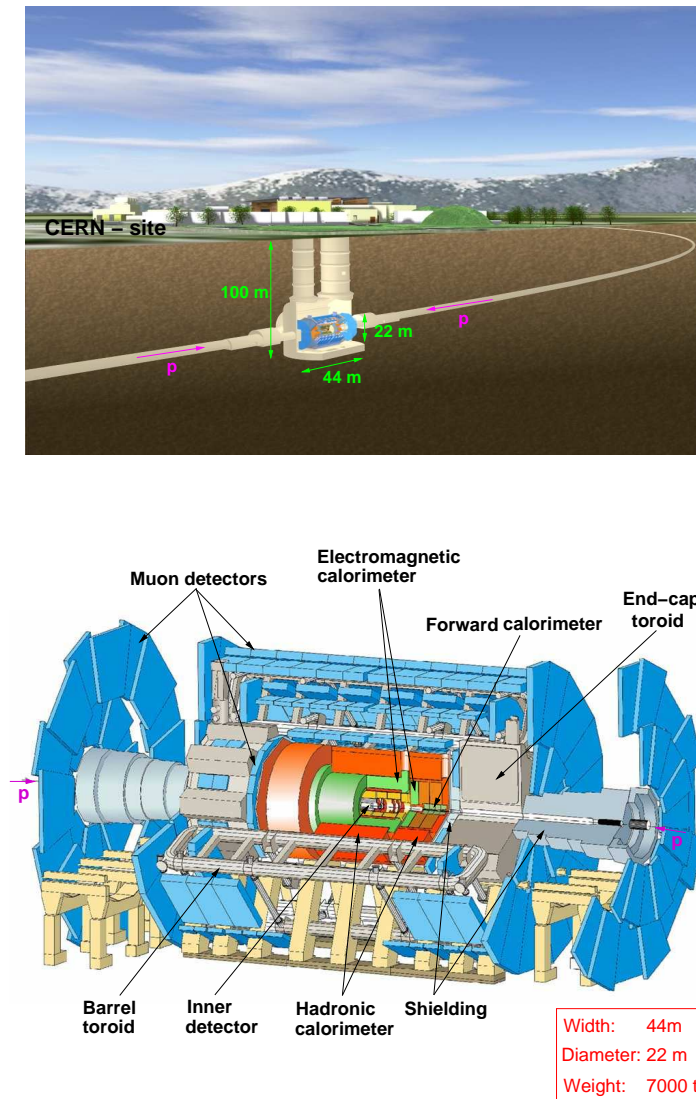


Figure 3.2: Top: Schematic view of parts of the LHC ring and the ATLAS detector in the ground. Bottom: The ATLAS detector which comprises from inside to outside: The inner tracker, the electromagnetic calorimeter, the hadronic calorimeter and the muon system.

The electromagnetic and the hadronic calorimeter measure the energies of the particles. The calorimeter is an important detector component for jet analysis and is thus covered in the next section in more detail.

The muon system constitutes the outer part of the ATLAS detector. It detects muons which are the only particles – except from neutrinos – penetrating the calorimeter. The muon spectrometer consists of three layers of trigger and precision drift tube chambers (see Figure 3.3) in a toroidal magnetic field averaging about 0.6 T. Muons emerging from the vertex cross at least three of the muon chambers, which leads to a precise measurement of these particles, considering in addition the trajectories of the muons deflected due to the magnetic field.

Part of the drift tube chambers⁶ are the BOS-MDTs. These chambers have been calibrated at the cosmic ray measurement facility of the LMU, where – among other tests – a pulser test has been carried out in order to check the functionality of the chambers’ read-out electronics. For the pulser test an electric pulse, which simulates the real signal the hardware will face once the LHC has started, was sent to the muon chambers and the output of the chambers was monitored and analyzed. This way the functionality and effectiveness of the electronics were tested and thus, it was ensured that the underlying hardware will operate properly when the first real ($t\bar{t}$) signals will arise. A detailed description of the pulser test can be found in Appendix C of this thesis.

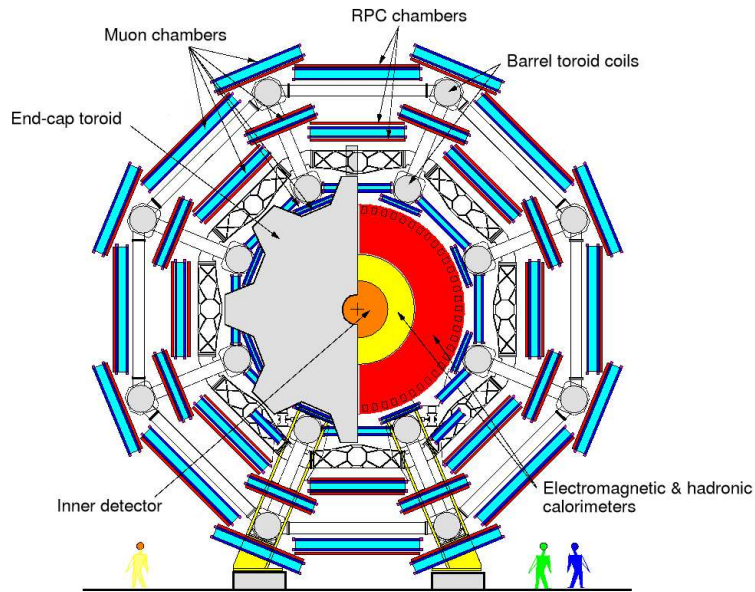


Figure 3.3: The ATLAS detector with the muon spectrometer representing three layers of trigger and drift tube chambers [31]. The furthestmost muon chambers are the ATLAS BOS - Monitored Drift Tube (MDT) chambers.

3.3 The electromagnetic and the hadronic calorimeter

The design of the calorimeter is always based on the requirements for energy and spatial resolution. In contrast to other detectors its intrinsic resolution improves with rising energy, making it a particularly suitable detector at high energy colliders like the LHC.

Due to the different interaction behaviour of electrons or photons on the one hand and hadrons on the other hand, the calorimeter is usually divided into an electromagnetic and a hadronic calorimeter section.

The calorimeter is crucial for understanding the diverse physics processes with jets,

⁶There are different sizes of muon chambers, among them BOS (**B**arrel **O**uter **S**mall), BIS (**B**arrel **I**nner **S**mall), BIL (**B**arrel **I**nner **L**arge), BMS (**B**arrel **M**iddle **S**mall), BML (**B**arrel **M**iddle **L**arge) and BOL (**B**arrel **O**uter **L**arge) chambers and more in the end-cap and between the ATLAS feet.

missing transverse energy, photons or charged particles like electrons. The particles and jets can be reconstructed via the energy they deposit in the calorimeter.

The ATLAS electromagnetic calorimeter, which is presented in Figure 3.4, is a lead and Liquid-Argon (LAr) sampling calorimeter consisting of a barrel and two end-cap parts [33]. The lead serves as showering (and absorbing) material whereas the Argon is the active part of the calorimeter.

The barrel part with $|\eta| \leq 1.475$ has the shape of an accordion for the lead absorbers and the electrodes (EM accordion calorimeter, Figure 3.4). In this way, it covers the whole range in ϕ without any gaps.

The end-cap calorimeter (EM LAr end-cap calorimeter, $1.4 \leq |\eta| \leq 3.2$) has a similar structure to that of the barrel calorimeter, but comprising lead absorbers like the spokes of a wheel [33].

Both the end-cap part and the barrel part are supplemented by sampling detectors, reaching $|\eta| = 1.8$, evaluating the energy loss due to the early starting showers in front of the calorimeter [33].

The calorimeter has a granularity of $\Delta\eta \times \Delta\phi = 0.025 \times 0.025$, with the pseudorapidity $\eta = -\ln(\tan \frac{\theta}{2})$ and azimuthal angle ϕ . The energy resolution for electromagnetic showers is about $\Delta E/E = 10\% / \sqrt{\frac{E}{\text{GeV}}}$.

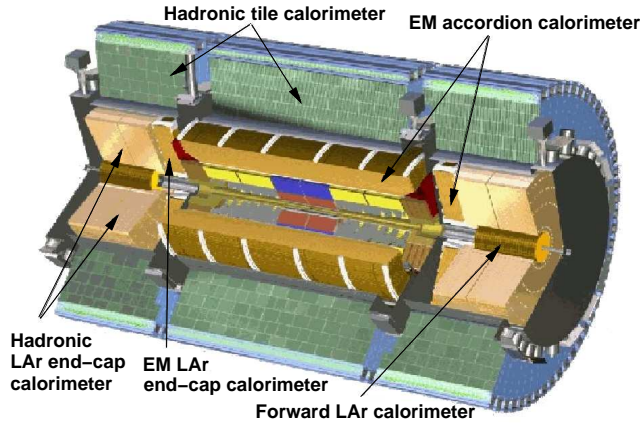


Figure 3.4: ATLAS electromagnetic (EM) and hadronic calorimeter.

The hadronic calorimeter, also illustrated in Figure 3.4, measures in general the energy of hadronic particles, such as pions. Such particles are likely to pass through the electromagnetic calorimeter⁷ but do interact via the strong force in the absorber material of the hadronic calorimeter. Like the electromagnetic calorimeter it is divided into a barrel and an end-cap part, ensuring a measurement of hadronic showers in almost full solid angle (i.e. 4π which corresponds to $|\eta| < 3.2$).

⁷In fact, hadronic particles start showering already in the electromagnetic calorimeter. The hadronic showers are much vaster than the electromagnetic showers. Thus, while the electromagnetic showers start and end in the electromagnetic calorimeter, the hadronic showers start in the electromagnetic calorimeter and expand to the hadronic calorimeter.

The barrel region with $|\eta| < 1.7$ contains iron tiles and scintillator tiles (see Hadronic tile calorimeter in Figure 3.4), stacked in planes pointing to the beam pipe. The light produced by the scintillators is read out with wavelength shifting fibres to photomultipliers on the outside of the calorimeter [4].

The hadronic end-cap calorimeter (Hadronic LAr end-cap calorimeter, Figure 3.4) is a parallel-plate liquid Argon sampling calorimeter [34] with copper plate absorbers, measuring up to a value of $\eta = 3.2$ [32].

Up to $|\eta| = 2.5$ the granularity of the hadronic calorimeter comes to about $\Delta\eta \times \Delta\Phi = 0.1 \times 0.1$, allowing a precise measurement of the energy and the angles of jets and single charged particles [32]. For $|\eta| > 2.5$ the granularity amounts to $\Delta\eta \times \Delta\Phi = 0.2 \times 0.2$. The energy resolution of the hadronic calorimeter is expected to be $\Delta E/E = (50\% - 100\%)/\sqrt{\frac{E}{\text{GeV}}}$ [29].

Chapter 4

Characterization of the background to fully hadronic $t\bar{t}$ events

The LHC is a top quark factory. Many millions of top quarks will be produced in a year. Most of these top quarks show up as fully hadronic $t\bar{t}$ events, as already outlined in Chapter 2. Thus, about $3.7 \cdot 10^6$ fully hadronic $t\bar{t}$ events are expected in the first nominal year of the LHC at a still very low luminosity of 10 fb^{-1} .

These fully hadronic $t\bar{t}$ events are completely swamped by lots of background events. The analysis and the understanding of the top quarks' properties, however, becomes very difficult or almost impossible when they are overlaid by background events.

This chapter characterizes different kinds of background events to the fully hadronic $t\bar{t}$ events and outlines their possible impact on the study of fully hadronic $t\bar{t}$ events.

4.1 The QCD multijet background

The most important background of fully hadronic $t\bar{t}$ events is the QCD multijet background emerging from processes [35], like

$$gg \rightarrow gg$$

$$gg \rightarrow q\bar{q}$$

$$qg \rightarrow qg$$

$$qq \rightarrow qq$$

$$q\bar{q} \rightarrow qq$$

$$q\bar{q} \rightarrow gg$$

Unfortunately, the QCD is one of the parts of the Standard Model which has been investigated least of all so far [36], which makes it even more difficult to predict the detailed properties of the corresponding background events and their influence on the analysis of the $t\bar{t}$ events.

Figure 4.1 presents Feynman diagrams illustrating two possible QCD multijet background processes with six final jets. Instead of a pair of top quarks the QCD multijet background events comprise a pair of lighter quarks or gluons in the final state. These particles emit gluons which finally hadronize. Thus, most of the jets in the background events originate from gluon radiation whereas the jets in the $t\bar{t}$ events are predominantly caused by the hadronization of quarks (see Figure 2.13).

The presumed cross section for all kinds of QCD multijet events amounts to

$$\sigma_{QCD} = 1.4 \mu\text{b} ,$$

as predicted by the ATLAS collaboration [37]. This cross section¹ includes all possible QCD processes with up to six partons in the final state. Those with two, three and four jets can more or less easily be distinguished from the topology of a fully hadronic $t\bar{t}$ event by setting a lower limit on the number of reconstructed jets.

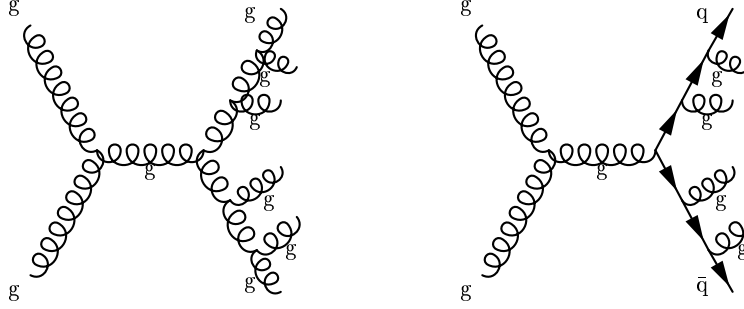


Figure 4.1: Illustration of possible QCD multijet background events with six jets in the final state.

The real problem is given by the 5-jet and 6-jet background events, based on the large number of jets in the final state, which causes these events to have a final state topology almost identical to that of the $t\bar{t}$ events. This topology makes it very difficult to distinguish these QCD background events from the $t\bar{t}$ signal. The cross section for the 5-jet and 6-jet QCD events, generated for this analysis, adds up to about [13]

$$\sigma_{QCD_{5,6}} \approx 0.1 \mu\text{b}$$

(see Section 7.2.2), which is still a very large value in comparison to the cross section of the fully hadronic $t\bar{t}$ events at the LHC which amounts to [37, 38]:

$$\sigma = 0.37 \cdot 10^{-3} \mu\text{b}$$

This fully hadronic $t\bar{t}$ cross section was derived from the expected production cross section for top quark pairs of 833 pb, as indicated in [37, 38], by multiplying this total cross section with the branching fraction of 44 % for fully hadronic $t\bar{t}$ decays.

Therefore, the 5-jet and 6-jet QCD events prevail the $t\bar{t}$ events by a factor of about 1000. Because of this fact and due to the very similar final state topology, it is a big

¹The cross section is estimated for events with a transverse momentum transfer $p_T > 100$ GeV for the hard process [37].

challenge to separate the $t\bar{t}$ signal from the QCD background.

The separation of the fully hadronic $t\bar{t}$ signal from the QCD multijet background events poses the main part of the underlying thesis and is described in Chapter 8.

4.2 W and Z pair production

There is another possible background for the $t\bar{t}$ events which features W and Z bosons, as indicated by the following equations:

$$q\bar{q} \rightarrow W^+W^-$$

$$q\bar{q} \rightarrow W^{+/-}Z$$

$$q\bar{q} \rightarrow ZZ$$

$$[gg \rightarrow W^+W^-]$$

$$[gg \rightarrow ZZ]$$

These processes represent the different ways of W/Z pair production at the LHC. The last two equations are in brackets as their production cross section, given by PYTHIA [13], is tiny and thus, they can be neglected.

Events with W/Z bosons and additional jets, as sketched in Figure 4.2, can comprise a large number of final state jets as it is the case for the fully hadronic $t\bar{t}$ events.

In most cases the W and Z bosons decay hadronically [3]², which is also illustrated in Figure 4.2. The resulting final states comprise (only) jets, making them very similar to the $t\bar{t}$ and also to the QCD background events. The occurring jets originate from the hadronization of quarks (which emerge from the decay of the W/Z bosons) as well as from the radiation of gluons.

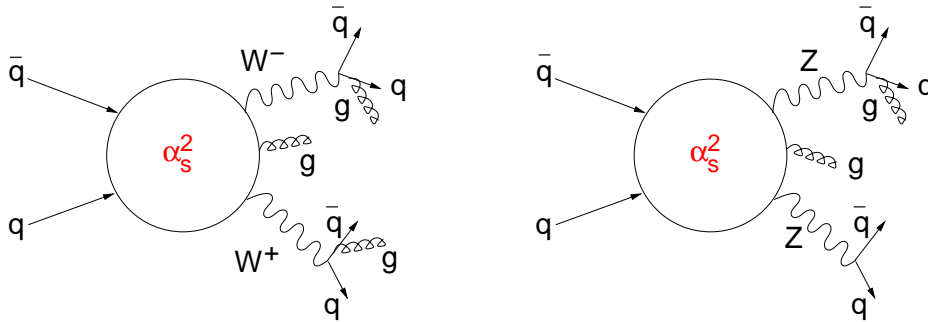


Figure 4.2: W/Z production with additional jets. The cross section of the $W/Z + n$ jets events is proportional to α_s^2 in lowest order. The W bosons decay in most cases into pairs of quarks. Another decay mode leads to charged leptons and the corresponding (anti)neutrinos in the final state, as outlined in Section 2.5.2. However, this decay mode is neglected when regarding possible $t\bar{t}$ background events. The Z boson decays mostly into a pair of quark and antiquark, too, but it can also decay into lepton and antilepton (which is irrelevant for the case of the fully hadronic $t\bar{t}$ background events).

²See also Section 2.5.2.

Nevertheless, the W/Z events can also feature different final states. The W^+W^- events can have charged leptons and missing transverse energy: $W^+W^- \rightarrow l^+\nu l^-\bar{\nu}$. The events including the production of Z bosons show up to four charged leptons ($ZZ \rightarrow l^+l^-l^+l^-$). Events comprising both – W and Z bosons – exhibit a mixture of these two final states. All possible final states are presented in Table 4.1.

Process	# Jets	# Leptons	Missing Energy
Fully hadronic $t\bar{t}$ decay	≥ 6	-	no
$W^+W^- \rightarrow q\bar{q}q\bar{q}$	≥ 4	-	no
$W^+W^- \rightarrow q\bar{q}l\nu$	≥ 2	1	yes
$W^+W^- \rightarrow l^+\nu l^-\bar{\nu}$	≥ 0	2	yes
$W^{+/-}Z \rightarrow q\bar{q}q\bar{q}$	≥ 4	-	no
$W^{+/-}Z \rightarrow q\bar{q}ll$	≥ 2	2	no
$W^{+/-}Z \rightarrow l\nu q\bar{q}$	≥ 2	1	yes
$W^{+/-}Z \rightarrow l\nu ll$	≥ 0	3	yes
$ZZ \rightarrow q\bar{q}q\bar{q}$	≥ 4	-	no
$ZZ \rightarrow q\bar{q}ll$	≥ 2	2	no
$ZZ \rightarrow ll ll$	≥ 0	4	no

Table 4.1: Different final states in W/Z pair production processes. The fully hadronic W/Z decays are tagged in red as they are the only processes comprising final states which are quite similar to the topology of a fully hadronic $t\bar{t}$ event. The table lists for comparison also the features of fully hadronic $t\bar{t}$ events, marked in blue.

Obviously, the events, in which the W/Z bosons do not decay completely hadronically, have very different final state topologies in comparison to the $t\bar{t}$ events and thus, they can be distinguished quite easily from the fully hadronic $t\bar{t}$ signals. Even the exclusion of a single lepton (electron or muon) in the regarded events would skip the whole amount of the referred W/Z background events, while no fully hadronic $t\bar{t}$ event would be lost. Therefore, the non-hadronic W/Z events can be neglected completely when regarding possible background events for $t\bar{t}$ signals.

In addition, the W/Z pair production processes, as listed above, have a much smaller production cross section than the $t\bar{t}$ events. While the $t\bar{t}$ events, produced for this thesis, have a cross section³ of 0.16 nb (see Section 7.2.2), a test sample of W/Z events – which were forced to decay fully hadronically – prevailed cross sections of 0.0075 nb ($q\bar{q} \rightarrow W^{+/-}Z \rightarrow$ jets) up to 0.03 nb ($q\bar{q} \rightarrow W^+W^- \rightarrow$ jets). These cross sections show that even the contributions of the fully hadronic W/Z events are almost negligibly small.

Because of these reasons, the referred W/Z events have not been included in the back-

³The cross section of the fully hadronic $t\bar{t}$ events produced for this thesis is smaller than the cross section of 0.37 nb expected at the LHC. This is due to settings in PYTHIA and the calculation of the corresponding cross section in LO, as described in the Sections 6.2.1 and 7.2.2 and in Appendix A.

ground studies. They account only for a very small fraction of the background to fully hadronic $t\bar{t}$ events [35].

4.3 τ lepton decays

Among the three generations of leptons in the Standard Model the τ lepton is the heaviest one⁴. As a consequence, the τ lepton can decay in both ways, leptonically and hadronically (with accompanying hadrons). It is thus the only lepton that can decay into hadrons.

While the leptonic decay is a three body decay resulting in a light lepton, the corresponding antineutrino and a τ neutrino ($\tau \rightarrow l\bar{\nu}_l\nu_\tau$), the hadronic decay is a two body decay producing a hadron (which decays further) and a τ neutrino. The whole amount of different τ lepton decays can be read in [3].

The branching fractions for the leptonic decay of the τ lepton can be calculated easily, including contributions of initial and final state radiation. Most hadronic decays are obtained from experimental data [39]. Some hadronic decays, however, cannot be calculated explicitly and thus, the total decay width of the τ leptons is (only) known from the lifetime of the τ lepton. The branching fractions for the most important hadronic decays are listed in Table 4.2.

Decay mode	Branching fraction
$\pi^- \nu_\tau$	11%
$\pi^- \pi^0 \nu_\tau$	25%
$\pi^- \pi^+ \pi^- \nu_\tau$	9%
$\pi^- \pi^0 \pi^0 \nu_\tau$	9%
$\pi^- \pi^+ \pi^- \pi^0 \nu_\tau$	4%
$\pi^- \pi^0 \pi^0 \pi^0 \nu_\tau$	1%

Table 4.2: Branching fractions for the most abundant hadronic decays of the τ lepton [3].

In the leptonic case there are no final state jets making these events completely negligible as possible $t\bar{t}$ background. In the hadronic decay mode, however, up to five (or more) hadrons can appear⁵. In any case, events comprising τ leptons feature always missing energy due to the occurring neutrinos.

All in all τ lepton events comprise a large variety of decay modes and corresponding final states. Nevertheless, it should not be too difficult to distinguish them from the final states of fully hadronic $t\bar{t}$ events. A simple limitation of missing energy in the regarded events might be enough to remove the τ events, while losing only a very small fraction of $t\bar{t}$ events.

⁴The τ lepton has a mass of about 1.8 GeV [3].

⁵ τ lepton decays with up to five hadrons have been observed [3]. Nevertheless, the hadronic τ events can still comprise a larger number of jets due to final state radiation.

In addition, the τ leptons are predominantly produced by the decay of W/Z bosons and photons or the decay of massive quarks, like the top quark and the bottom quark. The production cross section of those events is always small compared to the fully hadronic $t\bar{t}$ events (see also previous section).

Because of these reasons the τ lepton decays were neglected in the background studies for fully hadronic $t\bar{t}$ events.

Chapter 5

The k_T algorithm

This thesis focuses on the study of $t\bar{t}$ multijet and QCD multijet background events, featuring jets as the main and most important signature for the separation of signal from background events. Therefore, the examination and understanding of jet physics play a crucial role for this analysis.

This chapter aims to describe the formation of jets as well as to outline the different criteria for allocating particles to jets in the case of a jet reconstruction with the k_T algorithm [40]. Furthermore, the k_T algorithm is compared with the Cone algorithm [41, 42], which is used in many analyses for jet reconstruction at hadron colliders.

5.1 Production of jets

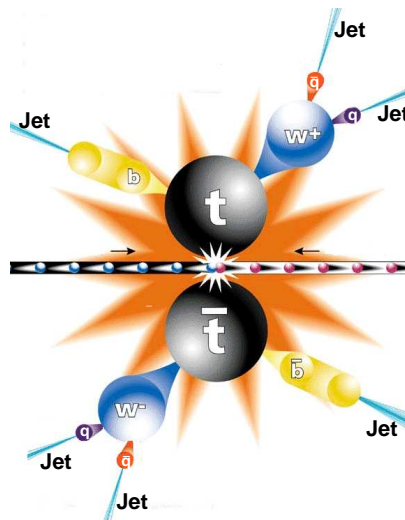


Figure 5.1: Schematic drawing of a $t\bar{t}$ multijet event with six jets.

As it was already outlined in Chapter 2 and 3, protons are no elementary particles but are composed of quarks and gluons. Highly energetic collisions of protons, like at the LHC, lead to an interaction of the protons' constituents. In ideal case there is a single hard, thus highly energetic, collision of two partons. In this way two scattered partons

show-up at large angle with respect to the proton beams. This pair of partons starts – just after its formation – radiating gluons and quarks, which emit further gluons splitting into pairs of quarks and antiquarks. Thus, a parton shower is induced forming a bunch of highly energetic partons (quarks and gluons), the parton jets. Due to the confinement (Chapter 2) the partons build colour-neutral particles forming the particle jets, which are outlined in Figure 5.1. However, this hadronization has no impact on the structure of the jets, which means that hadronization does not change the allocation of particles to the jets¹.

Sketch 5.2 illustrates the different phases a jet passes through. In the beginning the jets consist of partons, after the hadronization they are formed by stable and long-lived particles, like pions. In the last phase the jets are made up of objects measured in the calorimeter. This analysis deals with the particle and calorimeter jets (see also Chapter 6.4).

In order to allocate the particles and energy depositions in the calorimeter to different jets a jet algorithm is used. In the case of this thesis it is the k_T algorithm.

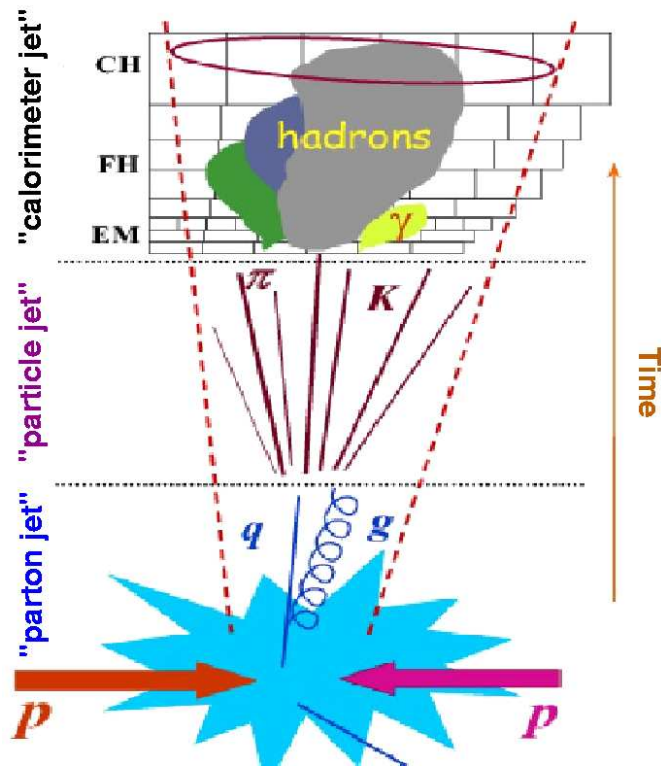


Figure 5.2: pp scattering in different phases. The initial pair of partons forms jets. The image shows the phase just before the hadronization (parton jets), after the hadronization (particle jets) and the calorimeter jets reconstructed from the particles' energy deposition in the calorimeter. [41]

¹This statement is valid as long as no long range correlations become important.

5.2 Jet reconstruction with the k_T algorithm

Before the k_T algorithm can start to cluster particles or energy depositions to jets, there are some technical aspects of the reconstruction which have to be taken into account. These requirements are outlined in the following.

5.2.1 Jet resolution variables

For defining the resolution of jets one has to decide on a kind of "measure of distance", including the distance between two particles and the distance of a particle to the beam, which can be expressed via so-called angular definitions [40]. There are three different resolution variables implemented, described in [40]:

- The angular scheme (*angle* = 1) with the following resolution variables:
Distance of a particle to the beam:

$$d_{iB} = 2E_i^2(1 - \cos(\theta_{iB})) \quad (5.1)$$

Distance between two particles:

$$d_{ij} = 2 \min(E_i^2, E_j^2)(1 - \cos(\theta_{ij})) , \quad (5.2)$$

where the index B stands for beam.

- The ΔR scheme (*angle* = 2):
Distance of a particle to the beam:

$$d_{iB} = p_{T,i}^2 \quad (5.3)$$

Distance between two particles:

$$d_{ij} = 2 \min(p_{T,i}^2, p_{T,j}^2) R_{ij}^2 \quad \text{with} \quad (5.4)$$

$$R_{ij}^2 = (\eta_i - \eta_j)^2 + (\Phi_i - \Phi_j)^2 , \quad (5.5)$$

where $p_{T,i}$ is the transverse momentum of the i -th particle to the beam axis. This definition of R_{ij}^2 is the standard setting for the reconstruction of Cone jets (see Section 5.3) and thus, the most common choice for hadron-hadron collisions [40]. Consequently, the ΔR scheme is used as standard resolution scheme for jet reconstruction in this thesis.

- The QCD emission scheme (*angle* = 3):
This scheme corresponds to *angle* = 2 with an alternate definition of R_{ij}^2 due to the form of QCD matrix elements for multi parton processes [40].

$$R_{ij}^2 = 2[\cosh(\eta_i - \eta_j) - \cos(\Phi_i - \Phi_j)] \quad (5.6)$$

5.2.2 The recombination scheme

With the recombination scheme one can define how to merge two objects i and j to a single one with 4-momentum p_{ij} [40]. There are five possible choices, two of which have been used in this analysis:

- The E scheme ($recom = 1$):

$$p_{ij} = p_i + p_j \quad (5.7)$$

The 4-momentum is calculated by simple 4-vector addition resulting in massive jets. This might pose a problem for the jet reconstruction in QCD events due to the massless QCD matrix element. Consequently, as QCD multijet events play a very important role in this analysis, the E scheme cannot be the first choice as jet recombination scheme in this thesis. Thus, it was only adopted for fully simulated $t\bar{t}$ events (see Chapter 6) which have predefined generation and reconstruction settings one cannot easily change, retrospectively.

- The E_T scheme ($recom = 4$):

$$E_{T,ij} = E_{T,i} + E_{T,j} \quad (5.8)$$

$$\eta_{ij} = \frac{E_{T,i}\eta_i + E_{T,j}\eta_j}{E_{T,ij}} \quad (5.9)$$

$$\Phi_{ij} = \frac{E_{T,i}\Phi_i + E_{T,j}\Phi_j}{E_{T,ij}} \quad (5.10)$$

This scheme deals with massless and massive input objects [40], but provides only massless combined output objects (jets). It is therefore the best choice for the reconstruction of QCD multijet and also $t\bar{t}$ multijet events and was used as standard setting for all events specially produced for this thesis.

The other recombination schemes (p_T scheme ($recom = 2$), p_T^2 scheme ($recom = 3$) and E_T^2 scheme ($recom = 5$)) are detailed in [40].

5.2.3 The reconstruction mode

The algorithm employed [40] can be used for the reconstruction of jets in high energy particle collisions as well as in e^+e^- reactions. There are two different reconstruction modes for running the algorithm, the **inclusive** and the **exclusive** mode. The difference in these two modes lies in the definition of the hard final state jets and in the separation of the jets from the proton beam remnants [40].

- **The inclusive mode:** The distance of a particle to the beam and between two particles is fixed by the jet resolution variables, as described in Section 5.2.1. The dimensionless parameter R , which is usually set to 1.0, defines the extent of the jets [40]. It acts like a radius for the jets.
The distance of a final state object d_i to the beam is scaled with the parameter R :

$$d_i = d_{iB}R^2 \quad (5.11)$$

The particles i and j are combined to a jet – according to the selected recombination scheme (Section 5.2.2) – if d_{ij} is the minimum out of $\{d_i, d_{ij}\}$.

The algorithm stops automatically when all objects have been included in jets. There is no cut-off or stopping condition. The size and thus, the number of jets can only be regulated via parameter R . As a consequence, parts of the proton remnants may be included accidentally in the reconstruction of the jets as the final state jets are not clearly cut off from the beam remnants. This results in a larger number of jets in inclusive mode. For this reason the inclusive mode is not chosen for the jet reconstruction in this thesis.

- **The exclusive mode:** The hard final state is explicitly separated from the soft beam remnants. Jets are defined in the hard final state by the stopping parameter d_{Cut} . d_{Cut} is a measure of distance in the momentum space and corresponds to the maximum distance between two particles. It has the dimension of energy squared and defines the hard scale of the process. The following applies for the stopping parameter d_{Cut} :

$$\Lambda_{QCD}^2 \ll d_{\text{Cut}} \leq s \quad (5.12)$$

Λ_{QCD} is the only free parameter of the Quantum Chromo Dynamics with a value of a few hundred MeV and s denotes the squared centre-of-mass energy in the hard scattering.

Two cases for the stopping parameter d_{Cut} have to be distinguished:

- $d_{\text{Cut}} \rightarrow \Lambda_{QCD}^2$: For small values of the cut-off parameter the condition² $\min\{d_{ii}, d_{ij}\} < d_{\text{Cut}}$ is not satisfied any more and the algorithm will stop before several particles could have been combined to a jet. This leads to events with (too) many jets in the final state.
- $d_{\text{Cut}} \rightarrow s$: In this case events with a very small number of jets are produced. The size of the jets rises with an increasing d_{Cut} , thus for the limiting case $d_{\text{Cut}} \rightarrow \infty$ all particles will be joined into one single jet.

5.2.4 The reconstruction in exclusive mode

For the actual reconstruction in the exclusive mode the jet algorithm starts with a list of energy-preclusters [43], built from partons, particles or calorimeter cells. The distance between the preclusters is defined via

$$\Delta R = \sqrt{\Delta\eta^2 + \Delta\phi^2}, \quad (5.13)$$

with η being the pseudorapidity and ϕ the azimuthal angle. The actual reconstruction, which is also outlined in the block diagram 5.3, proceeds in the following way:

- 1) The algorithm calculates for each object i the square of its transverse momentum with respect to the beam axis $d_{ii} = p_{T,i}^2$. For each pair ij of objects a distance function $d_{ij} = \min(p_{T,i}^2, p_{T,j}^2) \Delta R_{ij}^2 / D^2$ is determined with the dimensionless scaling parameter D which defines the size of the jets and which is set to unity in this analysis.

²With $d_{ii} = p_{T,i}^2$.

- 2) The minimum d_{min} of all d_{ii} and d_{ij} is calculated. If the minimum equals the distance function d_{ij} , the objects i and j are recombined to a new object k , putting it back in the list of objects while removing objects i and j from this list. The algorithm starts from the beginning.
- If the minimum is d_{ii} , object i is classified as a jet and is removed from the list. When the minimum of d_{ii} and d_{ij} is larger than d_{Cut} ($d_{min} > d_{Cut}$) the algorithm stops and all remaining objects in the list are classified as jets.
- 3) The algorithm operates as long as there are any objects left or d_{min} is smaller than the cut-off parameter d_{Cut} .

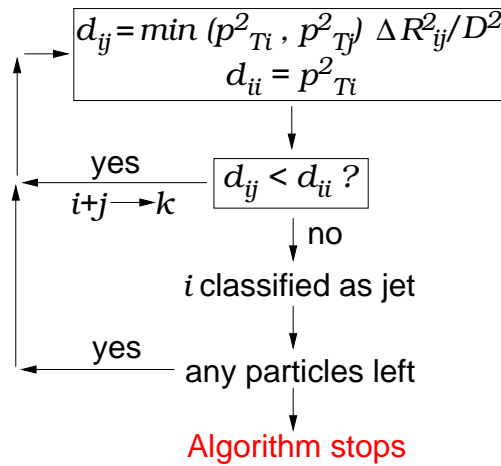


Figure 5.3: Block diagram: Jet reconstruction steps of the exclusive mode of the k_T algorithm.

In summary, one can say that the algorithm clusters pairs of nearby objects, where the closeness is defined by similarity in transverse momentum with respect to the jet axis ($p_T(1 - \cos \theta)$) and direction of the objects. An object is allocated to a jet, if it is clearly separated from other ones. In this context the cut-off parameter d_{Cut} characterizes approximately the size of the resulting jets. Further details concerning the jet reconstruction can be found in [40] and [2].

5.3 Comparison between k_T and Cone algorithm

The algorithm most often used for jet reconstruction at hadron colliders is the Cone algorithm. Thus, there is not yet very much experience in jet reconstruction from hadron collisions with the k_T algorithm. For event generation with ATLAS software (see Chapter 6.3) the k_T algorithm is available but the Cone algorithm is usually employed for the jet reconstruction at large collider experiments.

The Cone algorithm allocates objects to a jet which are located within a cone with a certain radius $R = \sqrt{\Delta\eta^2 + \Delta\phi^2}$. Particles which are outside the cone are not associated to the jet (Figure 5.4).

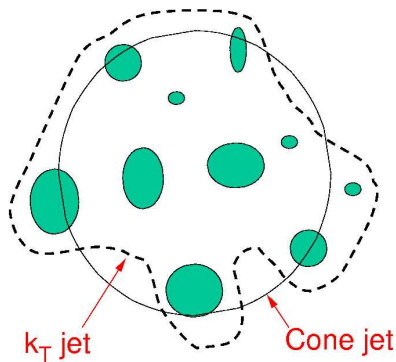


Figure 5.4: Comparison between k_T and Cone Algorithm. The k_T algorithm clusters objects with a similar p_T and adjusts dynamically to the jets. [41]

Thus, the whole detector has to be covered with these virtual cones resulting in the production of overlapping jets, as shown in Figure 5.5.

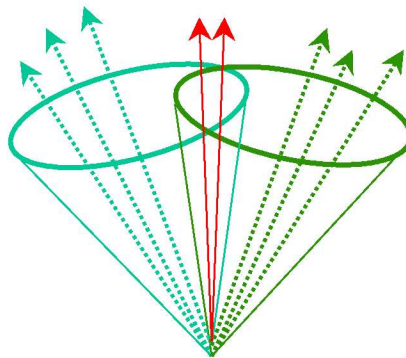


Figure 5.5: Overlapping cones in the jet reconstruction with the Cone algorithm. [41]

This makes an arbitrary splitting and merging of cones necessary in order to separate overlapping jets or combining them³, which also leads to the fact that the Cone algorithm is not infrared and collinear safe (Figure 5.6 and 5.7). In this context *infrared* means that the momentum of the radiated gluon is very small and *collinear* denotes that the angle between the radiating and the radiated gluon is very small. These are regions in the phase space which are not covered by the Cone algorithm. In addition, theoretical predictions for the Cone algorithm, which have been calculated in next-to-leading-order (NLO), are not infrared safe [43] and are consequently sensitive to low energetic radiation.

³These problems could partly be solved by the newly introduced Midpoint Cone algorithm [44].

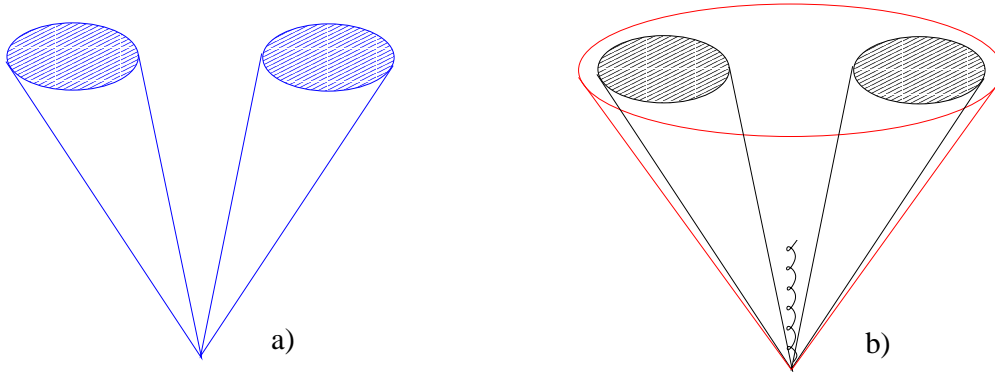


Figure 5.6: Illustration of an arbitrary merging of cones by the Cone algorithm. a) Two jets in the final state. b) The jet multiplicity changes ($2 \rightarrow 1$) after the emission of a soft gluon leading to infrared divergences in the phase space.

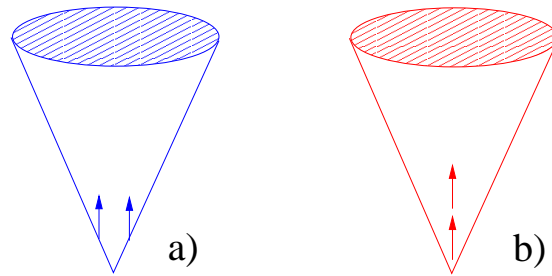


Figure 5.7: Collinear divergences at the jet reconstruction with the Cone algorithm. a) The partons are below the threshold, no jet is reconstructed. b) The jet multiplicity changes ($0 \rightarrow 1$) due to replacement of a massless parton by the sum of two collinear particles [45].

The k_T algorithm, however, avoids these problems. It is collinear and infrared safe in each order of perturbation theory [43] and it is less dependent on hadronic corrections. Additionally – as it clusters objects with a similar transverse momentum – it does not produce overlapping jets.

The reconstruction procedure of the k_T algorithm is very dynamic. The parton shower is reconstructed reversely to its starting point whereas the transverse momentum (k_T) of the partons and gluons serves as classification criterion or time coordinate, alternatively. The algorithm adjusts itself to the jets. Each object is unequivocally allocated to one jet which makes a further separation or combination redundant [43]. The k_T algorithm also includes objects into a jet which are wrongly excluded by the Cone algorithm, which is emphasized in Figure 5.4. As the distance between the objects is characterized by their transverse momenta the size of the resulting jets is dynamic. Last but not least the k_T algorithm is invariant under boosts along the beam direction⁴

⁴For the sake of completeness it should be mentioned that the Cone Algorithm is also invariant under boosts along the beam direction.

which is a crucial property at high energy collisions and leads to improved factorization properties and closer correspondence to experimental practice at hadron colliders [46]. Taking these properties of the two algorithms into account the k_T algorithm seems to be the most reasonable and promising choice for an efficient reconstruction of jets in hadron-hadron collisions.

Chapter 6

Monte Carlo generators

The analysis of real data, taken in a huge collider experiment, represents the major task when studying particle physics processes. A simulation of the particle reactions is needed to interpret the results of analyses and to compare the simulation with the real data, adjusting analysis techniques.

In the case of the LHC – where there is no real data yet – the simulation of particle processes plays a particularly crucial role, delivering the first information about the physics processes at the LHC and preparing the study of the data which will be available presumably in the middle of 2008.

The Monte Carlo (MC) simulation is a stochastic technique, which means it is based on the use of random numbers and probability statistics in order to investigate (among other problems) particle physics processes. For the simulation of the physics processes very different MC generators with fairly diverse fields of simulation are available. Some of these generators are outlined on the following pages.

6.1 ALPGEN

For processes with a large jet multiplicity, as it is the case for $t\bar{t}$ multijet events and QCD multijet events, the complexity of matrix element evaluation and of its singularity structure poses a challenge [47] for an exact simulation.

New strategies have been examined [48] which include a reweighting of the matrix element weights and a kind of "veto" of shower development in regions of the phase space which have already been sampled by a different parton-level configuration [47]. This procedure makes it possible to merge the multijet matrix elements with the shower evolution. These recent developments have been included in the Monte Carlo generator ALPGEN version 2.03 [47], which was utilized for the generation of the background events.

6.1.1 Choice of the subprocess

ALPGEN provides the generation of processes with N jets in the final state with up to two light quark pairs [47]. This operation was used for simulating the 4-vectors of the QCD multijet background events needed for this thesis. The shower evolution and jet reconstruction for these events was carried out as an independent step in PYTHIA [13]

(Section 6.2) succeeding the generation of unweighted parton-level events [47].

The available hard $2 \rightarrow 2$ processes for the N Jets code, to which up to four partons are added, are listed in Table 6.1. The other processes available in ALPGEN are described in [47].

process	$gg \rightarrow gg$	$q\bar{q} \rightarrow gg$	$gq \rightarrow qg$	$qg \rightarrow qg$	$gg \rightarrow q\bar{q}$
process	$qq \rightarrow qq$	$qq' \rightarrow qq'$	$q\bar{q}' \rightarrow q\bar{q}'$	$q\bar{q} \rightarrow q\bar{q}$	$q\bar{q} \rightarrow q\bar{q}$

Table 6.1: Hard $2 \rightarrow 2$ processes available in the ALPGEN N Jets option. Up to $N - 2 = 4$ final state partons are added to these light quark pairs.

In the initial and final state only the quark types u, d, c and s are considered [47], thus, no b -quarks are included in the QCD multijet background events. However, b -quarks constitute a significant feature of the QCD events. For this reason b -quarks were additionally included in the 4-jet, 5-jet and 6-jet events¹ by replacing a $q\bar{q}$ pair with a $b\bar{b}$ pair in the ALPGEN 4-vectors while keeping the original kinematics. This was only done if the $q\bar{q}$ pair did not originate from the proton structure. Thus, only the u -, d -, s -, c -quark pairs which were additionally added to the light quark pairs from the hard $2 \rightarrow 2$ reaction have been transformed into b -quark pairs. The b -quark events were added to the original background 4-vectors. This procedure is possible as QCD is invariant in terms of the quark flavour and electric charge.

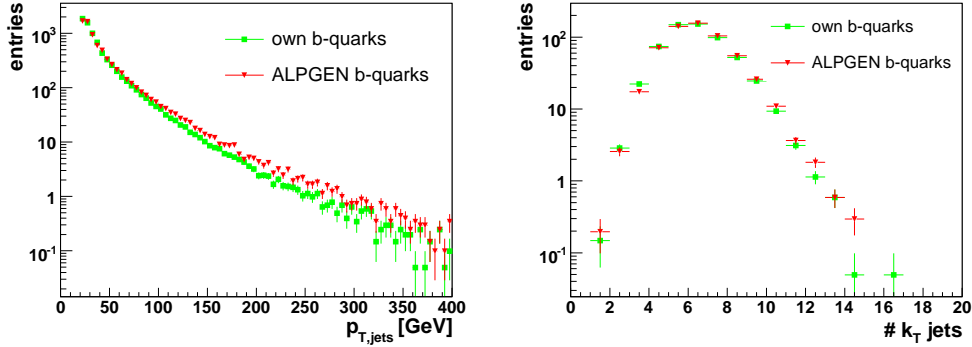


Figure 6.1: Comparison between b -quark events generated by replacing light quark pairs in existing QCD multijet samples ("own" b -quarks, illustrated in green) and b -quark events generated with the ALPGEN $Q\bar{Q}+4$ jets mode (red). The distributions are normalized to the same cross section. Left: Transverse momentum of the jets in the b -quark events. Right: Number of reconstructed k_T jets.

The $Q\bar{Q}+4$ jets mode of ALPGEN, which is also available in version 2.03, effectively provides the same kind of b -quark events apart from the fraction of b -quarks stem-

¹The fraction of b -quarks in the 3-jet QCD samples has not been considered, as the b -quark density in the proton is tiny.

ming from the heavy flavour structure of the proton or from the $gg \rightarrow b\bar{b}$ processes. A comparison between the p_T distributions of the b -quarks produced with the ALPGEN $Q\bar{Q}+4$ jets mode and b -quarks generated by replacing the light quark pairs – which did not originate from the structure of the proton – as described above is shown in Figure 6.1. There is a difference between the two distributions regarding small and especially very high jet- p_T .

The p_T distribution for own b -quark events divided by the distribution for the ALPGEN $Q\bar{Q}+4$ jets mode b -quark events is illustrated in Figure 6.2. As the replacement of the light quark pairs by $b\bar{b}$ pairs produces more soft b -quarks than the ALPGEN $Q\bar{Q}+4$ jets mode, there is a difference at small transverse momenta of the jets.

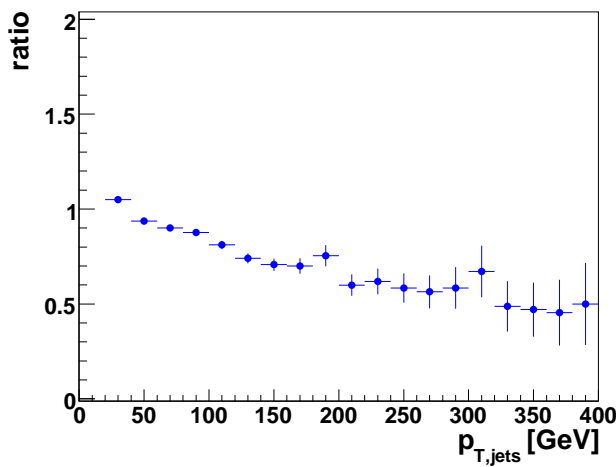


Figure 6.2: p_T distribution for own b -quark events divided by the distribution for the ALPGEN $Q\bar{Q}+4$ jets mode b -quark events for estimating the differences between the different b -quark samples.

The number of reconstructed jets for the two b -quark samples is presented in Figure 6.1 right and shows a slight tendency to a larger number of jets in maximum for the own b -quarks.

The comparison shows that our sample of b -quarks approximately represents – apart from the cross section normalization – the $b\bar{b}+4$ jets sample of ALPGEN. Therefore, it can be used to estimate the background contributions due to b -quarks. Thus, for statistics and time reasons the previous described method of generating b -quarks from the existing ALPGEN QCD multijet 4-vectors has been used for the estimation of the b -quarks in the QCD events.

An additional ALPGEN setting is the choice of one of the three different factorization renormalization scales² Q_0^2 available for the N Jets code, which are shown in Table 6.2 and picked up again in Table 6.3. For the generation of QCD multijet events $iqopt=1$ was chosen, since the $\sum_{jets} p_T^2$ is the only quantity which is experimentally accessible.

²The scale is used for absolute cross section normalization in ALPGEN.

$iqopt$	0	1	9
Q_0^2	1	$\sum_{jets} p_T^2$	\hat{s}

Table 6.2: Choice of factorization and renormalization scale for the N Jets code. The switch $iqopt$ can either be set to 0, 1 or 9 corresponding to a specific value of Q_0^2 , respectively. \hat{s} is the centre-of-mass energy of the hard interaction.

6.1.2 Operational mode and input structure

The ALPGEN generator has the following two main running modes:

- *imode 1*: Calculates the matrix elements on parton level for the selected process using the ALPHA algorithm [49, 50] and produces weighted events – considering phase space information and parton luminosity [47].
For this purpose there are some ”warm-up” cycles³, which are used to examine the distribution of the cross section in the phase space and among the contributing subprocesses [47]. The phase space is parameterized with a multidimensional grid and the weight of each bin of this grid is calculated.
After this warm-up phase an optimized cross section information for phase space and subprocesses is available and serves as an input for the actual generation, where a large statistics run is executed and the final integration takes place producing the matrix element weights which are stored [47].
- *imode 2*: Generates parton level events of unity weight which can be processed further in MC generators providing shower evolution, hadronization and jet reconstruction.
The weighted events are read in and an unweighting is carried out based on the maximum weight of the sample as well as on each event’s weight. The 4-vectors, flavour and colour flow of the events are stored again.

There is also an operational mode 0 where no weighting is available but a total cross section is calculated and histograms can be filled.

The ALPGEN program is steered by means of an input text file containing all information needed by the event generator. Table 6.3 shows an input file for the generation of a sample of weighted events with six final partons [47].

In this context the variable $igrd$ determines the kind of grid chosen for the next integration. The grid mode can be set to 0 which resets the existing grid and starts a new grid optimization, to 1 which starts a new run with the grid information of the previous warm-up run or it can be set to 2 which starts a run based on the optimized grid information from the end of the last generation run.

For the event generation several runs of ALPGEN have been performed. The random seed has been changed for each run to generate different events.

³The number of warm-up iterations can be chosen by the user (see Table 6.3).

Input	Meaning
1	Run mode (<i>imode</i>)
sixjet	Name of output file
0	Grid mode (<i>igrd</i>)
1000000 6	Number of events to iterate, number of iterations
100000000	Number of events for final integration
<i>njets</i> 6	Number of jets in final state
<i>ih2</i> 1	Collision type (proton-proton)
<i>ebeam</i> 7000	Beam energy in centre-of-mass frame
<i>ickkw</i> 1	Enables parton matching Uses CKKW scale for α_s in matrix element
<i>iqopt</i> 1	Factorization and renormalization scale
<i>ndns</i> 7	Parton density function (CTEQ6M)
<i>ptjmin</i> 20	Minimum p_T [GeV] for light jets
<i>drjmin</i> 0.699999988	Minimum ΔR between two jets
<i>etajmax</i> 2.5	Maximum $ \eta $ for light jets
<i>iseed1</i> 15515	Seed of first random number

Table 6.3: Input variables for the generation of a weighted six-parton sample. Note, that within the ALPGEN program final state partons are referred to as jets.

6.1.3 Jet – parton matching

A very important step in the simulation of the QCD background events is the jet-parton matching, which permits the generation of inclusive samples with any jet multiplicity. A lot of events are lost during the matching procedure and thus, the optimal settings for the simulation have to be found in order to minimize both the loss of events and the time needed for generating a given number of events.

For the matching of partons from the matrix elements with jets, found after applying a parton shower [47], according to the MLM-matching [51] the following steps of event generation were done⁴:

- Samples with weighted events were generated with *imode* 1, where the parameter *ickkw* (see Table 6.3) had to be set to value 1 [47].
- With *imode* 2 unweighted events were created, the *ickkw*=1 setting is taken again automatically.
- The unweighted events were processed through a parton shower generator providing shower evolution. In the case of this study PYTHIA 6.2 [13] was used

⁴For the MLM-matching the default configurations $E_{T,clus} = ptjmin$ and $R_{clus} = \Delta R(jet, jet) = drjmin$, as listed in Table 6.3, were chosen.

for the generation of the parton shower. The events were clustered with a jet algorithm⁵ and the jet-parton matching⁶ was performed before hadronization took place.

A jet can only be matched to one parton. Events which fail the matching are rejected, where "fail" means that the matching in either energy or direction of the parton and the parton jet fails.

In the inclusive case an event is kept if all matrix element partons are allocated to jets. If two partons match to the same jet or if one parton does not match the event is rejected [52].

For exclusive samples⁷ all partons have to match to jets [53]. When there is an extra jet which is not matched to any parton [52] the event is discarded.

In this context it should be mentioned that the routine UPVETO in ALPGEN (alpsho.f) has been modified. To increase the number of accepted events in exclusive mode, each rejected event was offered several times to the parton shower generator⁸. This way a sufficient number of QCD events could be generated within an acceptable period of time. However, this method implies that certain areas of the phase space are weighted too high. Thus, each event has to be reweighted by a factor of $\frac{1}{\text{Number of offers}}$ (we are grateful to [54] for pointing this out). Nevertheless, this factor can be neglected if the number of events with more than one additional offer is small, which is indeed the case (see Figure 6.3).

Further information concerning this topic can be found in Section 7.1.

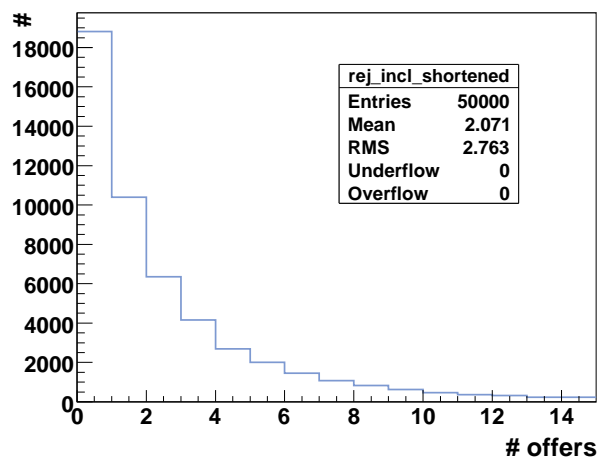


Figure 6.3: Number of offers in inclusive QCD 6-jet events. The predominant fraction of events was accepted after one iteration.

⁵The matching procedure is designed for jets which are clustered with the Cone algorithm.

⁶For the jet-parton matching PYTHIA version 6.322 was linked as in PYTHIA 6.2 the matching procedure is not yet implemented.

⁷In this context *exclusive* means that the jet multiplicity of the sample exactly corresponds to the number of partons from the matrix element.

⁸Up to 15 iterations have been allowed in maximum.

The matching procedure has been carried out for the production of the QCD multi-jet background events where different samples with three to six partons⁹ have been created. The further processing of the background events as well as the simulation of fully hadronic $t\bar{t}$ events with the PYTHIA Monte Carlo generator is outlined in the following section.

6.2 PYTHIA 6.2

The PYTHIA Monte Carlo generator [13] is a multipurpose generator, which is commonly used for the simulation of hadronic processes. It can generate detailed events which can then be compared to real data [13].

PYTHIA is a leading-order (LO) generator, which means that all events are calculated in leading and lowest order. Higher corrections can only be considered via the leading-log parton shower. Next-to-leading-order (NLO) calculations are not implemented, thus, the 4-vectors of the QCD multijet background events – which are proportional to higher orders of the strong coupling constant α_s – were simulated in ALPGEN. The matrix element for the fully hadronic $t\bar{t}$ events, however, is proportional to α_s^2 and thus, the fully hadronic $t\bar{t}$ events were completely simulated with PYTHIA.

6.2.1 Simulation of $t\bar{t}$ multijet events

For this study PYTHIA 6.2 was configured to generate pp events with a centre-of-mass energy of $\sqrt{s} = 14$ TeV corresponding to the centre-of-mass energy expected at the LHC. The right choice of PYTHIA switches allows the production of top and antitop with massive matrix elements and their decay into a pair of W bosons and two b -quarks. The W bosons themselves were forced to decay into pairs of quark and antiquark resulting in a fully hadronic $t\bar{t}$ event, as shown in Figure 6.4.

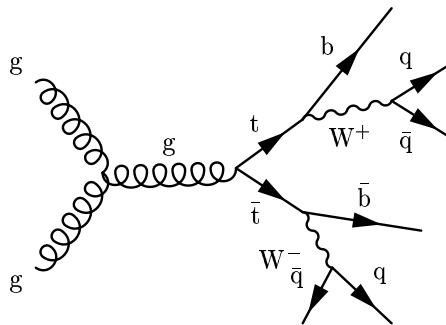


Figure 6.4: Feynman diagram of a $t\bar{t}$ pair decaying in the fully hadronic mode.

⁹The samples with three, four and five final partons have been simulated in exclusive mode. The six-jet sample, however, is an inclusive sample, thus allowing six or more partons in the final state.

The whole range of switches applied to simulate and configure the particle process investigated is illustrated in Table 6.4, where the first column denotes the name of the switch and the second one indicates what configuration is chosen by the switch.

Switch	Function
MSUB(81,1)	Subprocess $q\bar{q} \rightarrow Q\bar{Q}$
MSUB(82,1)	Subprocess $gg \rightarrow Q\bar{Q}$
MSEL(6)	$t\bar{t}$ production with massive matrix elements
MDME(46,1)	$t\bar{t} \rightarrow W^+bW^-\bar{b}$
MDME(190,1)	$W^+W^- \rightarrow \bar{d}u\bar{u}d$
MDME(191,1)	$W^+W^- \rightarrow \bar{d}c\bar{c}d$
MDME(192,1)	$W^+W^- \rightarrow \bar{d}t\bar{t}d$
MDME(194,1)	$W^+W^- \rightarrow \bar{s}u\bar{u}s$
MDME(195,1)	$W^+W^- \rightarrow \bar{s}c\bar{c}s$
MDME(196,1)	$W^+W^- \rightarrow \bar{s}t\bar{t}s$
MDME(198,1)	$W^+W^- \rightarrow \bar{b}u\bar{u}b$
MDME(199,1)	$W^+W^- \rightarrow \bar{b}c\bar{c}b$
MDME(200,1)	$W^+W^- \rightarrow \bar{b}t\bar{t}b$

Table 6.4: Switches for the simulation of $t\bar{t}$ multijet events with PYTHIA.

In addition, some kinematic and topological cuts have been applied, which are listed in Table 6.5 and which hold for both the $t\bar{t}$ and the background events (see Section 6.2.2).

Switch	Function
CKIN(3,100.)	Lower range of p_T for hard $2 \rightarrow 2$ process
MSTP(81,0)	Master switch for multiple interactions (off)
MSTP(61,1)	Initial state radiation (on)
MSTP(71,1)	Final state radiation (on)
MSTP(52,2)	Choice of parton distribution function library
MSTP(51,4057)	Parton distribution set (CTEQ6M)

Table 6.5: General switches for the configuration of PYTHIA.

By the use of CKIN(3,100.) the lower limit of the p_T -transfer in hard $2 \rightarrow 2$ processes was fixed¹⁰ to 100 GeV corresponding to a cut in the phase space. The resulting

¹⁰Generally, a cut on the lower limit of the momentum transfer in the hard interaction is necessary as the differential cross section is divergent for $p_T \rightarrow 0$ [13].

limitation of the phase space leads to a – by about factor two [13] – diminished production cross section for the $t\bar{t}$ events in comparison to the cross section of the $t\bar{t}$ events generated with a much lower p_T limit [13] (see also Section 7.2.2 and Appendix A) and compared to the $t\bar{t}$ cross section predicted for the LHC [38]. Besides, PYTHIA provides only LO calculations. The cross section estimation of fully hadronic $t\bar{t}$ events at the LHC is a NLO estimation, though. The difference between the cross sections in LO and NLO for $t\bar{t}$ events is illustrated in Figure 6.5. Especially for gluon initiated processes, which are the main production processes for $t\bar{t}$ events at the LHC, there is a deviation of up to 100 % between LO and NLO calculations, as outlined in [55]. Hence, there is a difference between the predicted cross section [38] and the one obtained from the PYTHIA simulation.

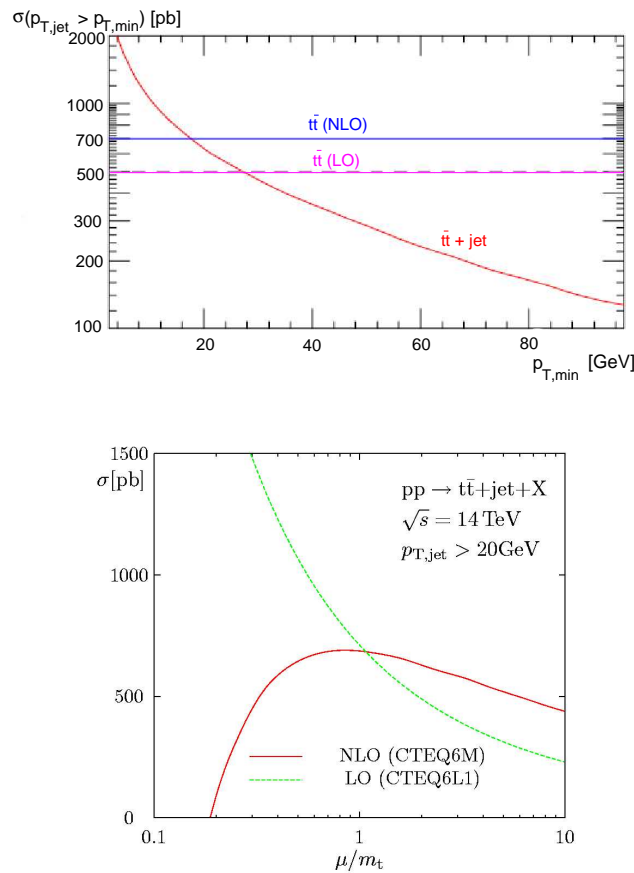


Figure 6.5: Illustration of the differences between LO and NLO for $t\bar{t} + jet$ events at the LHC. Top: Dependence of the LO $t\bar{t} + jet$ cross section on the parameter $p_{T,min}$ (red) which defines the additional jet and $t\bar{t}$ production cross sections at LO (magenta) and NLO (blue) [56]. Bottom: LO and NLO cross sections for $t\bar{t} + jet$ production plotted for the renormalization and factorization scale μ which is divided by the mass of the top quark m_t [57]. With the NLO corrections the scale dependence is reduced by far.

With switch MSTP(52,2) the PDFLIB [58] was selected as library for the parton density functions, where MSTP(51,4057) chooses the CTEQ6M [18, 59] NLO pro-

ton structure function from PDFLIB¹¹. This function is the latest available version of PDFLIB distribution functions and was obtained by means of adaptation to the current structure function data using improved theoretical calculations.

Once all settings have been made the events can be simulated. PYTHIA acts as a slave system [13] which means that the main program, configured by the user, calls all sub-routines needed for the simulation.

At this point parton shower and hadronization¹² are applied to the events. The parton shower involves an operation of the kind $a \rightarrow bc$ with a being the mother particle and b, c the daughter particles. The daughter particles themselves can split again into several particles. Further information concerning the explicit calculation of the parton shower and the corresponding evolution equations can be found in [13].

After the execution of the subroutines full control is given back to the main program. Now a jet clustering of all stable (charged and neutral) particles including neutrinos with the k_T algorithm [40] is provided within the main program. This step does not belong to the actual generation of the events and has been added additionally to the main PYTHIA program for simplifying matters. The jet reconstruction step is only carried out for the analysis of the events on generator level. The jet reconstruction for the events containing among others detector and b -tagging information has been performed using ATLFast within the Athena environment (see Section 6.3.2).

At the end of the generation PYTHIA delivers a ROOT file [60] or a "hepevt data file" [61] with all information about the particles (and jets) needed for a further processing and analysis of the $t\bar{t}$ events. The results of this analysis can be found in Section 7.2 and 7.3.

6.2.2 Reprocessing of QCD multijet background events

In Section 6.1 the generation of the 4-vectors of QCD background events (see Figure 6.6) has been described, which have to be processed further in PYTHIA. For processing these events several settings have to be made - apart from the ones already listed in Table 6.5.

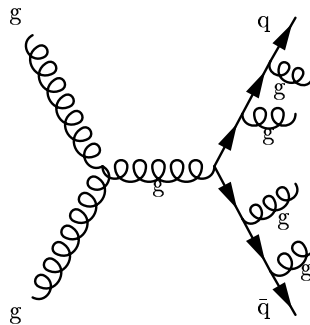


Figure 6.6: Example of a Feynman diagram for a QCD background event with six jets in the final state. The two quarks in the final state radiate gluons. This way six or more jets in final state can be produced.

¹¹The CTEQ6M parton density function is not contained by default in the PDFLIB but it was implemented especially for this thesis.

¹²The hadronization is described in Section 2.3.

With MSTP(143,1) (see Table 6.6) subroutine UPVETO is called in the event generation chain from inside the PYEVNT routine [13] and the user can decide if the current event is rejected or not. For this step a later version of PYTHIA (PYTHIA 6.322) has been used as PYTHIA 6.2 does not yet contain the possibility of a further processing of ALPGEN 4-vectors using UPVETO. MSTP(82,0) defines the structure of multiple interactions. In this case a simple two-string model without any hard interactions was used (toy model) [13].

After all PYTHIA has to be started with a modified call of the PYINIT subroutine assuring the full user control of the simulated process, finally. Now the 4-vectors of the ALPGEN events are read in and are processed through the shower evolution. The jet-parton matching (MLM-matching [51]) using PYTHIA 6.322 takes place and many events are rejected as the partons could not be unequivocally allocated to jets (subroutine UPVETO).

After the parton shower, hadronization and jet algorithm¹³ are applied to the events, as already outlined in the previous section. Again, at the end of the run a ROOT file or a hepevt data file is produced allowing the analysis of the completed background events.

Switch	Function
MSTP(82,0)	Structure of multiple interactions
MSTP(111,1)	Master switch for fragmentation and decay (on)
MSTP(143,1)	Calling of UPVETO

Table 6.6: Settings for processing ALPGEN background events in PYTHIA.

6.3 Athena - an ATLAS framework

Athena is the fully object-oriented ATLAS software framework, designed for data processing, simulation, reconstruction and physics analysis. It is currently being developed by the ATLAS collaboration and is completely written in C++ and Python [62].

Athena is based on the Gaudi framework [63], thus benefiting from the software experience of many other hadron collider experiments. As Gaudi is not dependent on external technologies (especially storage technologies) [64] the Athena framework is supposed to be almost independent from any changes in related external software and technology that may occur and is hence expected to run for many years.

The Athena framework is based on the *joboptions concept*, which is illustrated in Figure 6.7. When the user starts Athena he has to specify a joboptions file which is read by the application manager. This is the only service which is called in the Athena executable [65]. All other components are directly controlled via joboptions files. The files are written in the Python programming language and allow to modify diverse

¹³Jet reconstruction is again only applied for the generator-level events. The actual jet reconstruction was performed during the further processing of the 4-vectors in ATLFAST 11.0.41, as described in Section 6.3.2.

parameters interactively [65].

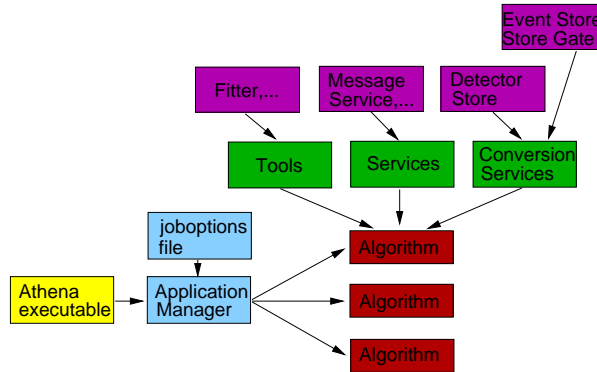


Figure 6.7: Concept of the Athena Framework. Each operation is started from the Athena executable. A lot of components are available, all being accessible and configurable via joboptions files [65].

Detailed information about the Athena framework can be found in [64, 65]. A lot of different software packages are available in the Athena environment. Each fulfills specific tasks of generation, reconstruction, or analysis of events. The following subsections outline the packages used for the simulation, conversion and analysis of the $t\bar{t}$ and background events. A whole chain of packages was needed in order to combine the events with all information needed and to get them ready for the final analysis and comparison.

As the Athena framework is under constant development, there are several Athena versions available. This thesis is based on Athena version 11.0.41.

6.3.1 Transformation of PYTHIA events for further processing in Athena

In order to handle the $t\bar{t}$ and background events, which were processed with PYTHIA, within the Athena environment they must be converted into a format Athena software can further process. This is the so-called POOL format. For this purpose the PYTHIA 6.2 events were converted to hepevt data format via a call to the HEPEVT subroutine of PYTHIA. This file contains all the necessary information – including the particles’ 4-vectors – of the generated events. The hepevt files can be read in by means of the jobOptions.hepevt.py file which belongs to the Athena *ReadEventFromFile*¹⁴ package. The events are again converted and written into a POOL file which can be run by most other software packages in the framework and which provides the input for the further processing of the events.

6.3.2 ATLEFAST - a software package of the Athena framework

PYTHIA can only simulate events on generator level, it provides no information about the detector itself. However, to compare the theoretical predictions with real data the

¹⁴*Generators/GenAnalysisTools/ReadEventFromFile/*

impact of the detector needs to be investigated. For this purpose a simulation program is needed which simulates the response of the detector's components to the physics processes under examination. As a consequence, the events attained are in the same format like real data and can be compared with the results from plain PYTHIA 6.2 (generator level events) in a next step.

The ATLFAST simulation program [66, 67] is a fast simulation of the ATLAS detector. It can run any generator that operates within the framework [66]. Thus, the Athena ATLFAST software package¹⁵ was used to simulate $t\bar{t}$ events by calling PYTHIA 6.323 attached to the Athena environment (by means of the `Atlfast_RunPythia.py` joboptions file), resulting in "ATLFAST $t\bar{t}$ events". In addition, the POOL files with $t\bar{t}$ and background events, generated with PYTHIA¹⁶ 6.2 stand-alone, were read in and were processed through ATLFAST ("PYTHIA $t\bar{t}$ events" and background events). This way the events were additionally combined with the simulation of the ATLAS detector.

The ATLFAST package simulates jet reconstruction in the calorimeter, momentum and energy smearing for leptons and photons, magnetic field effects as well as missing transverse energy [67]. In this context the jet reconstruction was done with the k_T algorithm [40] in the exclusive mode¹⁷ with a fixed cut-off parameter d_{Cut} and resolution parameter D of unity. As input to the jet reconstruction calorimeter cell entries¹⁸ as well as tracks of charged particles have been used¹⁹. Further information concerning the settings of the k_T algorithm within ATLFAST can be found in Section 7.2.1.

In summary, the detector parameters are adjusted to the real expectations in terms of the ATLAS detector, although the fast simulation package cannot provide all details of the detector as only the basic parametrization is implemented [67]. A more accurate detector simulation can only be obtained via a full simulation of events using GEANT 4 [68].

In addition to the simulation of the fundamental detector parameters the ATLFAST package provides b -quark tagging information, which is a crucial tool for distinguishing $t\bar{t}$ and background events, as it is described in Chapter 8. In this context a k_T -jet was regarded as b -quark jet when the combined likelihood for a b -tagged jet had a value of $combinedLH > 0.025$ and the combined b -tagging weight exceeded $w_{cmb} > 0$.

When generating fully hadronic $t\bar{t}$ events with ATLFAST, parton shower and hadronization are provided via the PYTHIA 6.323 generator – which Athena accesses – as it is the case for the stand-alone simulation of events with PYTHIA 6.2. In this regard it should be mentioned that PYTHIA 6.323 has been configured via the `Atlfast_RunPythia.py` joboptions file, thus running with exactly the same settings as PYTHIA 6.2 stand-alone.

ATLFAST contains several Athena-Algorithms which are run in a given order and has ntuples or Analysis Object Data (AOD) output which contains the smeared objects [66]. AOD are a reconstructed data format allowing a further analysis of the

¹⁵`Simulation/Atlfast/AtlfastAlgs/`

¹⁶and PYTHIA 6.322 for the MLM-matching.

¹⁷A small fraction of the QCD multijet events has also been reconstructed with the Cone Algorithm in standard setting with a Cone size of $R = 0.4$. Further information can be found in Appendix B.

¹⁸For the calorimeter cell events the minimum transverse energy of the cells has been increased from $E_{T,cell} = 0$ GeV to $E_{T,cell} = 1$ GeV to remove the lowest energetic cell entries which are caused by electronic noise.

¹⁹Events reconstructed with the Cone algorithm use only calorimeter cell entries as input for the jet reconstruction.

events with certain Athena AOD analysis programs, as outlined in the following section. They are only readable within the Athena framework, thus providing not full access to the event information using ROOT. Further information regarding the structure of the ATLFAST package can be found in [66, 67, 69].

6.3.3 AOD analysis with AnalysisSkeleton

As soon as the events are written in AOD format they can be transformed and analyzed with the AnalysisSkeleton code belonging to the UserAnalysis software package²⁰. This program grants access to the different ATLFAST containers (objects of the ATLFAST generator) storing information of each jet, b -quark jet and particle of the events and can be run via the AnalysisSkeleton.joboptions.py file. The extracted information is stored in Athena Aware NTuples (AANTs) [70], which can be read by Athena and also by ROOT, now providing the full set of characteristics of fully hadronic $t\bar{t}$ and background events including detector parameters. This information serves as input for selection cuts – see Chapter 8 – separating the signal from the background events and poses the final data output of the chain of Athena software packages used for this thesis.

6.3.4 Athena Full Simulation

As already discussed ATLFAST and in general fast simulation can only provide a coarse description of the ATLAS detector. However, the detailed simulation of the detector is a major task when simulating particle physics events. Thus, a full simulation based on GEANT 4 [68] was used which makes use of the Athena framework and provides a very detailed implementation of the four main subdetectors (inner tracker, electromagnetic and hadronic calorimeter, muon system) in ATLAS [71]. Thereby, the emphasis is set on the geometry description of the detector components, whereas a perfect detector with no dead channels or any misalignment is assumed so far [72]. The full simulation is organized in four different steps:

- 1) **Event Generation:** In this step the events are generated with a Monte Carlo generator, e.g. PYTHIA, as described in the previous section.
- 2) **Simulation:** Here a detailed tracking of particles through the detector material including detailed simulation of the interactions of the particles with the material is provided for the events which were generated in step 1.
- 3) **Digitalization:** This part of the full simulation provides the detector's response on the particle interactions – simulated in step 2 – and the simulation of measurable signals. After this step the simulated data has the same format as real data.
- 4) **Reconstruction:** The reconstruction of the particle tracks and a clustering (i.e. 4-momenta) is carried out using the information obtained from the digitalization and the other previous steps.

²⁰*PhysicsAnalysis/AnalysisCommon/UserAnalysis/*

An overview of already produced events is given by a certain webpage [73]. For this analysis two fully simulated datasets²¹ have been checked out for being able to compare the full simulation with the results obtained from the events processed in ATLFAST. However, all top physics analyses which have already been performed with fully simulated events agree quite well with results from the fast simulation [72]. Consequently, even a rather simplified simulation of the detector, which is available in ATLFAST, provides accurate kinematic distributions. The differences in the detector description between full and fast simulation seem to be negligible compared to effects of particle radiation, hadronization and reconstruction [72]. As a consequence, fast simulated events can be expected to be fully sufficient to study the physics of this analysis.

6.4 Implementation of the jet reconstruction algorithm in PYTHIA 6.2 (stand-alone) and in the Athena environment

As already discussed jet reconstruction at hadron colliders is widely done with the Cone algorithm. Nevertheless, this analysis uses the k_T algorithm by default for jet clustering, as described in Chapter 5. This poses a problem when comparing self-generated events with events from full or fast simulation. Though the k_T algorithm is implemented in Athena software, it is differently configured leading to different jet reconstruction and thus, to events which are quite difficult to compare. Table 6.7 shows an overview of the standard implementation of the k_T algorithm in PYTHIA 6.2 stand-alone, ATLFAST 11.0.41 and in full simulation.

Setting	Full simulation	ATLFAST	PYTHIA 6.2 stand-alone
Reconstruction	Inclusive	Inclusive	Exclusive
Resolution	ΔR	ΔR	ΔR
Recombination	E	E	E_T
Resolution D	1.0	1.0	1.0
Input	Calorimeter cells	Calorimeter cells	Particles

Table 6.7: Standard implementation of the k_T algorithm in PYTHIA 6.2 stand-alone and ATLAS software.

In PYTHIA 6.2 the k_T algorithm was implemented in exclusive mode with an optimized cut-off parameter of $d_{\text{Cut}} = 450 \text{ GeV}^2$. This is the default reconstruction mode for collider experiments with non-elementary particles (like proton-proton collisions

²¹The fully simulated datasets are the two `csc11` samples: `csc11.005204.TTbar_FullHad_McAtNlo_Jimmy.recon.AOD.v11004107` and `csc11.005204.TTbar_FullHad_McAtNlo_Jimmy.recon.AOD.v11004205`, where the last number in the file name refers to the Athena version used for data reconstruction.

at the LHC) where a soft beam remnant remains at the end of the particle collision, which has to be separated from the actual jets.

ATLAS software, however, uses the k_T algorithm in inclusive mode allocating accidentally the soft beam remnants to jets. This difference leads to a higher jet multiplicity in Athena events making it very difficult to draw conclusions when comparing these two kinds of events.

In addition, the input for the jet reconstruction in PYTHIA 6.2 are all stable particles produced (charged and neutral) leading to a very accurate reconstruction. Jet reconstruction via the energy depositions in the calorimeter cells, however, as it is done in ATLFAST and full simulation, suffers from effects due to detector granularity and resolution.

Given the different standard settings for the k_T algorithm in PYTHIA 6.2 stand-alone and Athena software it was necessary to change the default settings for the algorithm in Athena software to parameters which are comparable to the settings in PYTHIA 6.2 and which correspond better the case of dealing with proton-proton collisions. This way it became possible to run the jet algorithm in ATLFAST in exclusive mode and to use charged particle tracks (with $d_{\text{Cut}} = 200 \text{ GeV}^2$) in addition to calorimeter cells ($d_{\text{Cut}} = 550 \text{ GeV}^2$, see also Section 7.2.1) as input for the reconstruction. Supplementary, the recombination scheme in ATLFAST was switched to "E_T". This leads to a quite good agreement of results from the k_T implementation in PYTHIA stand-alone and in ATLFAST.

The parameter choice for the jet reconstruction in the full simulation cannot be changed retrospectively, except the events are reprocessed with modified settings. Thus, events from full simulation are not directly comparable to the ATLFAST and PYTHIA 6.2 events (see also Section 7.2.4).

Chapter 7

Study of fully hadronic $t\bar{t}$ events and QCD multijet background events

7.1 Modified subroutine UPVETO

As outlined in Section 6.1.3 the subroutine UPVETO in ALPGEN was modified, thus offering rejected events several times¹ to the parton shower generator during the jet-parton matching (MLM-matching [51]). This procedure holds the risk of forcing events which are rejected and offered too often (see Section 6.1.3).

Figure 7.1 left shows the number of offers for an exclusive (magenta line) and an inclusive (blue line) 6-jet background sample for a total number of 50000 events.

While in the exclusive case each event needs an average number of five iterations, more than 70 % of the inclusive events are accepted after one iteration, thus causing only a negligible reweighting of the events for the inclusive case.

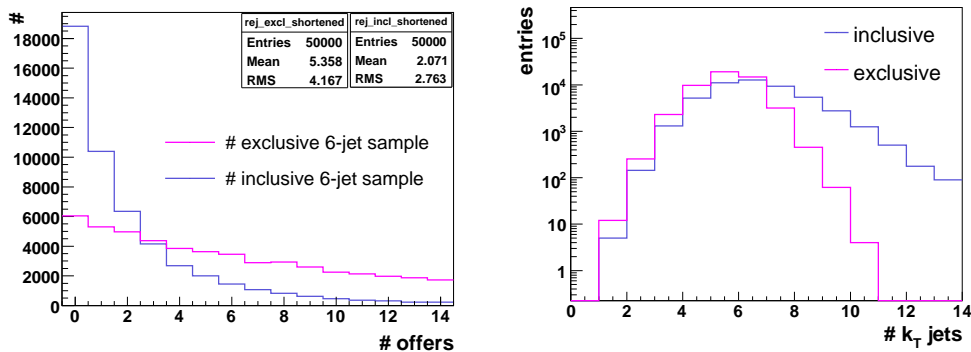


Figure 7.1: Left: Number of offers in inclusive and exclusive QCD 6-jet events. The predominant fraction of inclusive 6-jet events was accepted after one iteration. In exclusive mode many iterations were necessary until an event was accepted. Right: Number of reconstructed jets in an inclusive and an exclusive 6-jet background sample.

¹Up to 15 iterations have been allowed in maximum.

Figure 7.1 right presents the number of reconstructed jets for an inclusive and an exclusive 6-jet background sample. In the inclusive case the parton shower considers logarithmic corrections due to larger jet multiplicities resulting in the shift to the larger number of reconstructed jets in Figure 7.1 right. Therefore, and due to the high efficiency of event generation plus the negligible impact from the iterated shower matching in UPVETO, an inclusive 6-jet sample was chosen for the description of the main QCD background.

Figures 7.2 and 7.3 compare different distributions for an inclusive 6-jet QCD sample with and without iterative shower matching in UPVETO. Figure 7.2 left shows the jet multiplicity, Figure 7.2 right illustrates the sum of the momenta of the six leading jets in the event. Figure 7.3 represents the distributions for the event shapes sphericity and aplanarity [74].

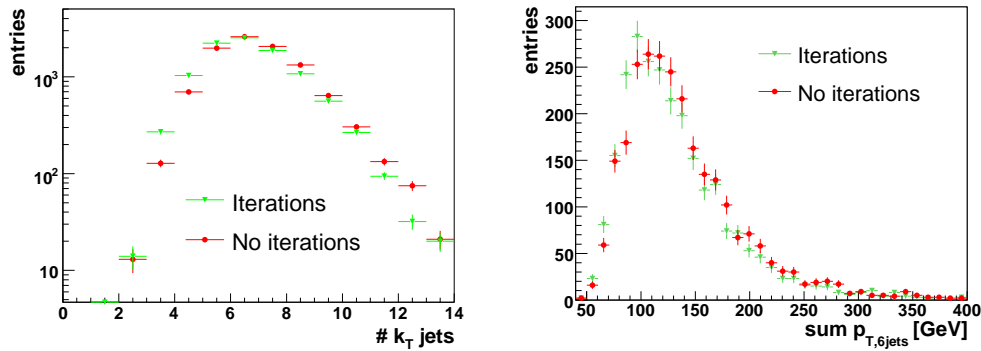


Figure 7.2: Distributions for modified routine UPVETO (iterations) and for the standard setting of UPVETO (no iterations) for inclusive QCD 6-jet events. Left: Jet multiplicity with mean multiplicity of 6.2 for the sample with iterations and mean multiplicity of 6.5 for the sample without iterations. Right: $\sum p_T$ of six jets. In both histograms the green distribution prevails the red one only at the small values, which means that the modified routine UPVETO overrates the collinear final states which comprise merely small jet multiplicities.

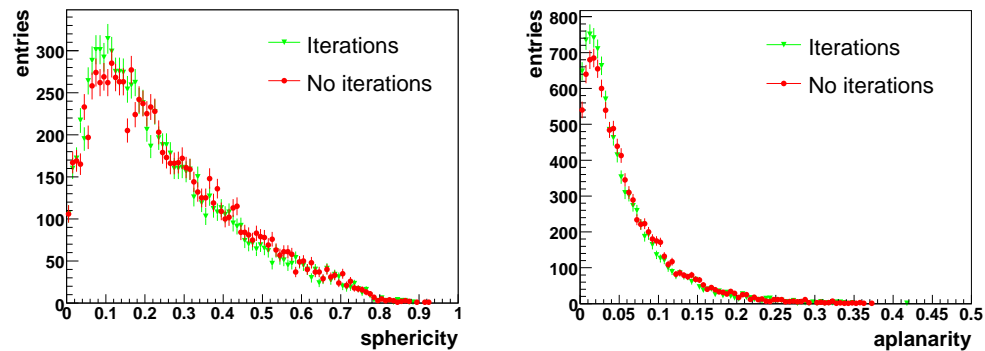


Figure 7.3: Distributions for modified routine UPVETO (iterations) and for the standard setting of UPVETO (no iterations) for inclusive 6-jet events. Left: Sphericity. Right: Aplanarity.

The noticeable differences in the distributions for the two different modes of UPVETO appear in ranges of the observables where lower jet multiplicities dominate the "6++" jets. This is consistent with the appearance of the differences only at small values of the corresponding distributions in Figures 7.2 and 7.3.

For the remaining QCD background events (3-, 4- and 5-jet) one would naively expect that a lower fraction of events should be rejected during the MLM-matching due to the smaller number of final state partons. However, in order to avoid double-counting of multi-parton final state cross sections, exclusive samples were chosen for the 3-jet, 4-jet and 5-jet QCD events, respectively. The fixed number of final state partons in these samples makes the jet-parton matching much more selective, rejecting substantially more events than in inclusive samples and thus facing partly a loss of 90% of the events. For this reason the subroutine UPVETO was used again in iterative mode.

The resulting distributions for modified UPVETO, as shown in Figure 7.4 for 5-jet QCD events, remain almost the same as for standard UPVETO displaying again only differences in ranges of the observables where lower jet multiplicities dominate. Thus, the several offers of an event, needed to be accepted by the parton shower generator, affect exclusive 3-, 4- and 5-jet QCD events only marginally in regions of the phase space where the partons are not very collinear².

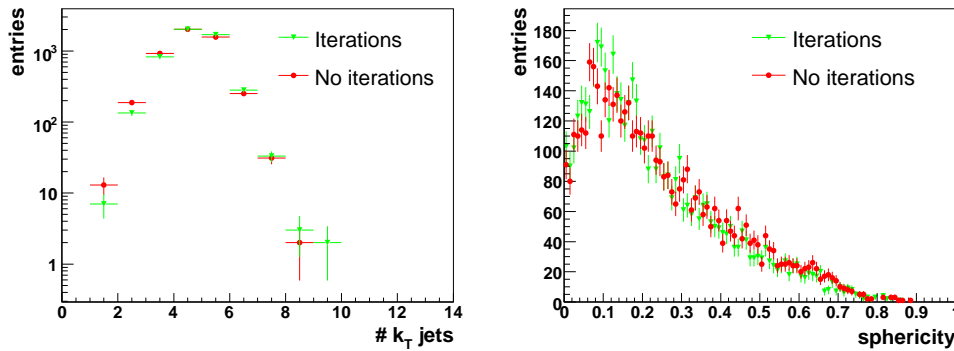


Figure 7.4: Left: Jet multiplicity for an (exclusive) 5-jet QCD sample for modified (iterations) and standard UPVETO (no iterations). Right: Sphericity distribution for the 5-jet QCD events with and without iterations.

7.2 Fully hadronic $t\bar{t}$ events and QCD multijet background events within the Athena environment

7.2.1 Determination of the cut-off parameter d_{Cut}

When processing the 4-vectors of the $t\bar{t}$ and background events with ATLFAST [66,67] version 11.0.41, the jet reconstruction was done with the k_T algorithm in exclusive mode, thus with a fixed cut-off parameter d_{Cut} , as described in Chapter 5.

ATLFAST enables to investigate charged particle tracks and calorimeter cell entries

²As outlined in Section 5.3, "collinear" denotes that the angle between radiating and radiated particle is very small.

separately as input for the jet reconstruction. Both options have been considered in this thesis³ and for both cases the optimal value for the cut-off parameter had to be found to reconstruct as many $t\bar{t}$ events with six final jets, as possible.

Finding the optimal value of d_{Cut} is crucial for the reconstruction of the jets and the further analysis of the events. If the cut-off parameter is set to a value which is too large ($d_{\text{Cut}} \rightarrow s$) the jet multiplicity in the events will be close to unity as the size of the jets rises with increasing d_{Cut} , as described in Section 5.2.3. On the other hand, if d_{Cut} is too small as it might be the case for a value close to Λ_{QCD}^2 , the k_{T} algorithm will stop before several objects could have been recombined to jets. This leads to events with too many jets in final state (see 5.2.3). Therefore, care must be taken on the determination of the d_{Cut} values.

For the determination of the cut-off parameter the d_{Cut} distributions for the cases when seven jets turn into six jets ($7 \rightarrow 6$) and six jets turn into five jets ($6 \rightarrow 5$) were regarded for both jets from calorimeter cells and tracks. The corresponding distributions are illustrated in Figure 7.5 for fully hadronic $t\bar{t}$ events. The distributions show the smallest d_{Cut} values possible to reconstruct the given number of jets. At the next smaller value the number of jets would amount to the next higher jet multiplicity. The number of final jets decreases with rising d_{Cut} . Thus, at large d_{Cut} values the 6-jet final state, illustrated by the green distribution in Figure 7.5 left and right, prevails.

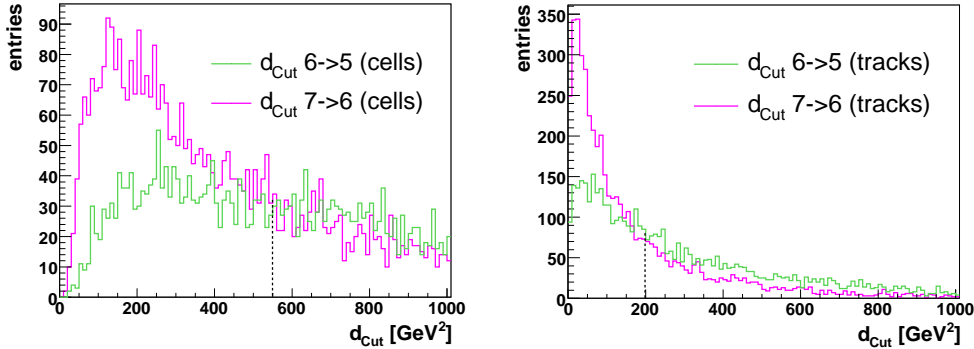


Figure 7.5: Determination of cut-off parameter d_{Cut} for fully hadronic $t\bar{t}$ events. Left: d_{Cut} distributions for a jet reconstruction from calorimeter cell entries. Right: d_{Cut} distributions for a jet reconstruction from charged particle tracks. The black line marks the position of the chosen cut-off parameter, respectively.

For the jets reconstructed from calorimeter cell entries (Figure 7.5 left) the transition from the 7-jet to the 6-jet final state happens at d_{Cut} values of about $500 - 600 \text{ GeV}^2$. Therefore, a value of 550 GeV^2 was chosen for the reconstruction of fully hadronic $t\bar{t}$ events with six jets in the final state. At this value an equal number of events with seven and six jets, respectively, is expected. At a larger d_{Cut} more of the green distribution ($6 \rightarrow 5$) than of the magenta distribution ($7 \rightarrow 6$) would get lost, while for smaller d_{Cut} values the opposite occurs.

For the reconstruction from charged particle tracks, however, the 6-jet final state starts prevailing the 7-jet final state already at d_{Cut} values of about 200 GeV^2 . Thus, a value

³For further information concerning the differences between the two options see Section 7.2.3.

of 200 GeV^2 was chosen as cut-off parameter for the jet reconstruction from tracks, indicated by the black line in Figure 7.5.

There seems to be a large difference between the two values for the cut-off parameter. But the *charged* particle tracks include only the charged particles in an event, thus a fraction of $\frac{2}{3}$ of all particles. Therefore, when comparing the cut-off parameter of the tracks with the d_{Cut} value for the cells the track- d_{Cut} must be multiplied with a factor of $(\frac{3}{2})^2$, accommodating to the neutral particles included in the cells⁴. In doing so the cut-off parameter for the charged particle tracks would amount to a value of 450 GeV^2 .

In addition, there is a difference in the d_{Cut} values for tracks and cells due to an imprecise reconstruction of the calorimeter cell entries in ATLFASST. In fact, when a particle hits the calorimeter cell the entry is always shifted to the centre of the cell as if the particle hit the cell-centre itself. This leads to an additional p_T contribution for each particle and thus, to larger d_{Cut} values for the calorimeter cell entries.

Taking these reasons into account the two cut-off parameters for the jet reconstruction from calorimeter cell entries and charged particle tracks agree.

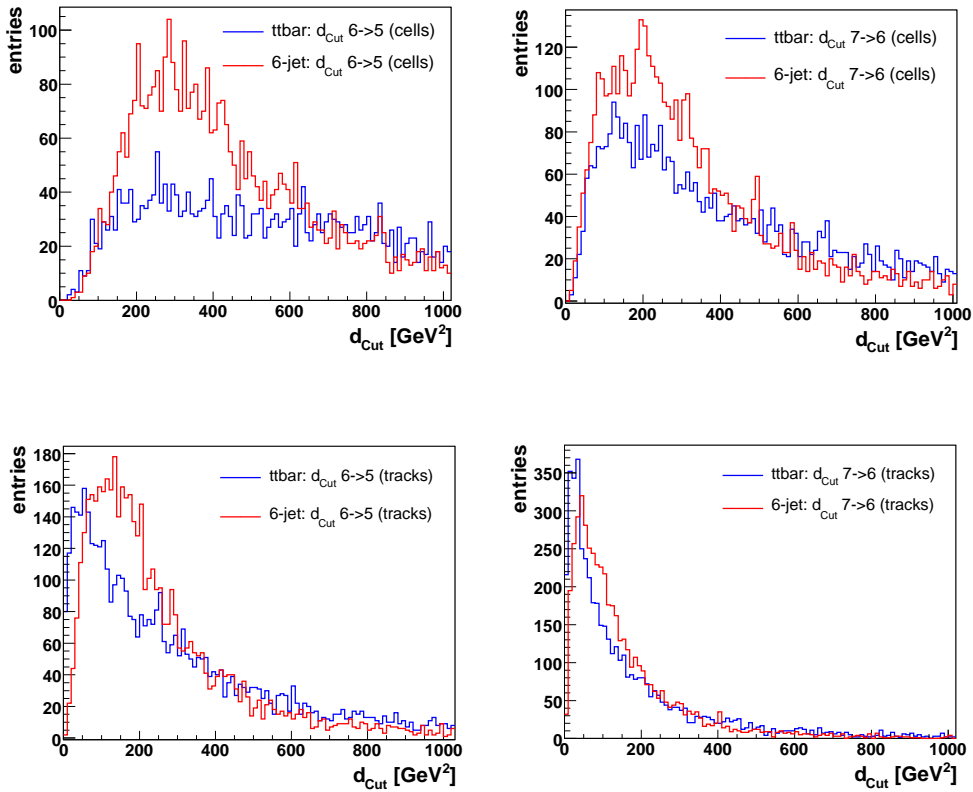


Figure 7.6: Comparison of d_{Cut} values for fully hadronic $t\bar{t}$ (blue) and 6-jet background events (red) reconstructed from calorimeter cell entries (top) and charged particle tracks (bottom). Left: d_{Cut} for the case $6 \rightarrow 5$ jets. Right: $7 \rightarrow 6$ jets.

⁴The factor $\frac{3}{2}$ comes from the strong isospin symmetry yielding a number ratio of charged and uncharged pions: $\frac{\#\pi^\pm + \#\pi^0}{\#\pi^\pm}$. The square derives from the fact that the regarded d_{Cut} parameter is quadratic in the energy.

The comparison of the d_{Cut} distributions in $t\bar{t}$ events with the distributions of 6-jet QCD background events (Figure 7.6) shows that the 6-jet background events predominate at small values of the cut-off parameter. At very large values the fully hadronic $t\bar{t}$ events are dominating.

7.2.2 Produced signal and background events

For the analysis of fully hadronic $t\bar{t}$ events and their separation from the QCD multijet background a lot of events had to be simulated and processed. Table 7.1 lists the number of $t\bar{t}$ events which were generated for this analysis (PYTHIA $t\bar{t}$ and ATLFast $t\bar{t}$ events) as well as the number of available $t\bar{t}$ events obtained from Athena full simulation⁵, as described in Chapter 6.3.4.

In this context ‘‘PYTHIA $t\bar{t}$ ’’ denotes that the 4-vectors of the fully hadronic $t\bar{t}$ events have been produced with PYTHIA 6.2 stand-alone outside the Athena environment. These 4-vectors have then been transformed into pool format and further processed with ATLAS software (ATLFast version 11.0.41), analogue for the production of the QCD multijet events (see Section 6.3).

	PYTHIA $t\bar{t}$	ATLFast $t\bar{t}$	Full simulation
# Events	259000	259000	147000
σ [nb]	0.16	0.14	0.14

Table 7.1: Number of available fully hadronic $t\bar{t}$ events. PYTHIA $t\bar{t}$ denotes the 4-vectors which have been produced with PYTHIA 6.2 stand-alone outside the Athena environment and afterwards further processed in Athena. ATLFast $t\bar{t}$ marks the events which have been exclusively produced and further processed within the Athena environment with ATLFast. Full simulation indicates the $t\bar{t}$ events which have been obtained from ATLAS full simulation (Section 6.3.4).

‘‘ATLFast $t\bar{t}$ ’’ indicates that the complete simulation and processing has been carried out within the Athena environment. Thus, the simulation (with PYTHIA version 6.323) and processing of the events was performed by one single ATLFast 11.0.41 run.

Note, that the resulting $t\bar{t}$ cross sections, listed in Table 7.1, are smaller than the expected LHC cross section⁶ for fully hadronic $t\bar{t}$ events [38]. This is due to the limitation of the phase space for the generation of the $t\bar{t}$ events in PYTHIA (see Section 6.2.1 and Appendix A). This cut reduces the fully hadronic $t\bar{t}$ cross section by a factor of about two [13], while the underlying physics remains unchanged. Thus, the shape of the distributions is the same with and without a limitation of the phase space, as

⁵As fully simulated fully hadronic $t\bar{t}$ events, the two csc11 samples ‘‘csc11.005204.TTbar_FullHad_McAtNlo_Jimmy.recon.AOD.v11004107’’ and ‘‘csc11.005204.TTbar_FullHad_McAtNlo_Jimmy.recon.AOD.v11004205’’ have been used for this thesis. They were the only available fully simulated hadronic $t\bar{t}$ samples at this time.

⁶There is also a difference in the cross section for PYTHIA $t\bar{t}$ and ATLFast $t\bar{t}$ events due to the different versions of PYTHIA used for the generation of the events.

shown in Appendix A. In addition, PYTHIA provides only LO calculations⁷ for the generated events [13], while the expected LHC cross section of 0.37 nb is a NLO prediction [38].

Table 7.2 summarizes the number of generated QCD events and b -quark events reconstructed both from calorimeter cell entries and from charged particle tracks. The b -quark samples must be merged with the QCD samples for 4, 5 and 6++ final state partons in order to get "realistic" QCD multijet event samples.

ALPGEN + k_T	6++	5	4	3	$b(6++)$	$b(5)$	$b(4)$
# Events	500000	431000	210000	224000	79000	77000	35000
σ [nb]	26	48	480	4766	4	16	69

Table 7.2: Number of generated QCD multijet events and b -quark events produced with the QCD background 4-vectors from ALPGEN and PYTHIA 6.2. For the jet reconstruction calorimeter cells and tracks were used. The b -quark cross sections are derived from the cross sections quoted in [47].

There are also smaller sets of QCD multijet events which have been reconstructed with a standard Cone algorithm with Cone size of $R = 0.4$, as listed in Table 7.3. Note, that in contrast to the k_T algorithm the Cone algorithm was used in standard setting and was not optimized for the reconstruction of QCD multijet events.

ALPGEN + Cone	6++	5	4	3	$b(6++)$	$b(5)$
# Events	181000	237000	121000	150000	24000	22000

Table 7.3: Number of QCD events for the different numbers of final state partons and number of generated b -quark events. For the jet reconstruction a standard Cone algorithm ($R = 0.4$) was used. Using the Cone algorithm the reconstruction was exclusively done from calorimeter cell entries. Further information concerning these events can be found in Appendix B.

7.2.3 General properties of signal and background events

This section treats the properties of $t\bar{t}$ multijet and QCD multijet background events before any cuts have been applied to separate the $t\bar{t}$ signal from the background. All quantities have been studied for both events reconstructed from calorimeter cell entries and charged particle tracks. While for the calorimeter cell events a precise energy calibration of the calorimeter is necessary in order to obtain accurate measurements, the events reconstructed from charged particle tracks deliver precise measurements of the particles' momenta already at the beginning of the LHC. However, the charged particle track events do not contain neutral particles but can deliver only measurements of the charged particles in the events.

⁷For further information see Section 6.2.1.

Figure 7.7 shows the distributions for the azimuthal angle ϕ of the jets in $t\bar{t}$ and background events for a jet reconstruction from calorimeter cell entries. The distributions are flat as expected. There is also no difference in the ϕ distributions for the signal and the background events. The corresponding distributions for charged particle tracks, which are not shown explicitly, agree in all details with the plots represented for the cells.

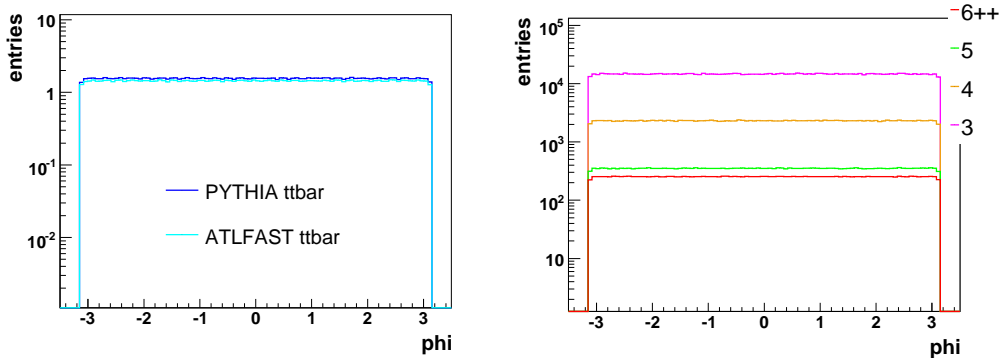


Figure 7.7: ϕ distributions of the jets in $t\bar{t}$ (left) and QCD multijet background events (right) for events reconstructed from calorimeter cell entries.

The η distributions of the jets in events reconstructed from calorimeter cells show that for the background events (Figure 7.8 right) the distribution declines abruptly at η values of about $|\eta| = 2.5$. This is due to an internal η -cut in ALPGEN (see Section 6.1.2), applied when generating the 4-vectors of the background events. Additional η contributions for $|\eta| > 2.5$ are caused by the jet-parton matching in PYTHIA 6.2 and the further processing of the events in ATLFAST.

The $t\bar{t}$ distribution, however, is smooth up to $|\eta| < 5$ corresponding to an internal η cut in ATLFAST [75] at $|\eta_{jet}| = 5$.

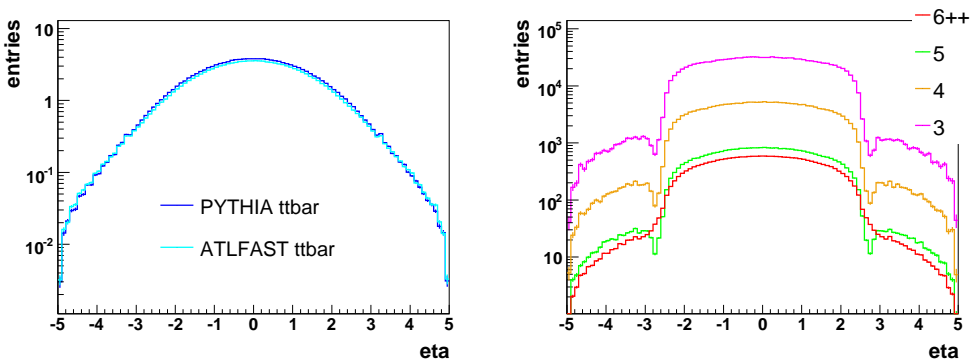


Figure 7.8: η distribution of the jets in $t\bar{t}$ (left) and QCD multijet background events (right) for a jet reconstruction from calorimeter cell entries.

For the events reconstructed from charged particle tracks (Figure 7.9) the distributions drop to zero at $|\eta| = 2.5$ for both the signal and the background events. This meets the expectations for the track-reconstruction as particle tracking in ATLAS is possible only up to $|\eta| \leq 2.5$ [32].

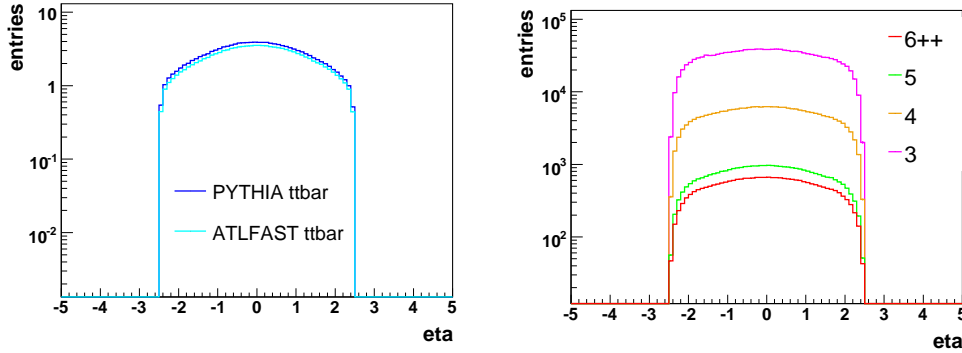


Figure 7.9: η distribution of the jets in $t\bar{t}$ (left) and QCD multijet background events (right) for a jet reconstruction from particle tracks.

The jet- p_T distributions (Figures 7.10 and 7.11) are very similar for the events reconstructed from cells and tracks indicating many jets with small transverse momenta. However, the track events seem to tend slightly to softer jets, thus, jets with smaller p_T . This might be caused by the shift of calorimeter cell entries to the cell-centre, causing additional p_T contributions for the particles, and also by the slightly different values for the cut-off parameter d_{Cut} chosen for the jet reconstruction, respectively. The kinematic distributions of ATLFAST track events have been multiplied with a factor of $\frac{3}{2}$ for comparability with distributions using calorimeter cells only. For the charged particle tracks and the calorimeter cells the background events – especially the 3-jet background – show fluctuations at large jet- p_T which is due to lacking statistics.

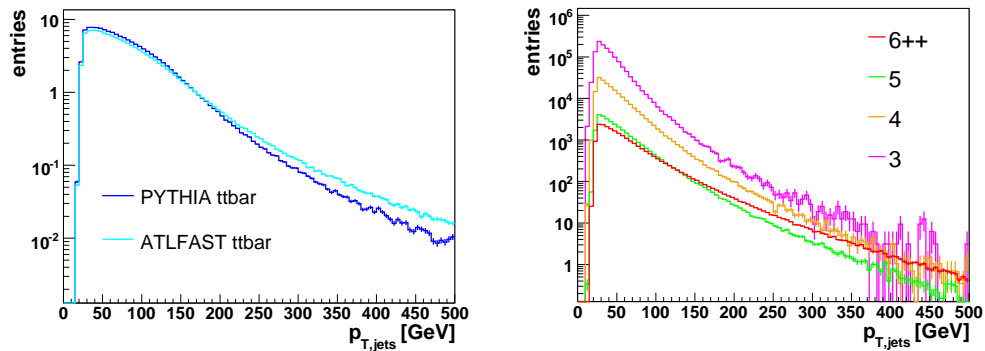


Figure 7.10: Transverse momenta p_T of the jets in $t\bar{t}$ (left) and QCD multijet background events (right) for the jet reconstruction from calorimeter cell entries.

The p_T -distributions for the PYTHIA $t\bar{t}$ and the ATLFast $t\bar{t}$ events are almost identical at small transverse momenta (Figures 7.10 and 7.11 left). But there is a deviation for values of $p_{T,jet} > 300$ GeV which is more distinct for the calorimeter cell events. This difference between the two fully hadronic $t\bar{t}$ samples might be caused by the two versions of PYTHIA (PYTHIA 6.2 stand-alone and PYTHIA 6.323 [76] which is implemented in Athena Version 11.0.41) used for the simulation of the events, comprising differences in the parton shower generation [77].

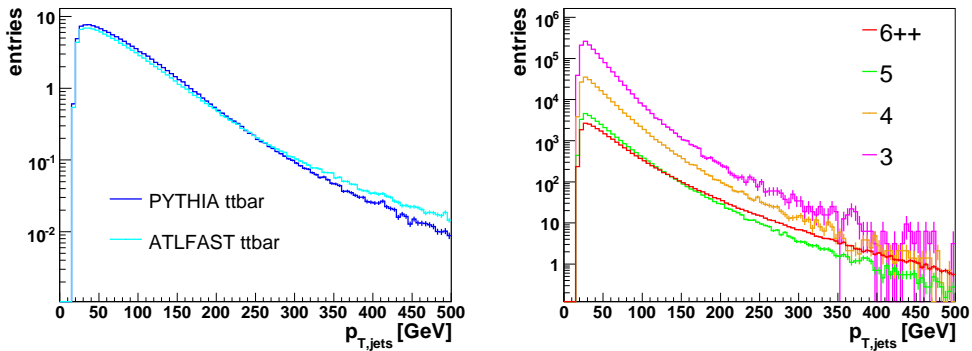


Figure 7.11: Transverse momenta p_T of the jets in $t\bar{t}$ (left) and QCD multijet background events (right) for the jet reconstruction from tracks. The $p_{T,jets}$ values have been multiplied with a factor of $\frac{3}{2}$ in order to include approximately also the contributions from non-charged particles.

The number of reconstructed jets for calorimeter cell events is illustrated in Figure 7.12. The $t\bar{t}$ events have six reconstructed jets in mean. The number of jets in 6-jet background events is clearly shifted to larger values, which is caused by the inclusive 6-jet samples comprising six or more final state partons. The 3-jet and 4-jet background events show only small jet multiplicities.

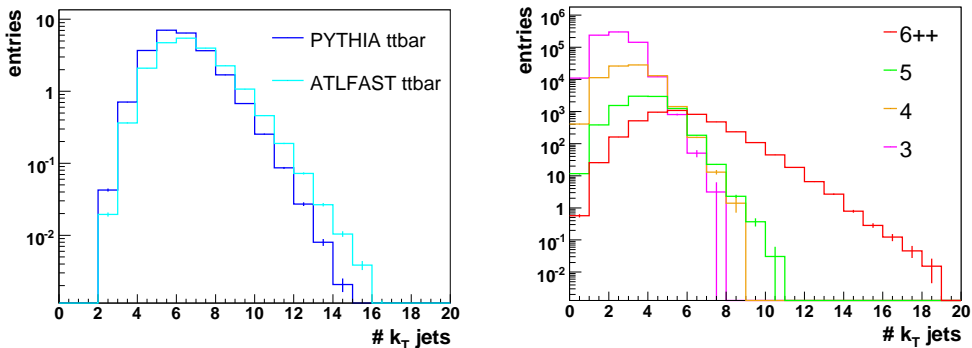


Figure 7.12: Number of reconstructed jets in $t\bar{t}$ (left) and QCD multijet background events (right) for the jet reconstruction from cells.

The events reconstructed from calorimeter cell entries slightly tend to larger jet multiplicities in maximum than the track events (Figure 7.13). This might be again a feature of the slightly different cut-off parameters for the two kinds of jet reconstruction (tracks and cells).

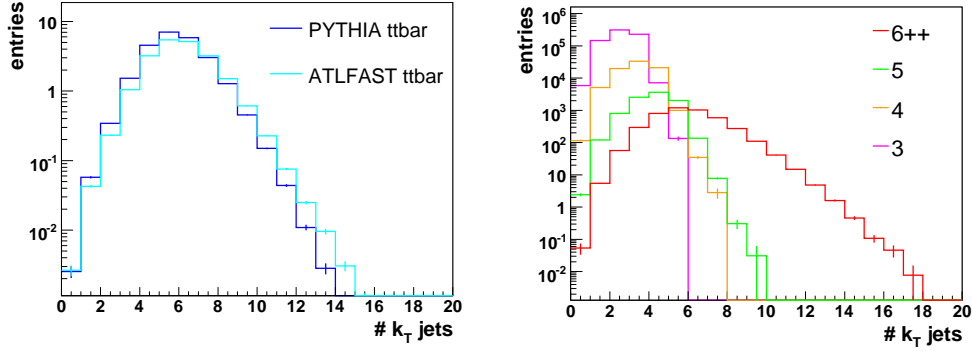


Figure 7.13: Number of reconstructed jets in $t\bar{t}$ (left) and QCD multijet background events (right) for the jet reconstruction from tracks.

Figure 7.14 shows a distribution for η_{jet} versus the number of reconstructed jets in $t\bar{t}$ multijet events which were reconstructed from cell entries. Most jets are located at small η values ($|\eta| < 2$). Only a very small fraction of jets can be observed in the forward section of the calorimeter for $|\eta| > 3$, which is a calorimeter region where jets cannot be reconstructed properly any more by the ATLAS detector [32]. Although it is again noticeable that ATLFAS $t\bar{t}$ events (Figure 7.14 right) slightly tend to higher jet multiplicities, the two plots for the PYTHIA $t\bar{t}$ and ATLFAS $t\bar{t}$ events agree well.

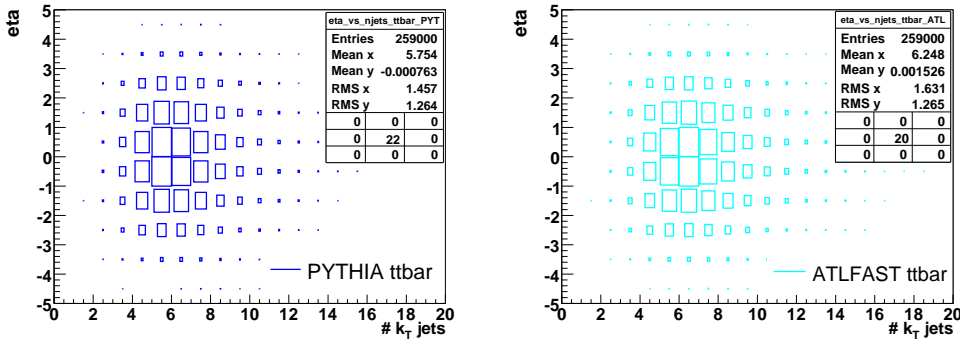


Figure 7.14: η versus the number of reconstructed jets for events reconstructed from cell entries. Left: PYTHIA $t\bar{t}$ events. Right: ATLFAS $t\bar{t}$ events.

The corresponding distributions for the background events (reconstructed from cells) are presented in Figure 7.15. Again most of the jets are concentrated on the central region of the detector ($|\eta| < 2$), although the background events show a larger fraction of jets for $|\eta| > 2$ than the $t\bar{t}$ events. This is due to the fact that jets in the QCD events

originate predominantly from the radiation of softer gluons, whereas most of the jets in the $t\bar{t}$ events are caused by the hadronization of highly energetic quarks comprising larger angles θ to the beam pipe which leads to smaller η values.

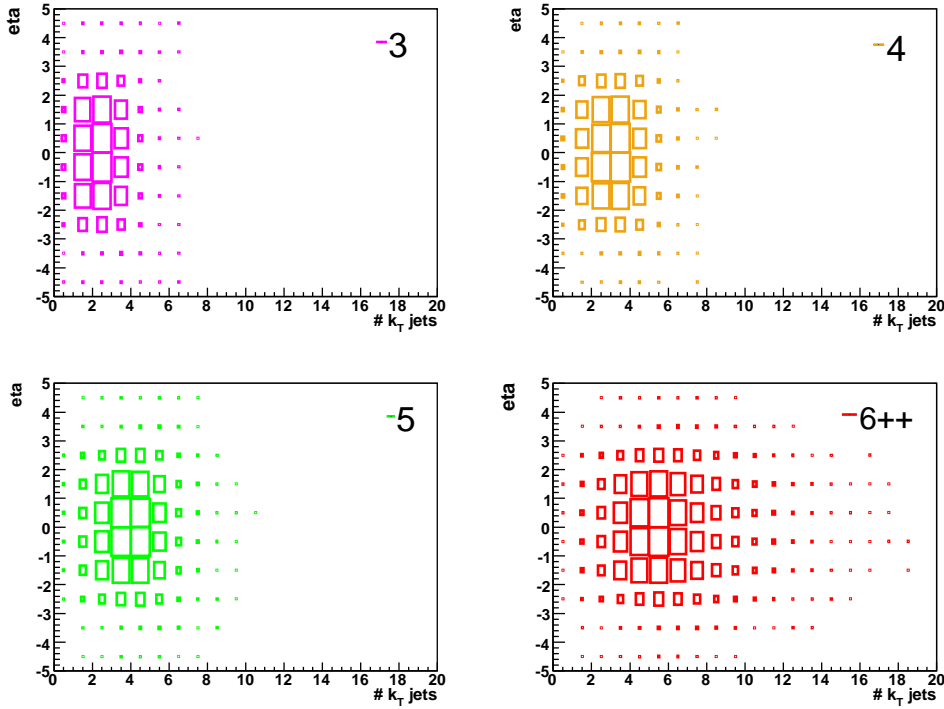


Figure 7.15: η versus the number of reconstructed jets for QCD multijet background events reconstructed from cell entries.

The same behaviour is observed for the events resulting from the jet reconstruction from charged particle tracks. However, due to the ATLAS particle tracking, which can be carried out only up to $|\eta| \leq 2.5$, there are no entries for larger η -values, as already shown in Figure 7.9.

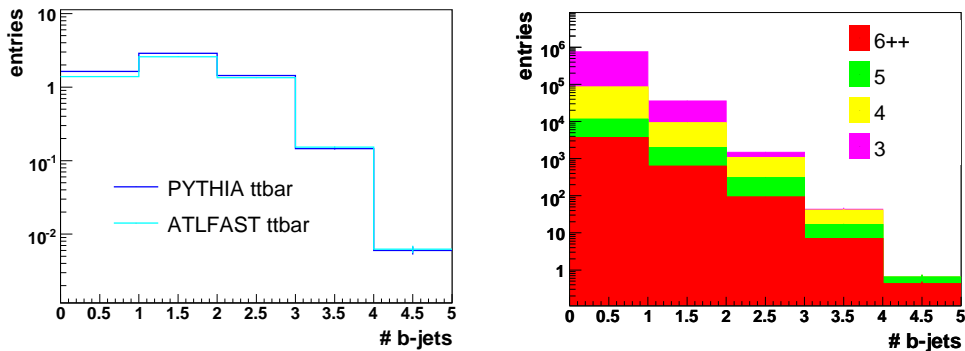


Figure 7.16: Number of b -tagged jets in $t\bar{t}$ (left) and QCD background (right) events for a jet reconstruction from cells. The distributions for the QCD events are added in so-called stacked histograms [78]. A first cut on the pseudorapidity η of the b -jets was applied ($|\eta_{b\text{-jet}}| < 2.5$).

The number of b -tagged jets is shown in Figure 7.16. For these distributions an η -cut of $|\eta_{b-jet}| < 2.5$ has been applied as jets originating from b -quarks can only be detected for $|\eta| \leq 2.5$ [32]. The $t\bar{t}$ events (Figure 7.16 left) comprise in most cases one or two b -jets as was expected regarding the decay of top and antitop into two W bosons and two b -quarks. The QCD background events, however, exhibit a generally smaller number of b -tagged jets.

The number of b -tagged jets in $t\bar{t}$ events reconstructed from charged particle tracks is very similar to that for calorimeter cell events. The background events show no 3-jet QCD events with four b -tagged jets. There are some 3-jet background events with five reconstructed b -jets indicating false tags.

In Figure 7.17 the η_{b-jet} versus the number of b -jets distribution in $t\bar{t}$ multijet events⁸ is illustrated, still without a cut on the pseudorapidity of the b -jets. There are no entries for $\eta_{b-jet} > 2.5$ because there is no acceptance by the silicon and pixel detectors for $\eta_{b-jet} > 2.5$ [32]. Most jets are located at small η values ($|\eta| < 2$). One can see that in most cases the $t\bar{t}$ events comprise two b -jets.

The corresponding plot for the QCD multijet background events is presented in Figure 7.18. It is clearly visible that the number of b -tagged jets is shifted to smaller values than for the $t\bar{t}$ events.

The distributions for the events reconstructed from charged particle tracks are not shown in this thesis because they exhibit almost no difference compared to the distributions of the cell-entry events.

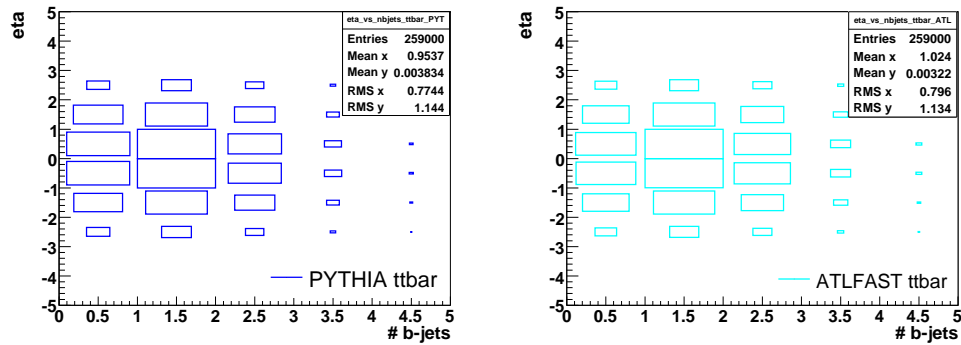


Figure 7.17: η versus the number of b -tagged jets for $t\bar{t}$ events reconstructed from calorimeter cells. Left: PYTHIA $t\bar{t}$ events. Right: ATLFAST $t\bar{t}$ events.

The number of particles (hadrons) in $t\bar{t}$ and background events is shown in Figure 7.19. As the properties of particles are independent from jet reconstruction, there is only one distribution for both events reconstructed from tracks and cells.

ATLFAST $t\bar{t}$ events contain obviously more particles than PYTHIA $t\bar{t}$ events (Figure 7.19 left). This might be again due to the two different versions (thus different implementations of the parton shower) of the PYTHIA Monte Carlo generator used for simulating the $t\bar{t}$ events [77].

⁸This plot shows the distribution for events reconstructed from calorimeter cell entries.

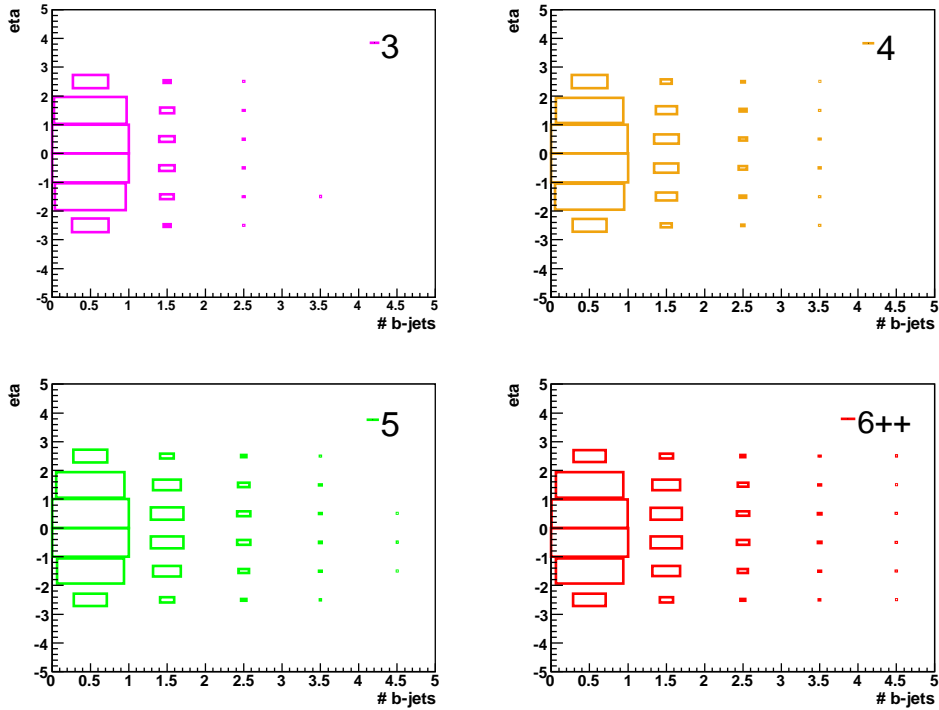


Figure 7.18: η versus the number of b -tagged jets for QCD multijet background events reconstructed from calorimeter cell entries.

The QCD 6-jet events show – similar to the $t\bar{t}$ events – a large number of up to 500 or more hadrons in the events, whereas the other background events are shifted to smaller numbers of particles.

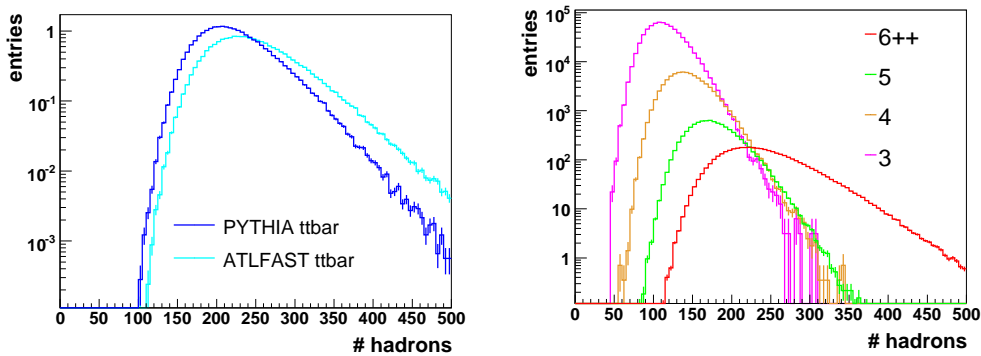


Figure 7.19: Number of particles (hadrons) in $t\bar{t}$ and background events.

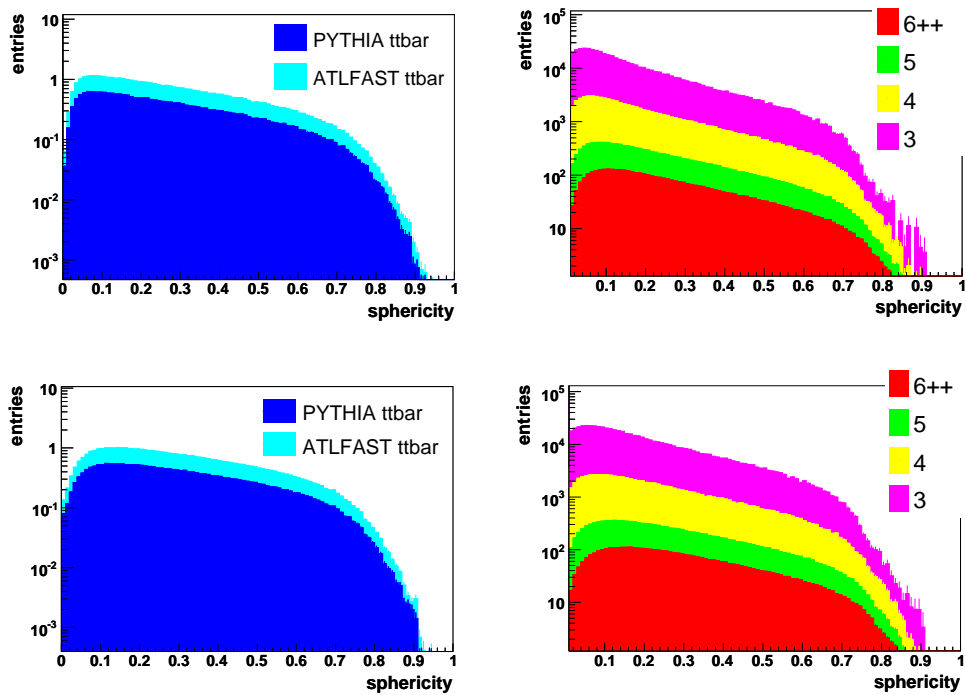


Figure 7.20: Sphericity in events reconstructed from calorimeter cell entries (top) and charged particle tracks (bottom), illustrated with stacked histograms.

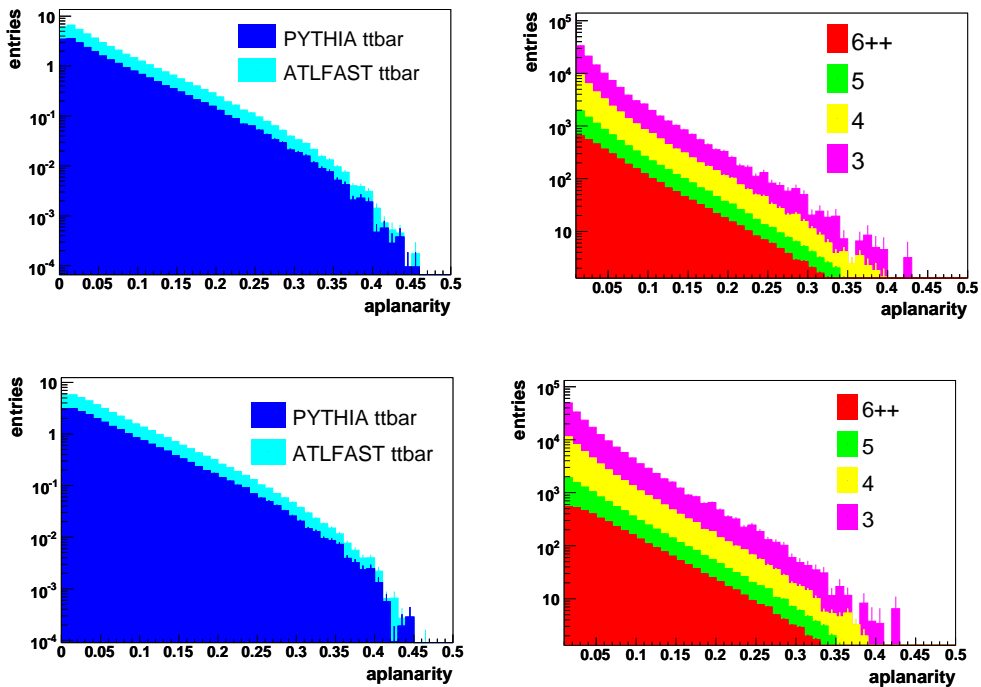


Figure 7.21: Aplanarity in events reconstructed from calorimeter cells (top) and charged particle tracks (bottom), illustrated with stacked histograms.

The topology variable sphericity [74] is presented in Figure 7.20. In this analysis the event shapes have been determined from the 3-vector momenta of the reconstructed jets. The distributions of the cell events (Figure 7.20 top) are very similar to the sphericity calculated in particle track events (Figure 7.20 bottom). All in all the histograms show a slight tendency for the $t\bar{t}$ events to be more spherical than the QCD background events which is expected due to the large top quark mass.

The same behaviour can be observed in the aplanarity distributions for calorimeter cell events (Figure 7.21 top) and charged particle track events (Figure 7.21 bottom).

7.2.4 Comparison of fully hadronic $t\bar{t}$ events from full simulation and fast simulation

Fully simulated hadronic $t\bar{t}$ events (see Section 6.3.4) comprise pre-defined jet reconstruction settings which are hardly accessible and which cannot be reconfigured easily, retrospectively. Different settings for the jet reconstruction, as described in Section 6.4, make it difficult to compare the fully simulated $t\bar{t}$ events with the events from private production.

This section sketches the differences between the fully simulated hadronic $t\bar{t}$ events used for this analysis⁹ and the ATLFAS $t\bar{t}$ events simulated and processed with ATLFAS 11.0.41 in the Athena environment.

In this context Figure 7.22 illustrates the ϕ distribution for fully simulated and fast simulated events. The ATLFAS $t\bar{t}$ sample, presented in this plot, was reconstructed from calorimeter cell entries. In Athena full simulation the calorimeter cell entries are generally used for the reconstruction of the events. Thus, this section shows no plots for the ATLFAS $t\bar{t}$ events reconstructed from charged particle tracks, as they cannot be compared with the full simulation.

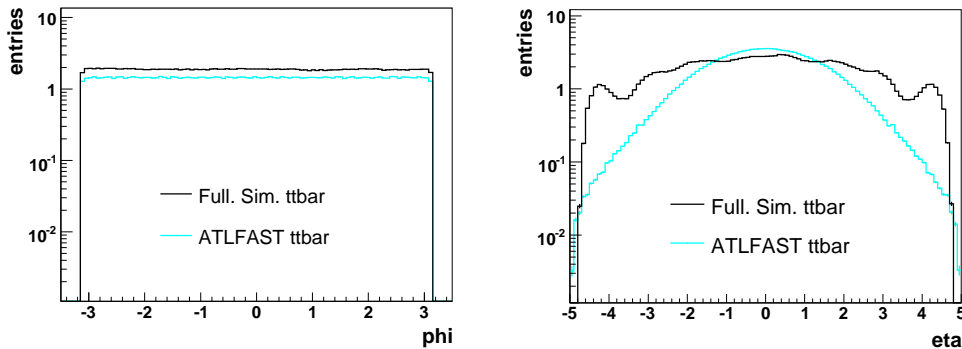


Figure 7.22: ϕ (left) and η (right) distribution of the jets in $t\bar{t}$ events from full simulation and fast simulation with ATLFAS 11.0.41. The jet reconstruction in the shown fast simulated events was done with calorimeter cells. Fully simulated events are always reconstructed from cell entries.

The ϕ distribution in Figure 7.22 left is not really different for the fast and the full simulation exhibiting flat distributions up to $|\phi| = \pi$.

⁹The fully simulated $t\bar{t}$ events used in this analysis have been generated with MC@NLO [79].

The η distribution in Figure 7.22 right, however, shows a bad agreement with the ATLFast events reconstructed from cells comprising η values of up to $\eta = \pm 5$. The fully simulated events peak at large η values ($|\eta| \approx 4.5$) which might be due to the proton remnants most probably recombined to jets in the fully simulated events. The distribution for the fully simulated events is not smooth as for the ATLFast events and it is broader, which could be caused by the smearing of the events in the full simulation.

Figure 7.23 left illustrates the transverse momenta of the jets in the events showing a good agreement of the fully simulated events with the ATLFast cell-entry events for large transverse momenta. However, the fully simulated events comprise a much larger fraction of soft jets, presumably caused by the proton remnants contained in the fully simulated events leading to jets with very small transverse momenta with respect to the beam axis. The fast simulated events do not contain the proton beam remnants due to the use of the k_T algorithm in exclusive mode in the fast simulation separating the hard final state from the beam remnants (Section 5.2.3).

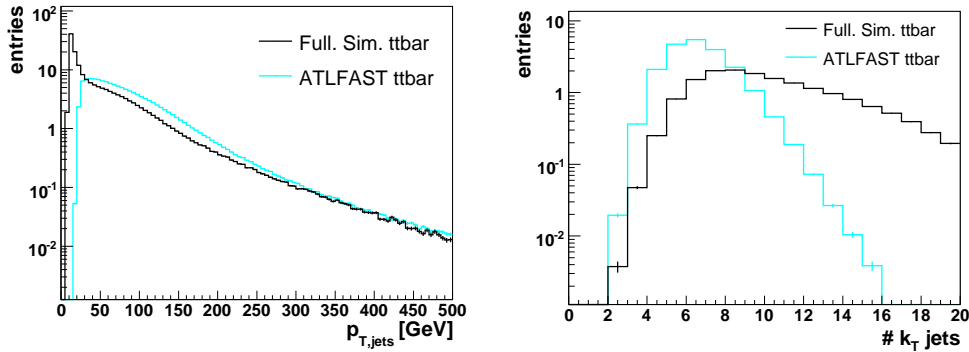


Figure 7.23: Left: Transverse momenta p_T of the jets in $t\bar{t}$ events from full simulation and fast simulation with ATLFast 11.0.41. Right: Number of jets in $t\bar{t}$ events from full simulation and fast simulation. The fast simulated events have 6.2 jets in mean. The fully simulated events, however, comprise in mean 9.9 jets.

The number of reconstructed jets is presented in Figure 7.23 right. Due to the different settings for the k_T algorithm in full and fast simulation (Section 6.4) the ATLFast events do not agree at all with the fully simulated events. While the self-generated events have in mean six final jets¹⁰, the distribution for fully simulated events shows a much larger jet multiplicity which is again due to the fact that in the fully simulated events the proton beam remnants are most probably allocated to jets. This results in the larger number of jets and also in softer jets, as already shown in Figure 7.23 left.

Figure 7.24 left shows the η versus N_{jet} distribution for ATLFast $t\bar{t}$ events, the fully simulated events are represented in Figure 7.24 right.

The full simulation comprises much more jets, as described above. A larger number of jets are found in the forward section of the calorimeter ($|\eta| > 2$) than in the ATLFast events. This conforms to the assumption that the soft beam remnants have

¹⁰The exact mean for the ATLFast $t\bar{t}$ distribution amounts to 6.2 while the fully simulated events comprise in mean 9.9 reconstructed jets.

been allocated to the jets. Also in the central region of the detector, at very small η values, more jets are reconstructed in the fully simulated events than in the fast simulation with ATLFAST.

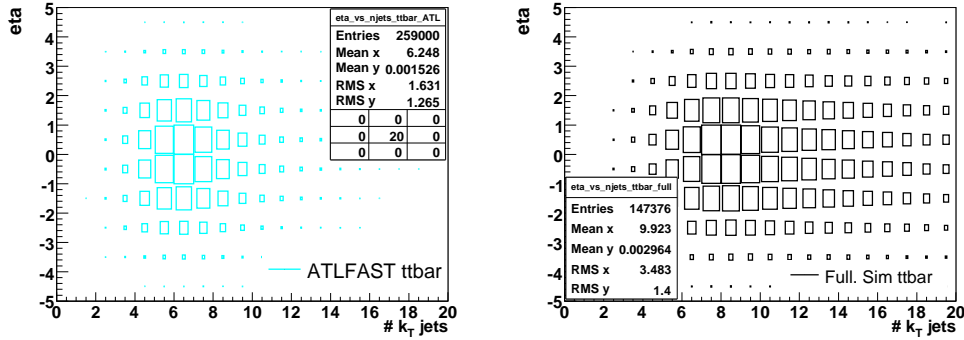


Figure 7.24: η versus the number of reconstructed jets in fast simulated $t\bar{t}$ events (left) and fully simulated $t\bar{t}$ events (right).

The number of b -tagged jets is much larger in fully simulated events than in events from fast simulation, as illustrated in Figure 7.25. Due to the k_T algorithm used in inclusive mode and the resulting larger number of final state jets in fully simulated events, the number of reconstructed b -jets seems to increase as well. This might be an indication that the inclusive mode of the k_T algorithm does not really meet the demands for reconstructing fully hadronic $t\bar{t}$ events.

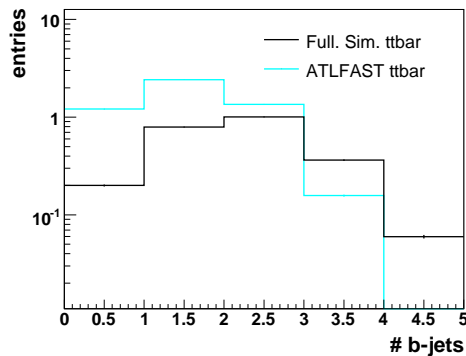


Figure 7.25: Number of b -tagged jets in fully hadronic $t\bar{t}$ events from full simulation and fast simulation with ATLFAST 11.0.41.

The distribution for η_{b-jet} versus N_{b-jet} is shown in Figure 7.26 left for the ATLFAST events and in Figure 7.26 right for the events from full simulation. For the fully simulated events the plot shows again that more b -jets are reconstructed. Nevertheless, the b -jets are all located within $|\eta| \leq 2.5$.

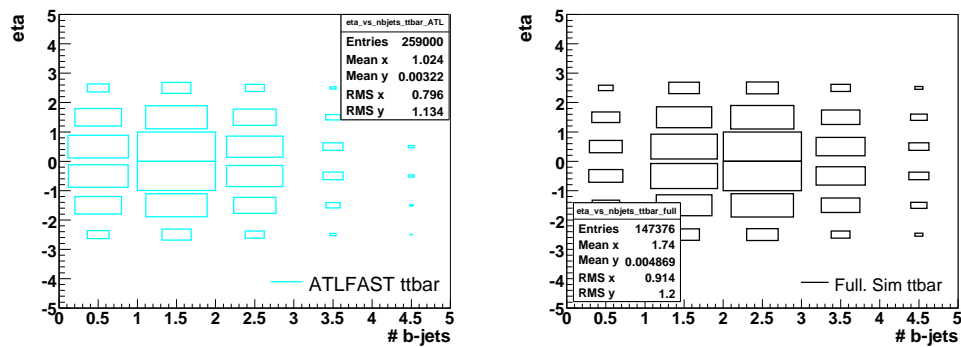


Figure 7.26: η versus the number of b -jets in fast simulated $t\bar{t}$ events (left) and fully simulated $t\bar{t}$ events (right).

The sphericity distributions are shown in Figure 7.27. The fast simulated events show a slight tendency to larger sphericity values than the fully simulated events.

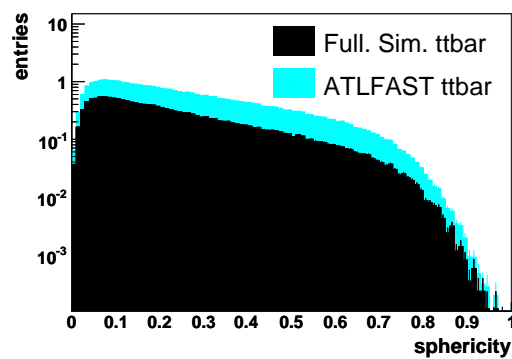


Figure 7.27: Sphericity in fast and fully simulated $t\bar{t}$ events represented with a stacked histogram.

In summary, the represented distributions confirm the assumption that a direct comparison between the fully simulated $t\bar{t}$ sample and the fast simulated $t\bar{t}$ events from the private production is difficult due to the very different settings for the jet reconstruction in the $t\bar{t}$ events. Therefore, the resulting distributions vary partially strongly, especially for the jet multiplicity in the events, but also the η values for the jets differ clearly for the fast and the fully simulated events.

7.3 Analysis of $t\bar{t}$ and background events at generator level with PYTHIA 6.2

The ATLAS software is still under constant development. Therefore, several features of the "real" events or properties of the completed detector have not yet been

implemented in the software while performing this study. This is for example the case for the simulation of pile-up or multiple events (see Section 7.3.2) in ATLFast.

Consequently, when studying the effect of pile-up events on the fully hadronic $t\bar{t}$ and QCD multijet background events, as described in Section 7.3.2, this has to be done on generator level for the $t\bar{t}$ events exclusively processed with PYTHIA 6.2. PYTHIA stand-alone contains the possibility to simulate multiple interactions in addition to the fully hadronic $t\bar{t}$ and QCD multijet events [13].

When real data will be available at the LHC, the min-bias and pile-up events will be measured – with a special trigger configuration – in these real events and will be used afterwards as a correction for the processes of interest. This procedure is necessary as QCD calculations for semihard and soft interactions are not precisely enough calculable to estimate the effect of the multiple events.

7.3.1 Determination of the cut-off parameter d_{Cut}

Before the generator level $t\bar{t}$ events can be analyzed, the best cut-off parameter d_{Cut} for the reconstruction of fully hadronic $t\bar{t}$ events with exactly six final state jets has to be determined for these events, as already done in Section 7.2.1 for the $t\bar{t}$ events processed with ATLAS software.

The d_{Cut} distribution, illustrated in Figure 7.28, shows again the case when seven jets are merged into six jets ($7 \rightarrow 6$) and six jets are merged into five jets ($6 \rightarrow 5$) for fully hadronic $t\bar{t}$ events. As described in Section 7.2.1, at small values of the cut-off parameter events with a larger number of jets prevail. From 400 GeV^2 to 1000 GeV^2 , however, the 6-jet final states dominate. Thus, a d_{Cut} value of 450 GeV^2 (indicated by the black vertical line in Figure 7.28) was chosen to reconstruct as many $t\bar{t}$ 6-jet events on generator level as possible.

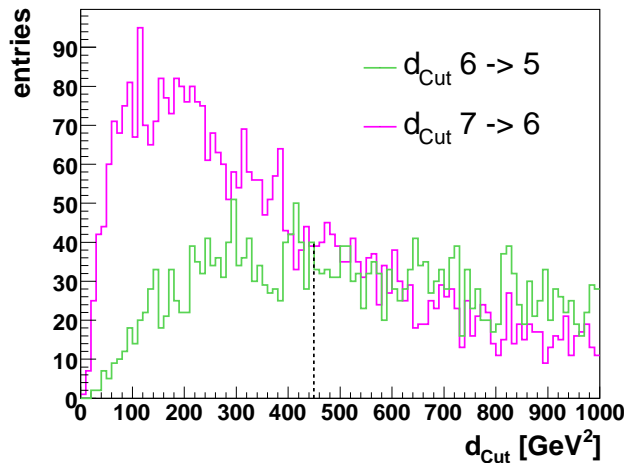


Figure 7.28: Determination of cut-off parameter d_{Cut} for $t\bar{t}$ events on generator level.

This d_{Cut} value corresponds exactly to the chosen cut-off parameter of $(\frac{3}{2})^2 \cdot 200 \text{ GeV}^2$

for the jet reconstruction from charged particle tracks¹¹ (see Section 7.2.1). The cut-off parameter of 550 GeV^2 for the jet reconstruction from calorimeter cell entries in ATLFast is in good agreement with this value when the imprecise reconstruction of the calorimeter cell entries caused by the finite cell size and the additional p_T contribution for each particle due to the shift of each entry to the cell-centre are considered. When the optimal cut-off parameter for the jet reconstruction of fully hadronic $t\bar{t}$ events on generator level is found, the effect of pile-up can be examined. This is described in the following section.

7.3.2 Pile-up studies

In a single crossing of proton-bunches several parton interactions, so-called *pile-up* events, can occur. This is especially the case at hadron colliders with very high luminosity, as at the LHC. These events cannot easily be separated from each other by the detector, thus biasing the interesting events [2]. The pile-up events include soft (thus low- p_T) interactions between the partons (*min-bias* events) and *semihard* interactions of the partons creating "minijets" at small transverse momenta [80].

For estimating the effect of those pile-up events¹² PYTHIA 6.2 was configured to include the generation of several pp events per bunch-crossing as well as to produce semihard QCD and all kind of diffractive and low p_T events in addition to the $t\bar{t}$ and QCD multijet background events.

For these purposes the instantaneous luminosity of $L = 10^{34} \text{ cm}^{-2}\text{s}^{-1}$ for the LHC [32, 81] and the expected bunch spacing of $\Delta\tau = 25 \text{ ns}$ [32, 81] were used to calculate the luminosity per bunch-crossing L_{BC} , needed by PYTHIA 6.2 as input for the pile-up simulation [13]:

$$L_{BC} = \Delta\tau \cdot L = 0.25 \cdot 10^{31} \text{ m}^{-2}$$

Using the relation of $1 \text{ mb} = 10^{-31} \text{ m}^2$ the luminosity per bunch-crossing amounts to:

$$L_{BC} = (4.0 \text{ mb})^{-1}$$

With this input the program is able to generate multiple events in addition to the $t\bar{t}$ or background events, thus covering the whole amount of particle production the ATLAS detector might be confronted with [13]. The user can decide if these events include diffractive and elastic events or not. For this study the default setting including diffractive and elastic events in the pile-up events was kept.

The average number of pile-up events for one bunch-crossing is calculated via the relation

$$\bar{n} = \int \mathcal{L} dt \cdot \sigma_{pile-up},$$

where $\sigma_{pile-up}$ is the cross section for the studied pile-up processes [13].

Figure 7.29 shows an estimate of the number of pile-up events per bunch-crossing for a total number of 2000 bunch-crossings. The average number of 25.37 pile-up events corresponds to the number of 23 multiple events expected for the LHC [32].

¹¹When comparing the d_{cut} values the track cut-off parameter of 200 GeV^2 has to be multiplied with $(\frac{3}{2})^2$, considering also the contribution of neutral particles.

¹²For simplification pile-up, soft, diffractive and semihard QCD events are in the following combined in the term *pile-up* or *multiple* events.

This poses a quite large amount of multiple events for the bunch-crossings at the LHC in contrast to the $p\bar{p}$ reactions at the Tevatron with about two multiple events per bunch-crossing [2]. The huge difference in the number of pile-up events is due to the much higher luminosity reached at the LHC.

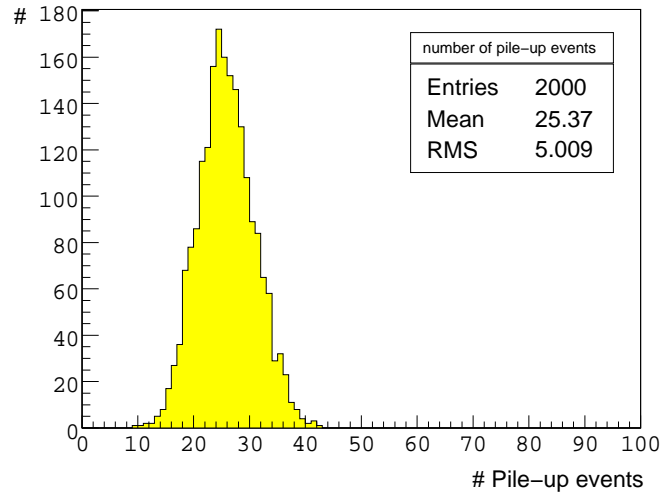


Figure 7.29: Number of multiple events in fully hadronic $t\bar{t}$ events for a luminosity per bunch-crossing of $L_{BC} = 0.25 \text{ mb}^{-1}$.

The effect of the pile-up events on the fully hadronic $t\bar{t}$ and the QCD multijet background events is shown in Figure 7.30 and 7.31. The presence of the multiple events – illustrated by the magenta distributions in Figure 7.30 – leads to an enormous increase in the jet multiplicity for the $t\bar{t}$ and the background events.

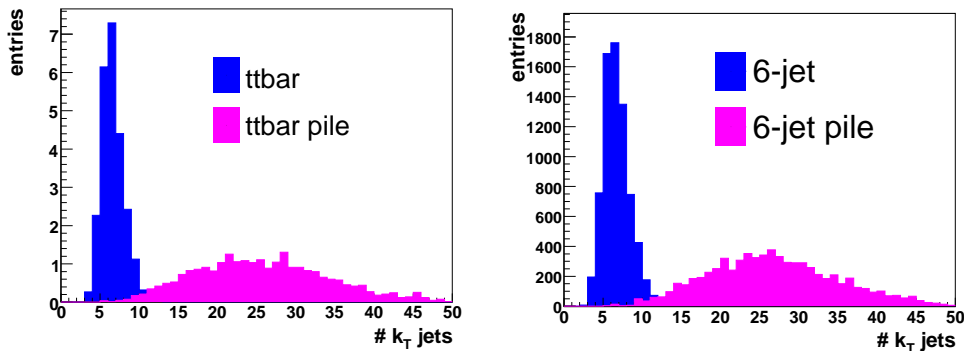


Figure 7.30: Jet multiplicity in $t\bar{t}$ events (left) and jet multiplicity in 6-jet background events (right) with and without pile-up.

The average number of reconstructed jets is shifted to about 25 jets per event, up to 50 jets are found in a single event (Figure 7.30). For comparison, without pile-up events

the jet multiplicity in the $t\bar{t}$ and 6-jet background events had its average at about six jets, which is represented by the blue distributions in Figure 7.30.

No clear peak is visible any more in the pile-up events and therefore, it becomes very difficult to extract the $t\bar{t}$ signal from the pile-up "noise", which is also obvious from Figure 7.31.

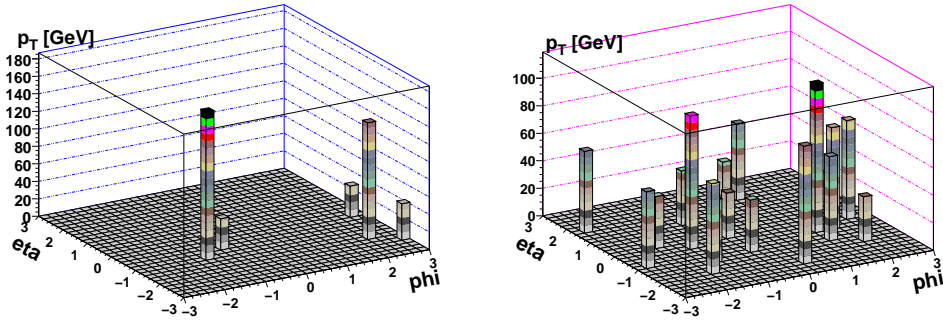


Figure 7.31: Lego plot of one fully hadronic $t\bar{t}$ event without pile-up (left) and with pile-up (right) representing the number of jets in the $\eta_{jets}-\phi_{jets}$ level for $|\eta_{jets}| < 2.5$. The height of the bars corresponds to the transverse momenta of the reconstructed jets. In the presence of pile-up the number of jets increases substantially.

The pile-up events consist predominantly of low energetic particles (see Figure 7.32 left and 7.33 left). This leads to many jets in the forward section of the calorimeter ($|\eta| > 2.5$, Figure 7.32 right and Figure 7.33 right), thus, a region where the detector can deliver only imprecise measurements of the particles.

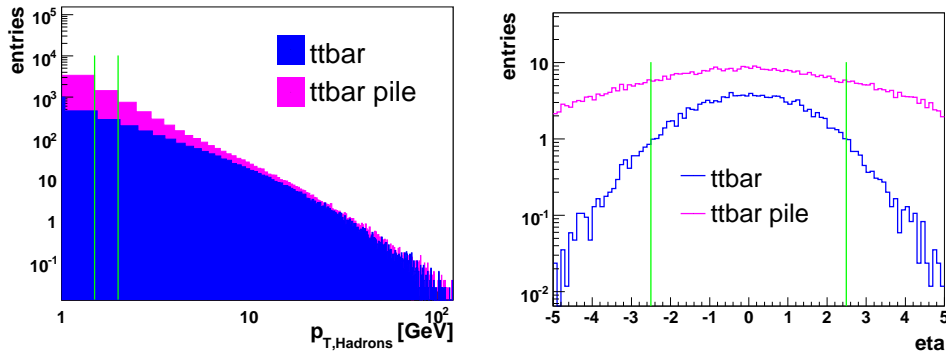


Figure 7.32: Transverse momentum p_T of hadrons (left) and pseudorapidity η of jets (right) for $t\bar{t}$ events with and without pile-up. The green lines illustrate the position of the applied cuts ($p_{T,Hadrons} > 1.5$ GeV (> 2 GeV) and $-2.5 < \eta < 2.5$).

However, particles with very small transverse momenta ($p_T < 0.4$ GeV) do not even reach the calorimeter due to the magnetic field [80] but loop in the inner detector [80]. Accordingly, two cuts on the transverse momentum of the hadrons ($p_{T,Hadrons} >$

1.5 GeV or $p_{T,\text{Hadrons}} > 2$ GeV, respectively) and on the pseudorapidity η of the jets ($-2.5 < \eta < 2.5$) have been applied to the events in order to exclude the particles with too small transverse momenta as well as the jets in regions which cannot be covered by the detector. These cuts are supposed to eliminate measurements biased by the pile-up events without losing too many "good" events.

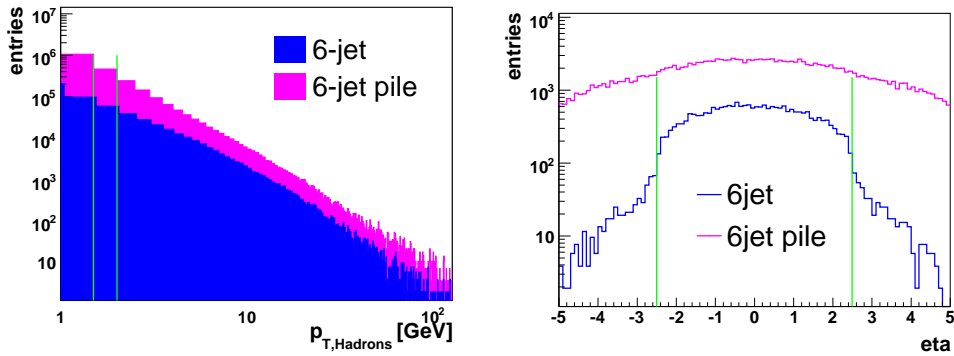


Figure 7.33: Transverse momentum p_T of hadrons (left) and pseudorapidity η of the jets (right) for 6-jet background events. The green lines indicate the position of the introduced cuts ($p_{T,\text{Hadrons}} > 1.5$ GeV (> 2 GeV) and $-2.5 < \eta < 2.5$).

The resulting number of reconstructed jets in fully hadronic $t\bar{t}$ events with and without pile-up after applying the introduced cuts is illustrated in Figure 7.34. On the left there is the distribution of the $t\bar{t}$ events for $|\eta_{\text{jet}}| < 2.5$ and a p_T -cut of $p_{T,\text{Hadrons}} > 1.5$ GeV as well as a cut on the transverse momentum of the jets¹³ at $p_{T,\text{jets}} > 25$ GeV.

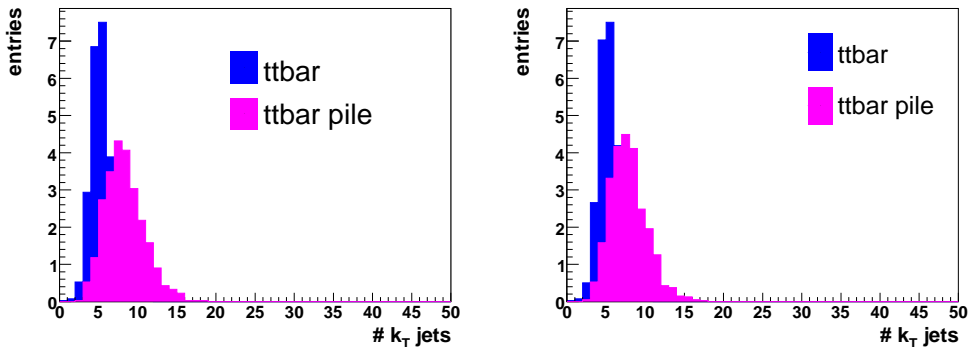


Figure 7.34: Jet multiplicity in fully hadronic $t\bar{t}$ events after the application of the introduced cuts. The blue distributions represent the events without pile-up, the magenta distributions include pile-up events. Cuts on the pseudorapidity ($|\eta_{\text{jet}}| < 2.5$) and on the hadron p_T ($p_{T,\text{Hadrons}} > 1.5$ GeV (left) or $p_{T,\text{Hadrons}} > 2$ GeV (right)) have been applied. For the left distribution an additional cut on the transverse momentum of the jets ($p_{T,\text{jets}} > 25$ GeV) has been used.

¹³This cut is motivated due to the surplus of jets with small transverse momenta in pile-up events, as obvious from Figure 7.35.

As a result of the cuts the number of jets in the pile-up events is now shifted to smaller jet multiplicities, a distinct peak is observable. The positions of the maximum for events with and without pile-up agree quite well.

In Figure 7.34 right the η cut is the same ($|\eta_{\text{jet}}| < 2.5$), the p_T -cut, however, was set to $p_{T,\text{Hadrons}} > 2$ GeV. Apparently, this cut could remove the main part of the pile-up events and therefore, no cut on the transverse momenta of the jets in the $t\bar{t}$ events was needed any more. The resulting distribution looks very similar to the plot shown in Figure 7.34 left.

The two distributions illustrate that it seems to be equivalent to apply either a single cut at $p_{T,\text{Hadrons}} > 2$ GeV or a combination of the cut at $p_{T,\text{Hadrons}} > 1.5$ GeV and the jet- p_T cut at a value of 25 GeV. For both cases¹⁴ the contribution from pile-up on generator level seems to be largely reduced.

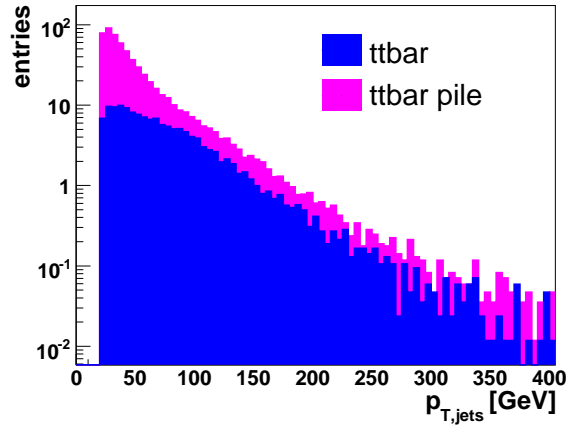


Figure 7.35: Transverse momentum p_T of the jets in $t\bar{t}$ events with and without pile-up. The pile-up events comprise many jets with very small transverse momenta.

The jet multiplicity distributions for the different p_T -cuts (Figure 7.34) make clear that already small changes of the hadrons' p_T seem to have a large effect on the jet multiplicity in the events. Hence, an increase of only 0.5 GeV for the minimum p_T of the hadrons makes further cuts redundant. Consequently, the large number of hadrons at small p_T in the pile-up events changes the distributions dramatically, although the particles might have nearly no physical impact as their transverse momentum is almost too small to be measured and the resulting jets are very often too close to the beam pipe to be resolved.

The chosen cut at 1.5 GeV (2 GeV) for the transverse momentum of the particles is reasonable as the charged particles in the lowest energetic jet (thus, the sixth of six jets) in $t\bar{t}$ events without pile-up have a mean p_T of about 2.5 GeV. Thus, the chosen p_T -cuts do not or do only marginally affect the (charged) particles and therefore, the jet multiplicity in the $t\bar{t}$ events without pile-up, which can also be derived from Figure 7.34. However, this cut affects strongly the pile-up events as there are generally more

¹⁴Both cases include a cut on the pseudorapidity of the jets: $|\eta_{\text{jets}}| < 2.5$.

and also softer particles in the events, which is obvious from Figures 7.32, 7.33 and 7.36.

In summary, one can say that the total number of reconstructed jets in the presence of pile-up is much larger, the distributions are broadened. There are smaller and thus more jets (see Figure 7.31) due to the larger number of generated particles in the events (Figure 7.36).

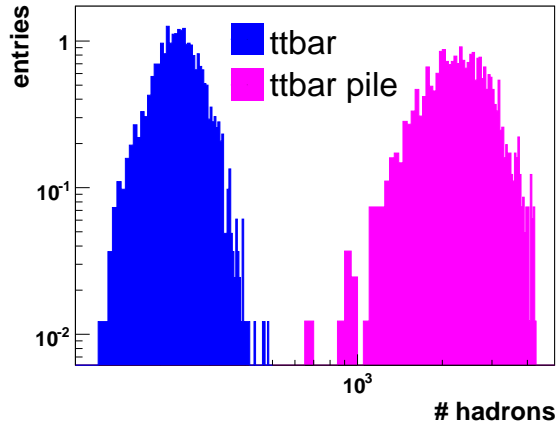


Figure 7.36: Number of hadrons in $t\bar{t}$ events with and without pile-up. In the presence of pile-up events the number of hadrons per event is shifted to larger values. The distributions are cut-off at a number of 4000 particles due to an internal cut in the corresponding PYTHIA common block [13].

However, it might be difficult to apply these results to the events including detector information, especially to the events reconstructed from calorimeter cell entries or to real data, as minimum bias and pile-up are only parameterizations at which the choice of the parameters underlies large uncertainties [82]. In addition, this study regards only events at generator level, the pile-up particles, though, will be additionally influenced by the detector due to its final acceptance in η , p_T , E_T and because of the granularity of the calorimeters.

In order to check the consistency of the pile-up simulation described above, the simulation of multiple events with the settings¹⁵ introduced in [80] was re-run with PYTHIA 6.2 and compared with the pile-up events obtained from the private simulation. The resulting distributions for $t\bar{t}$ multijet events are shown in Figure 7.37. The two distributions for the reconstructed number of jets (Figure 7.37 left) agree, however, the pile-up events generated with the settings of [80] slightly tend to a larger number of reconstructed jets¹⁶. Figure 7.37 right illustrates the transverse momenta of the particles in the fully hadronic $t\bar{t}$ events. The two distributions agree very well.

¹⁵The referred study [80] analyzes $p\bar{p}$ events at the Tevatron and uses still older UA5 parameterizations for min-bias events.

¹⁶For comparison the mean jet multiplicity obtained with own settings is 25.29, with the settings of [80] the mean comes up to 26.89.

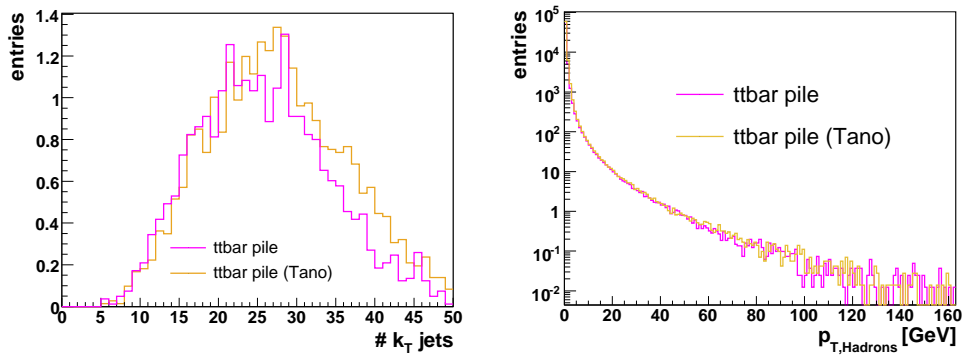


Figure 7.37: Left: Jet multiplicity of $t\bar{t}$ pile-up events obtained from own settings (magenta) and reproduced with the settings introduced in the PhD thesis of Valeria Tano [80] (orange). Right: Transverse momenta of hadrons in fully hadronic $t\bar{t}$ events produced with own settings (magenta) and the settings described in [80] (orange).

Chapter 8

Separation of fully hadronic $t\bar{t}$ events from the QCD multijet background

This chapter describes the separation of the $t\bar{t}$ signals from the QCD multijet background using the information gained from the comparison of the properties of both kinds of events (Chapter 7). Especially QCD background events with six or five final state partons comprise a final state topology which is very similar to that of the $t\bar{t}$ events (as already outlined in Section 7.2.3 and Chapter 4), which makes it difficult to distinguish the signal from the background events.

There are two possible ways for separating the $t\bar{t}$ events from the background, which are discussed in this thesis. On the one hand, one can maximize the signal to background (S/B) ratio which might be approached by a cut analysis with hard cuts discarding not only the background but also lots of signal events, as described in the following section.

On the other hand, there is the possibility to reconstruct a top-mass peak with a preferably large number of signal events. In this case the residual number of background events is larger than it is for the case of the cut analysis with hard cuts. This method aims to detect a small surplus of the $t\bar{t}$ signal on the top of the QCD background events at the value of the top quark mass of about 174 GeV [3] and is described in Section 8.2. In this context the remaining QCD background provides a realistic estimation of the shape and the number of background events after applying the (more or less) loose cuts. The selected $t\bar{t}$ events can be used to determine the $t\bar{t}$ cross section.

8.1 Separation by means of a cut analysis

The separation by means of the following cut analysis aims at a $t\bar{t}$ sample almost free of QCD background events. Consequently, the cuts applied remove not only the background events but reduce strongly also the fully hadronic $t\bar{t}$ signal, which is inevitable when a signal to background ratio close to unity is intended.

The choice of the optimal selection variables is a crucial factor for the success of a cut analysis. These variables must depend on the physical aspects of the signal and background events and consider the technical capabilities of the underlying hardware,

i.e. the ATLAS detector.

The cut variables in this thesis are chosen to accommodate the experimental situation at the very beginning of the LHC and the ATLAS experiment. Thus, this study shall describe the analysis and the separation of fully hadronic $t\bar{t}$ events in the start-up period, when the detector is not yet well understood and quite a few technical components, such as the alignment of the detector or the energy calibration of the calorimeter¹, do not act perfectly yet. The cut analysis is, hence, optimized for the case of a largely uncalibrated detector. As a consequence, some "separation tools" relying on the perfect performance of the detector are ignored or used only at the end and as a supplement to the cut analysis. This applies predominantly to the b -tagging in the events, i.e. the identification of jets originating from b -quarks. As the b -tagging strongly depends on a proper alignment of the detectors, which is not guaranteed in the first year of the LHC, this selection variable can only be an extension to the following analysis.

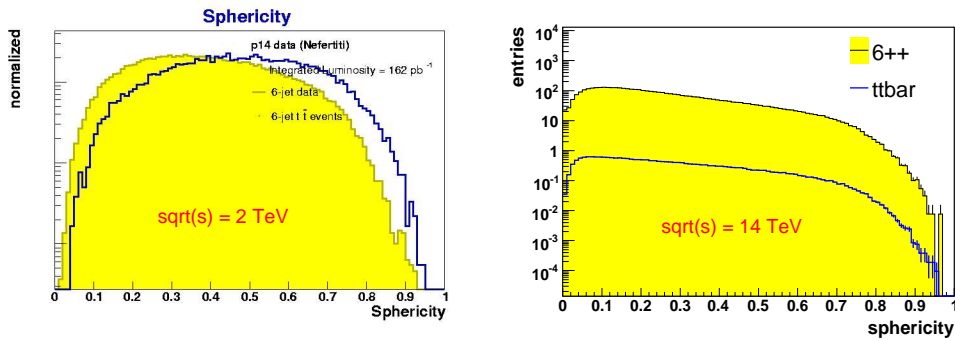


Figure 8.1: Comparison between the sphericity of fully hadronic $t\bar{t}$ and QCD 6-jet events at the Tevatron and at the LHC. Left: Sphericity distribution provided by the $D\phi$ experiment at the Tevatron [83]. Right: Sphericity distribution obtained from the simulated $t\bar{t}$ and 6-jet background events at the LHC.

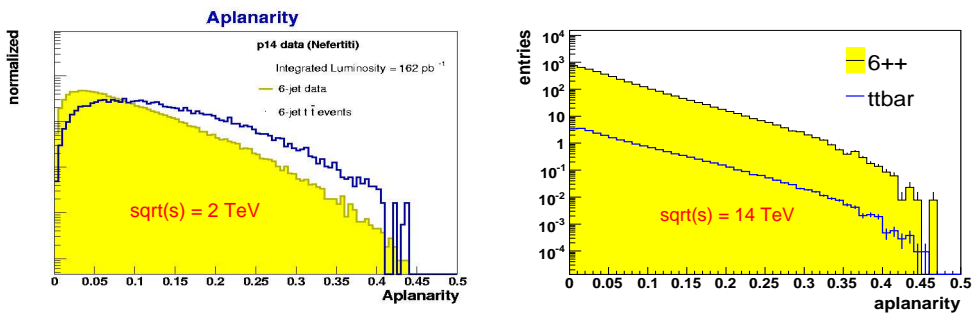


Figure 8.2: Comparison between the aplanarity of fully hadronic $t\bar{t}$ and QCD 6-jet events at the Tevatron and at the LHC. Left: Aplanarity distribution provided by the $D\phi$ experiment at the Tevatron [83]. Right: Aplanarity distribution obtained from the simulated $t\bar{t}$ and 6-jet background events at the LHC.

¹The energy calibration is a very important topic in terms of this thesis as it affects (among others) the energy measurement of the jets occurring in the $t\bar{t}$ and background events.

In addition, event shape variables like sphericity and aplanarity [74], used predominantly at the Tevatron for separating the fully hadronic $t\bar{t}$ signal from the background (see Figures 8.1 and 8.2 left), cannot be the first choice due to the larger energies at the LHC causing the top quarks to be produced with a certain boost. The same applies for the QCD background events. The event shape distributions are broadened for $t\bar{t}$ and background events produced at the LHC, as illustrated in Figures 8.1 and 8.2. Thus, the $t\bar{t}$ distributions get completely similar to the background events and the signal cannot be separated any more, as it was the case for the $t\bar{t}$ studies at the Tevatron. Therefore, a new approach for separating $t\bar{t}$ events from the QCD multijet background events has to be figured out, meeting the conditions and challenges in the start-up period of the LHC with its much larger collision energies than at the Tevatron.

The first variable to cut on is the pseudorapidity η of the jets. According to the technical specification of the ATLAS detector [32] a cut was set at $|\eta_{jet}| < 3$.

The resulting distribution for the number of reconstructed jets in $t\bar{t}$ and background events with the cut on $|\eta_{jet}| < 3$ is shown in Figure 8.3. In comparison to the distributions without η -cut (Figures 7.12 and 7.13) the mean jet multiplicity is shifted to smaller values for events reconstructed from cell entries. The jet multiplicity of the track events has not been changed as particle tracking in ATLAS is only possible up to $|\eta| < 2.5$, anyway [32]. This cut does not really affect the separation of the signal from the background yet, which is also apparent regarding Figures 7.8 and 7.9, which represent the η distributions for the analyzed events.

The plot for the events reconstructed from cells (Figure 8.3 left) includes also the distribution for the fully simulated $t\bar{t}$ events, comprising very large numbers of jets with $|\eta| > 3$ (see Figure 7.24), which could be removed by this first cut.

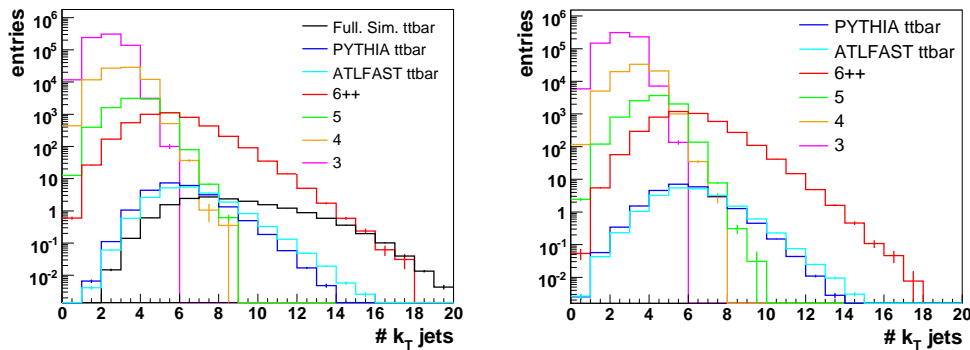


Figure 8.3: Number of reconstructed jets with a first cut on the pseudorapidity η of the jets ($|\eta_{jet}| < 3$). Left: Jets reconstructed from calorimeter cell entries. Right: Jets reconstructed with charged particle tracks.

The number of reconstructed jets in $t\bar{t}$ events is typically located around six. Jets in the 6-jet² background events tend to a larger multiplicity due to the inclusive 6-jet sample comprising six or more final state partons. The 3-jet, 4-jet and 5-jet background events, however, are located at smaller jet multiplicities. As a consequence,

²Note, that for the description of QCD background events the number of final state partons (3, 4, 5, 6++) is referred to as jets, following the ALPGEN notation (see Section 6.1.2).

the next cut confines the number of reconstructed jets in an event to exactly six final state jets (within $|\eta| < 3$): $N_{\text{jet}} = 6$. While the number of $t\bar{t}$ events remains almost stable, the 3-jet background events have been eliminated completely by this cut.

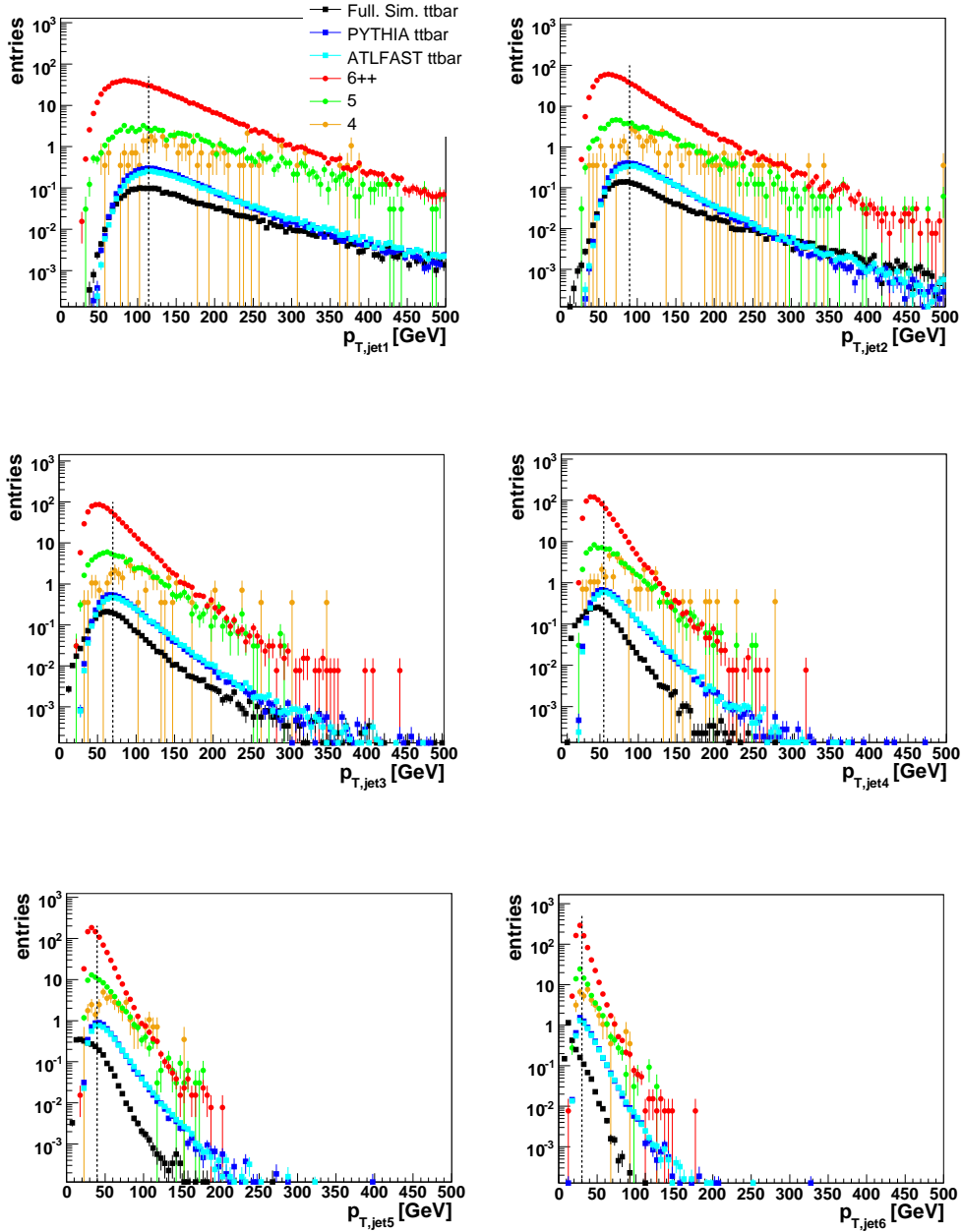


Figure 8.4: Transverse momenta p_T of the six chosen jets in 6-jet events, reconstructed from calorimeter cell entries, in order of decreasing $p_{T, \text{jet}}$. Top left: p_T of leading (highest p_T) jet. Top right: p_T of second jet. Middle left and middle right: p_T of third and fourth jet. Bottom left and bottom right: p_T of the lowest energetic jets five and six. The black vertical line indicates the position of the cut for the jet-momentum, respectively.

The transverse momenta for the six chosen jets in events reconstructed from calorimeter cell entries are represented in Figure 8.4. Obviously, the $t\bar{t}$ events tend to larger jet transverse momenta than the background events.

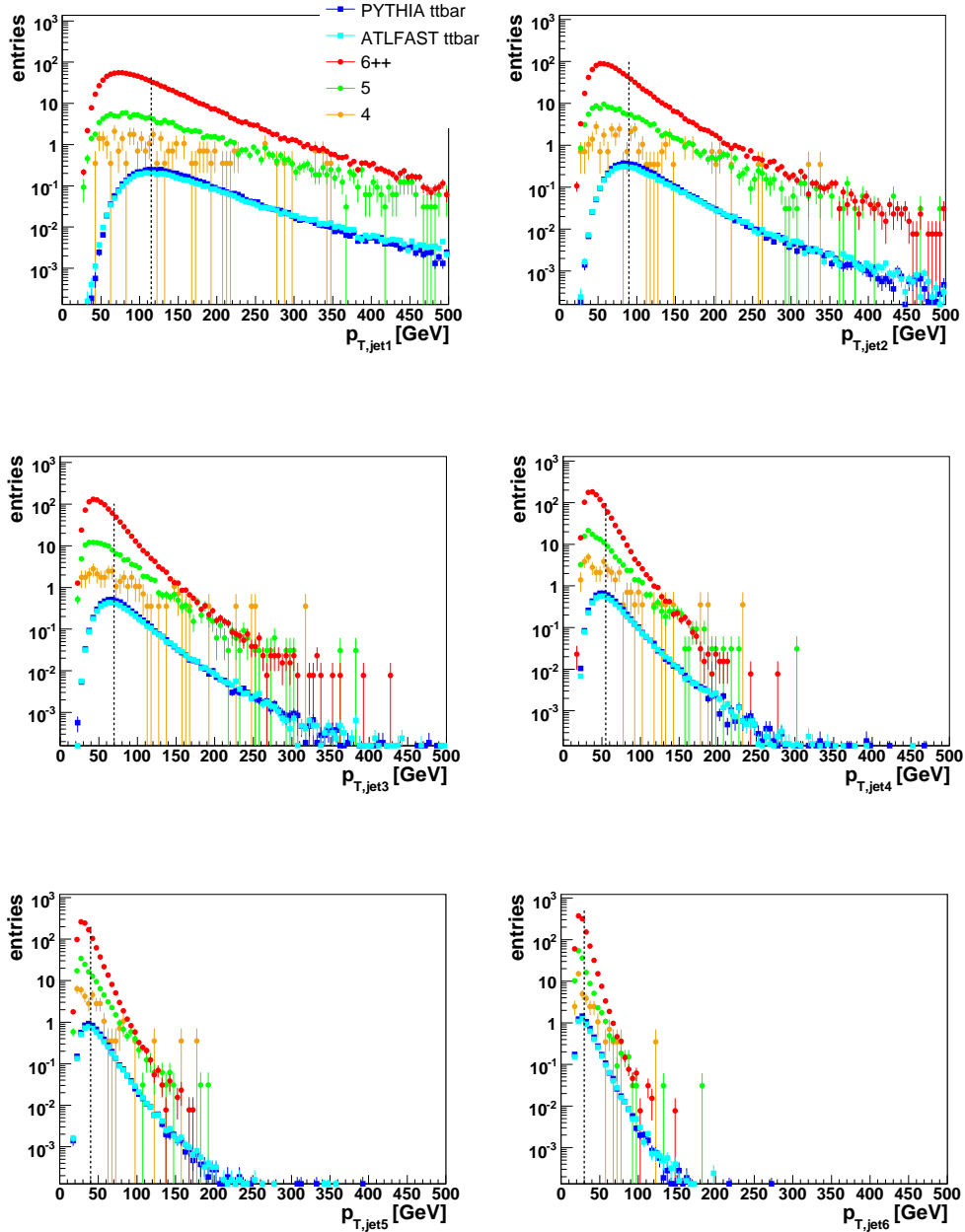


Figure 8.5: Transverse momenta p_T of the six chosen jets in 6-jet events, reconstructed from charged particle tracks, ordered for decreasing $p_{T, \text{jet}}$. The jet momenta have been scaled by 1.5, as explained in the text. Top left: p_T of leading jet. Top right: p_T of second jet. Middle left and middle right: p_T of third and fourth jet. Bottom left and bottom right: p_T of jets five and six. The black vertical line indicates the position of the cut for each jet-momentum.

For eliminating the remaining (predominantly) 5-jet and 6-jet background events a lower limit for each jet's transverse momentum $p_{T,jet}$ was selected, indicated by the black vertical lines in Figure 8.4. Thus, only the fraction of the events on the right of the black lines remains after the p_T -cut. The lower limits for the transverse momenta are listed in Table 8.1.

The corresponding p_T distributions for the events reconstructed from charged particle tracks are illustrated in Figure 8.5. The distributions for track and cell events are in good agreement. However, the charged particle tracks comprise only $\frac{2}{3}$ of the particles in an event, which was compensated by scaling the kinematic variables of the jets for the track events with a factor $\frac{3}{2}$.

Again the same lower limits for the transverse momenta of the six remaining jets (see also Table 8.1) have been applied, which is pointed out once again by the black vertical lines in Figure 8.5.

The p_T -sum of the six chosen jets is shown in Figure 8.6. Again, the $t\bar{t}$ events exhibit larger p_T -values than the background events. This feature is used to apply a cut on the sum of the transverse momenta of the chosen jets at a value of $\sum p_{T,jets} > 140$ GeV, as indicated by the black vertical line in Figure 8.6 left and right. Obviously, this cut especially eliminates the bulk of the 5-jet background events, but also a large amount of 6-jet QCD events is discarded when cutting the p_T -sum of the six chosen jets.

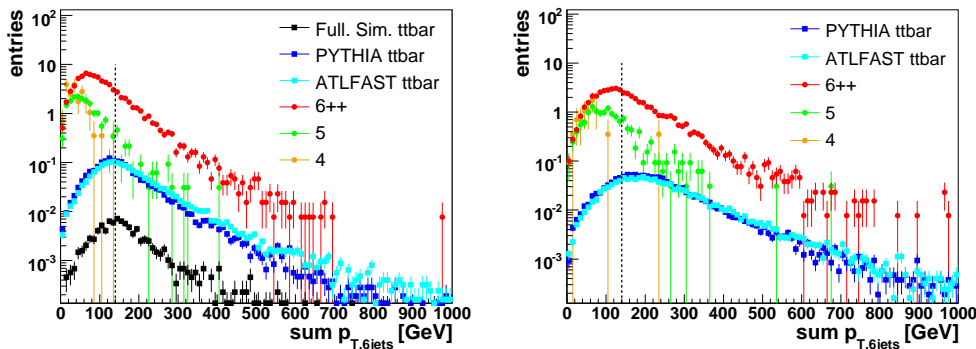


Figure 8.6: Sum of the six jets' p_T for events reconstructed from cells (left) and tracks (right). The black vertical line illustrates the position of the $\sum p_T$ -cut at 140 GeV. All events with a p_T sum of less than 140 GeV are discarded.

Another feature of fully hadronic $t\bar{t}$ events one can use to separate them from background is that the top quarks decay into two W bosons, which (after the decay into pairs of light quarks) further decay into jets. Therefore, it should be possible to reconstruct the masses of the two W bosons out of the jet masses resulting in two invariant dijet masses of about 80 GeV, respectively³.

The reconstruction of the two W masses was performed in the following way:

- 1) The four lowest p_T jets of the six jets in an event were regarded to result from

³80 GeV is the mass of the W boson [3].

the decay of the two W bosons⁴.

- 2) For each combination of pairs of two jets the invariant dijet masses were calculated:

$$m_{jet\ a, jet\ b} = \sqrt{(E_a + E_b)^2 - (p_{x,a} + p_{x,b})^2 - (p_{y,a} + p_{y,b})^2 - (p_{z,a} + p_{z,b})^2}$$

$$m_{jet\ c, jet\ d} = \sqrt{(E_c + E_d)^2 - (p_{x,c} + p_{x,d})^2 - (p_{y,c} + p_{y,d})^2 - (p_{z,c} + p_{z,d})^2}$$

In this context there are three possible (non-overlapping) jet-pair combinations in an event which are:

- (jet 3) (jet 4) and (jet 5) (jet 6)
- (jet 3) (jet 5) and (jet 4) (jet 6)
- (jet 3) (jet 6) and (jet 4) (jet 5)

- 3) The χ^2 , which expresses the difference between the dijet masses and the mass of the W boson of 80 GeV [3], was calculated for each pair of 2-jet combinations:

$$\chi_{(34),(56)}^2 = (m_{34} - m_W)^2 + (m_{56} - m_W)^2$$

$$\chi_{(35),(46)}^2 = (m_{35} - m_W)^2 + (m_{46} - m_W)^2$$

$$\chi_{(36),(45)}^2 = (m_{36} - m_W)^2 + (m_{45} - m_W)^2$$

- 4) The minimum of the three χ^2 values leads to the dijet combination forming the two W bosons in the regarded event.

The calculated two dijet masses, representing the invariant W masses, are illustrated in Figure 8.7 top for events from calorimeter cell entries and in Figure 8.7 bottom for the events from charged particle tracks.

⁴The two top quarks decay into two W bosons and two b -quarks ($t\bar{t} \rightarrow W^+W^-b\bar{b}$). The total momentum of the top quarks is split between these four particles. The W bosons split their momentum again between the two light quarks in which they decay, while the b -quarks will start hadronizing immediately. Thus, the four light quarks, originating from the decay of the W s, carry each about half of the momentum of the b -quarks. Consequently, the four lowest energetic jets in an event are likely to stem from the decay of the W bosons.

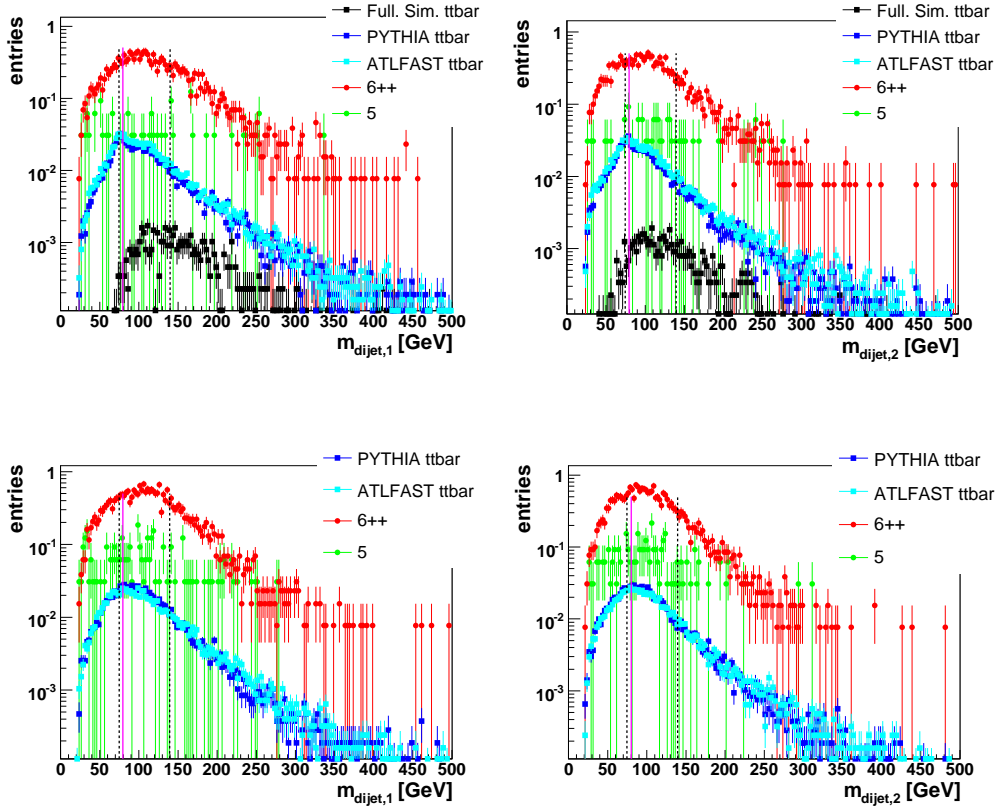


Figure 8.7: Top: Invariant dijet masses for calorimeter cell events. Bottom: Invariant dijet masses for charged particle track events.

The magenta line represents the mass of the W boson of 80 GeV. The two black lines illustrate the chosen cut for the dijet masses: $75 \text{ GeV} < m_{dijet} < 140 \text{ GeV}$. The events on the right and on the left of these two values are discarded.

The dijet masses in the $t\bar{t}$ events have their maxima around a value of 80 GeV (illustrated by the magenta vertical line), as expected. The 5-jet background events, plotted in green, have almost been eliminated by the previous cuts. However, the 6-jet background events still swamp the $t\bar{t}$ signal and cannot be separated easily by cutting on the dijet masses. Nevertheless, there is a tendency for the 6-jet background events to larger reconstructed dijet masses and therefore, a cut for the invariant dijet masses of $75 \text{ GeV} < m_{dijet} < 140 \text{ GeV}$ (represented by the two black vertical lines in Figure 8.7) was applied to discard as many 6-jet QCD background events as possible.

In the next step the invariant mass of three jets and thus, the invariant top-mass was calculated. Relying on the jet assignment for the W s the two combinations in the event were formed with the remaining two jets (*jet 1* and *jet 2*). Generally, there are two ways of combining the two remaining jets with the chosen jets pairs:

1)

$$\begin{aligned}
 & (jet\ a)(jet\ b)(jet\ 1) \text{ and } (jet\ c)(jet\ d)(jet\ 2) = \\
 & (m_{dijet1})(jet\ 1) \text{ and } (m_{dijet2})(jet\ 2)
 \end{aligned}$$

2)

$$(jet\ a)(jet\ b)(jet\ 2)\ \text{and}\ (jet\ c)(jet\ d)(jet\ 1) = \\ (m_{dijet1})(jet\ 2)\ \text{and}\ (m_{dijet2})(jet\ 1)$$

For each of these two combinations the χ^2 with respect to the mass of the top quark of 174 GeV [3] was calculated:

$$\chi_1^2 = (m_{dijet1, jet1} - m_t)^2 + (m_{dijet2, jet2} - m_t)^2$$

$$\chi_2^2 = (m_{dijet1, jet2} - m_t)^2 + (m_{dijet2, jet1} - m_t)^2$$

The minimum of the two χ^2 delivered the jet combination forming the two top quarks in the regarded event.

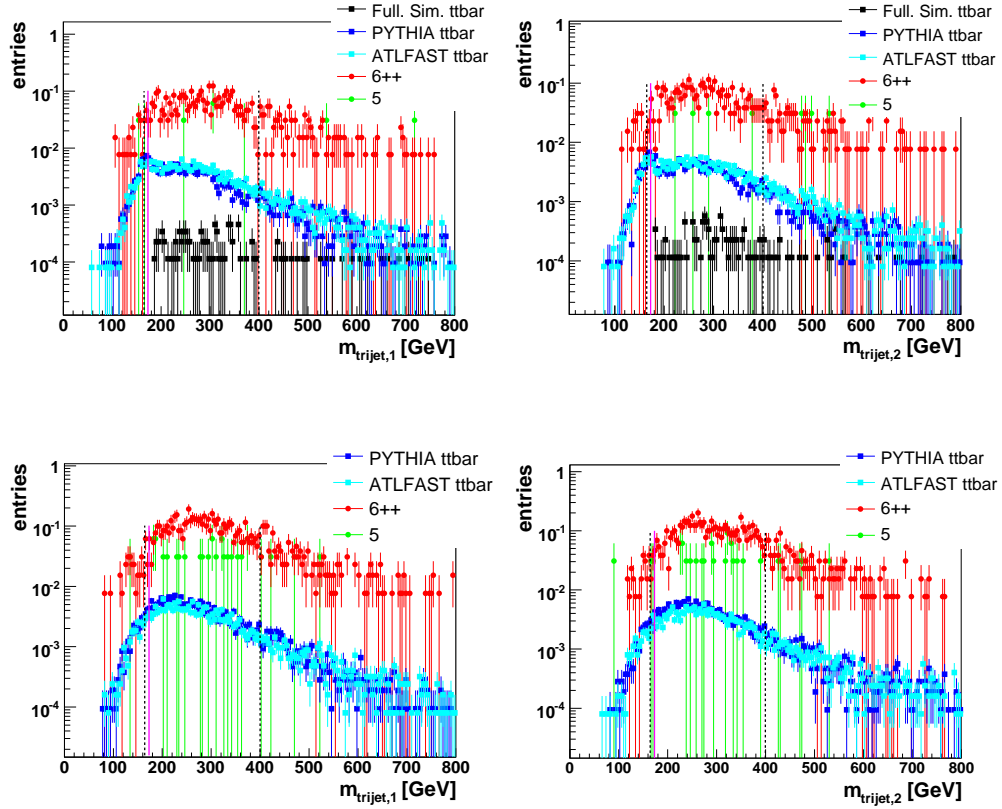


Figure 8.8: Invariant trijet masses for calorimeter cell events (top) and charged particle track events (bottom). The magenta line represents the mass of the top quark of about 174 GeV and the two black lines illustrate the chosen cut for the trijet masses of $165\ \text{GeV} < m_{trijet} < 400\ \text{GeV}$.

The results of the calculation of the invariant trijet masses are shown in Figure 8.8 for both calorimeter cell entries (Figure 8.8 top) and charged particle tracks (Figure 8.8 bottom).

The calorimeter cell $t\bar{t}$ events clearly show the top-mass peak⁵ at values of ≤ 174 GeV. The track events do not show such a distinct peak at the value of the top-mass as they contain only the charged particles⁶. The vertical magenta line in Figure 8.8 denotes the mass of the top quark. The events reconstructed from cell entries comprise only a few remaining 5-jet QCD events, whereas in the track events more 5-jet background events are left. In order to remove the remaining background events, a cut on the reconstructed top quark masses of $165 \text{ GeV} < m_{\text{trijet}} < 400 \text{ GeV}$ has been applied, indicated by the black vertical lines in Figure 8.8. However, due to the very similar final state topology of fully hadronic $t\bar{t}$ and 6-jet background events, this cut can only remove a small part of the remaining background.

The scalar jet- p_T sum for the jets, belonging to the two 3-jet combinations which form the top quarks, is shown in Figures 8.9 and 8.10.

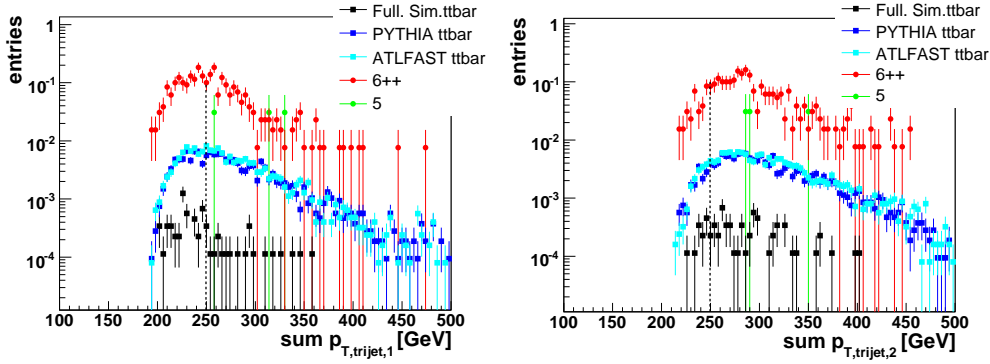


Figure 8.9: Scalar jet- p_T sum for the two 3-jet combinations forming the top quarks in the event, plotted for calorimeter cell events. The black line illustrates that all events with $\sum p_{T,\text{trijet}} > 250$ GeV remain.

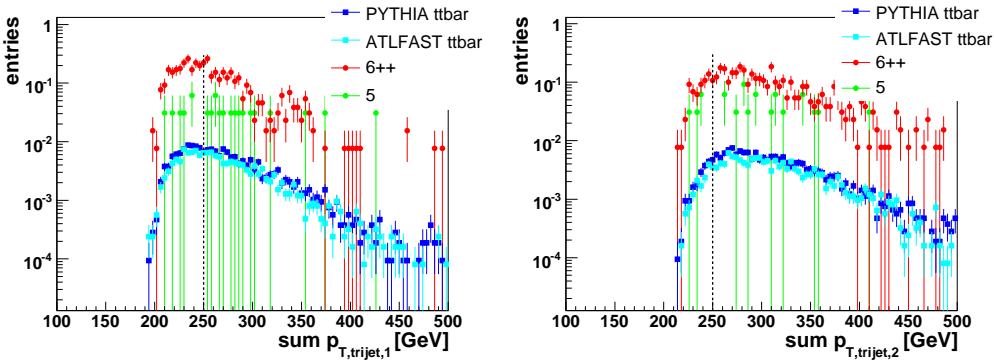


Figure 8.10: Scalar jet- p_T sum for the 3-jet combinations forming the top quarks in the regarded event for charged particle track events. Only events with $\sum p_{T,\text{trijet}} > 250$ GeV are selected, as indicated by the black vertical line.

⁵Note, that the reconstructed mass of the top quark is typically lower than its real mass.

⁶The neutral particles have been considered by multiplying the kinematic variables of the particle track events with a factor of $\frac{3}{2}$. However, this factor cannot reflect the properties of the neutral particles but accounts for the energy carried by the neutral particles.

Based on the fact that $t\bar{t}$ events tend to larger jet momenta, the next cut is applied on the scalar p_T sum at $\sum p_{T, trijet} \geq 250$ GeV, which is again illustrated by the black lines in the corresponding figures.

The next selection variables, regarded in this cut analysis, are the event shapes aplanarity, sphericity and the azimuthal event shape centrality [74].

The aplanarity⁷ defines how the jets in an event are placed with respect to a plane. It is a measure of the momentum component out of the event plane. The aplanarity can have any value between zero and $\frac{1}{2}$, where $A = 0$ denotes that the event is maximally planar, thus flat.

The sphericity⁸ defines how spherical the jets in an event are. If $S = 0$, the event is a 2-jet event and for $S = 1$, the event is maximally spherical, as shown in Figure 8.11.

In general, the $t\bar{t}$ events are expected to be more spherical and more aplanar than the background events due to the large top mass. But, as shown in Figures 8.1 and 8.2, this feature of the $t\bar{t}$ events gets almost lost at the LHC due to the high energies and therefore the boost of the generated particles. Consequently, a cut on the event shapes can only be applied at this stage of the cut analysis, after applying other cuts and when the main part of the background events has already been removed. Only at this stage there is a chance for a (further) separation of the $t\bar{t}$ signal by means of the topology variables.

Figure 8.12 left represents the event shapes for calorimeter cell events, still without a cut on an event shape. The sphericity and the centrality distributions of the $t\bar{t}$ events (see Figure 8.12 top and bottom) are almost completely swamped by the 6-jet background events. In the aplanarity distribution (Figure 8.12 middle), however, the $t\bar{t}$ events show a tendency to larger values. Therefore, a cut was chosen to reject the events at small aplanarity values: $A > 0.1$, indicated by the black vertical line in Figure 8.12 middle. The resulting distributions, after applying the cut on the aplanarity, are shown in Figure 8.12 right. Half of the remaining 6-jet background events could be removed. The 5-jet background has disappeared completely.

The corresponding distributions for the charged particle track events are shown in Figure 8.13. On the left there are again the plots before applying the cut on the aplanarity and on the right after cutting on the aplanarity at $A = 0.1$.

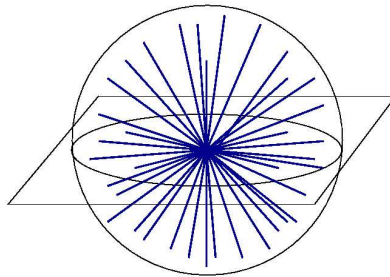


Figure 8.11: Sketch of an event with maximal sphericity and aplanarity ($S = 1$ and $A = \frac{1}{2}$) [84].

⁷ $A = \frac{3}{2}\lambda_3$, with λ_3 eigenvalue of the momentum tensor $\frac{\sum_i p_i^\alpha p_i^\beta}{\sum_i |p_i|^2}$ where $\alpha, \beta = x, y, z$.

⁸ $0 \leq S \leq 1$; $S = \frac{3}{2}(\lambda_2 + \lambda_3)$, where λ_2 and λ_3 are the eigenvalues of the momentum tensor $\frac{\sum_i p_i^\alpha p_i^\beta}{\sum_i |p_i|^2}$.

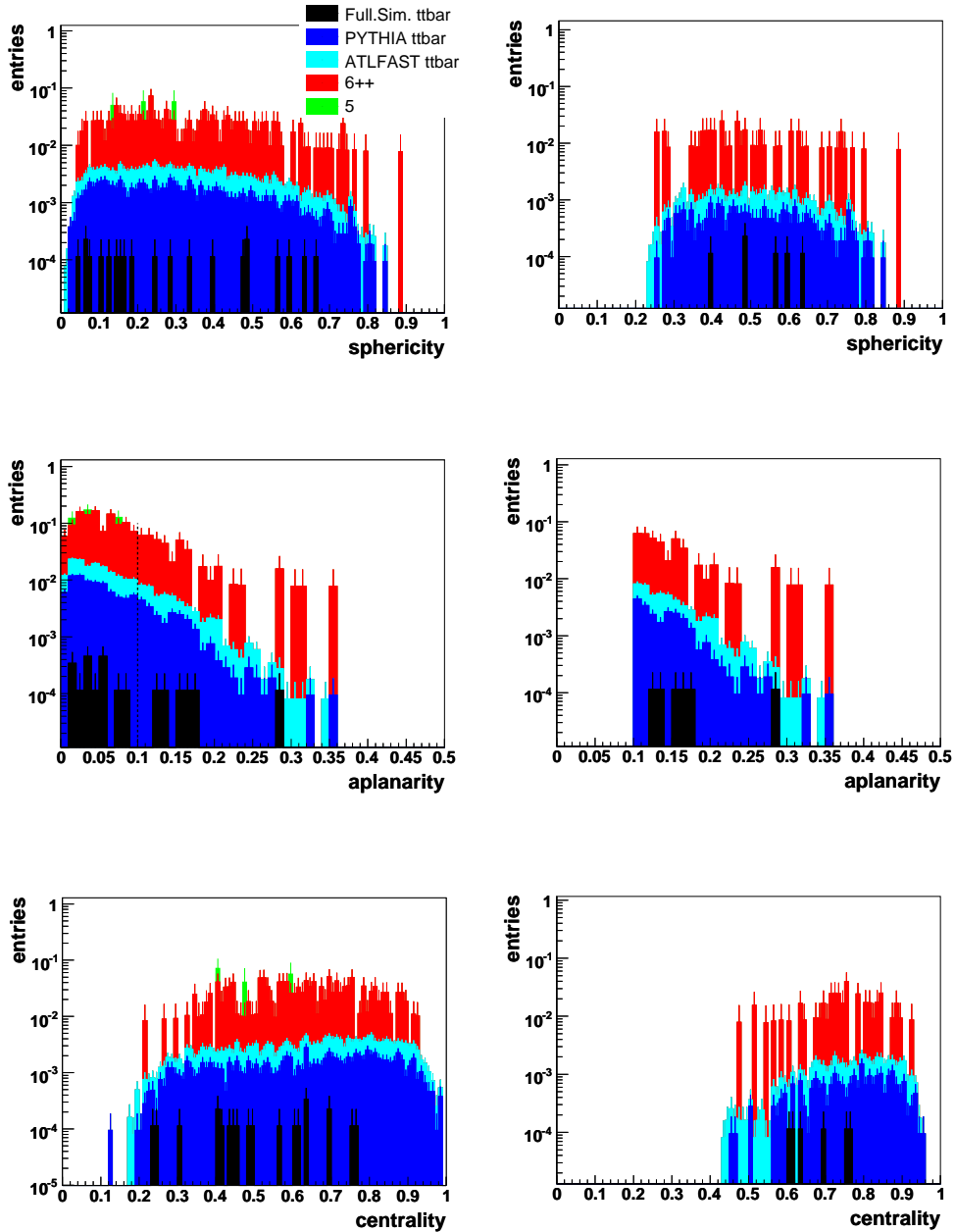


Figure 8.12: Stacked histogram showing the event shape distributions for calorimeter cell events. Top: Sphericity. Middle: Aplanarity. Bottom: Centrality. Left: Still without a cut on an event shape. Right: After applying a cut at the aplanarity $A > 0.1$.

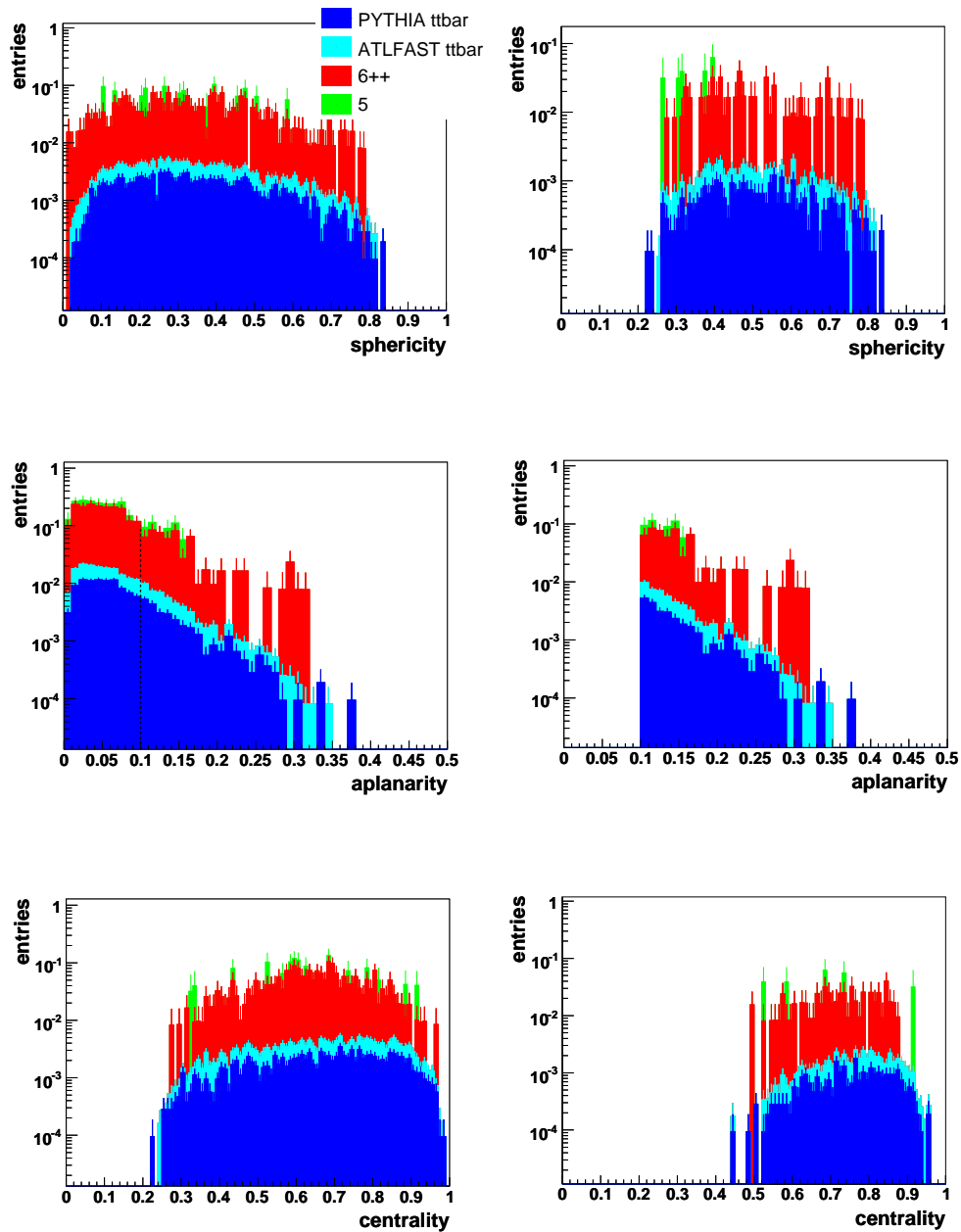


Figure 8.13: Event shapes for charged particle track events (stacked histogram). Top: Sphericity. Middle: Aplanarity. Bottom: Centrality. Left: Still without a cut on an event shape. Right: After applying a cut at $A > 0.1$.

Table 8.1 summarizes the cuts which have been motivated on the previous pages. A total number of eight cuts has been applied to separate the $t\bar{t}$ signal from the QCD multijet background.

Cuts	Tracks & Cells
#0	$ \eta_{\text{jet}} < 3$
#1	$N_{\text{jets}} = 6$
#2	$p_{T,\text{jet1}} > 115 \text{ GeV}$, $p_{T,\text{jet2}} > 90 \text{ GeV}$ $p_{T,\text{jet3}} > 70 \text{ GeV}$, $p_{T,\text{jet4}} > 55 \text{ GeV}$ $p_{T,\text{jet5}} > 40 \text{ GeV}$, $p_{T,\text{jet6}} > 30 \text{ GeV}$
#3	$\text{Sum } p_{T,\text{jet}} > 140 \text{ GeV}$
#4	$75 \text{ GeV} < m_{\text{dijet}} < 140 \text{ GeV}$
#5	$165 \text{ GeV} < m_{\text{trijet}} < 400 \text{ GeV}$
#6	$p_{T,\text{trijet}} > 250 \text{ GeV}$
#7	$A_{\text{planarity}} > 0.1$

Table 8.1: Summary of all cuts applied to the $t\bar{t}$ and background events.

The result of the cut analysis, including all the cuts which are listed in Table 8.1, is illustrated in the two cut-flow histograms, presented in Figure 8.14. The cut on the pseudorapidity of the jets is not shown explicitly but is included in the first cut which affects also the number of reconstructed jets in an event ($N_{\text{jets}} = 6$).

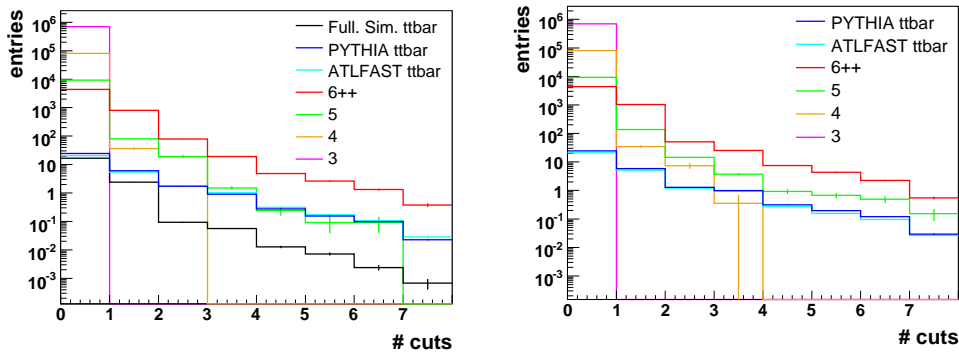


Figure 8.14: Cut-Flow histogram for events reconstructed from cell entries (left) and particle tracks (right).

Apparently, the 3-jet and 4-jet background events were already eliminated at the beginning of the cut-analysis with the cuts on the number of the jets or the sum of the jets' transverse momenta, respectively. Thus, this part of the QCD multijet background does not really pose a problem for the analysis of fully hadronic $t\bar{t}$ events.

For the cell entry events the 5-jet background was reduced to zero with the cut on the aplanarity, while for the track events there are still a few 5-jet QCD events left at the end of the cut analysis. The 6-jet QCD events, however, still dominate the $t\bar{t}$ events after applying the introduced cuts.

The number of events, which remain after all cuts have been applied, is listed in Table 8.2 and Table 8.3. Note, that for the residual 6-jet background events a factor of 81.8 (for the PYTHIA $t\bar{t}$ events) or 95.8 (for the ATLFAS $t\bar{t}$ events) must be considered⁹, which was implemented for scaling the 6-jet background events to the luminosity of the PYTHIA $t\bar{t}$ or ATLFAS $t\bar{t}$ events. For the 5-jet background events this factor amounts to 327 (PYTHIA $t\bar{t}$ events) or 383 (ATLFAS $t\bar{t}$ events).

	PYTHIA $t\bar{t}$	ATLFAS $t\bar{t}$	Full. Sim. $t\bar{t}$
# initial events	$259 \cdot 10^3$	$259 \cdot 10^3$	$174 \cdot 10^3$
# remaining events (Tracks)	313	331	n/a
# remaining events (Cells)	244	355	6

Table 8.2: Number of $t\bar{t}$ events which are left after applying the introduced cuts. The remaining fully simulated $t\bar{t}$ events for the events reconstructed from tracks have not been counted (n/a).

	6++	5	4	3
# initial events	$578 \cdot 10^3$	$302 \cdot 10^3$	$228 \cdot 10^3$	$224 \cdot 10^3$
# remaining events (Tracks)	71	5	-	-
# remaining events (Cells)	49	-	-	-

Table 8.3: Number of background events which are left after applying the introduced cuts.

The efficiency $\varepsilon_{t\bar{t}}$ for all used $t\bar{t}$ events is about 10^{-3} with $\frac{\Delta\varepsilon_{t\bar{t}}}{\varepsilon_{t\bar{t}}} = 0.002$. The efficiencies for the background events are listed in Table 8.4. The relative statistical uncertainty for the efficiency of the 6-jet background events comes to $\frac{\Delta\varepsilon_{6++}}{\varepsilon_{6++}} = 0.001$. For the remaining 3-jet, 4-jet and 5-jet background events it is $\frac{\Delta\varepsilon_{3,4,5}}{\varepsilon_{3,4,5}} = 0.002$.

$\int L dt = 10 \text{ fb}^{-1}$	ε_{6++}	ε_5	ε_4	ε_3
Tracks	$1 \cdot 10^{-4}$	$2 \cdot 10^{-5}$	$4 \cdot 10^{-6}$	$4 \cdot 10^{-6}$
Cells	$8 \cdot 10^{-5}$	$3 \cdot 10^{-6}$	$4 \cdot 10^{-6}$	$4 \cdot 10^{-6}$

Table 8.4: Efficiency ε for background events with $\frac{\Delta\varepsilon_{6++}}{\varepsilon_{6++}} = 0.001$ and $\frac{\Delta\varepsilon_{3,4,5}}{\varepsilon_{3,4,5}} = 0.002$.

Using calorimeter cell entries only, shown in Figure 8.14 left, the cut analysis leads to a S/B ratio of 1/16, resulting in a suppression factor of about 10000 for the 6-jet

⁹The scaling factors for the PYTHIA and the ATLFAS $t\bar{t}$ events are slightly different due to the slightly different luminosities of the two $t\bar{t}$ samples.

background events. Using charged particle tracks only, the S/B ratio amounts to $1/24$, also corresponding to a suppression factor of about 10000 for the 6-jet background¹⁰, as listed in Table 8.4.

These numbers correspond to 3330 remaining fully hadronic $t\bar{t}$ events, reconstructed from calorimeter cells, in the first year of the LHC at a still very low integrated luminosity¹¹ of 10 fb^{-1} . This is a quite large amount of $t\bar{t}$ events in comparison to the few hundred fully hadronic $t\bar{t}$ events per year which are produced at the Tevatron at full luminosity. For the track events this value amounts to 3700 remaining fully hadronic $t\bar{t}$ events in the start-up phase of the collider.

The signal to background ratios are presented in Table 8.5 for both the PYTHIA $t\bar{t}$ and the ATLFAST $t\bar{t}$ events.

$\int L dt = 10 \text{ fb}^{-1}$	S/B (PYTHIA $t\bar{t}$)	S/B (ATLFAST $t\bar{t}$)
Tracks	$\frac{1}{24}$	$\frac{1}{26}$
Cells	$\frac{1}{16}$	$\frac{1}{13}$

Table 8.5: Signal to background (S/B) ratios. For the calculation of the S/B ratio the scaling factors, as quoted above, were considered for scaling the 6-jet and 5-jet background events to the luminosity of the PYTHIA $t\bar{t}$ and ATLFAST $t\bar{t}$ events, respectively.

In order to estimate the effect of a possible b -tagging on the S/B ratio, an additional cut on the number of b -tagged jets ($N_{b\text{-jets}} \geq 1$ or $N_{b\text{-jets}} \geq 2$, respectively, see Figure 8.15) was added at the end of the cut analysis, which is illustrated by the last bin in the cut-flow histograms in Figure 8.16.

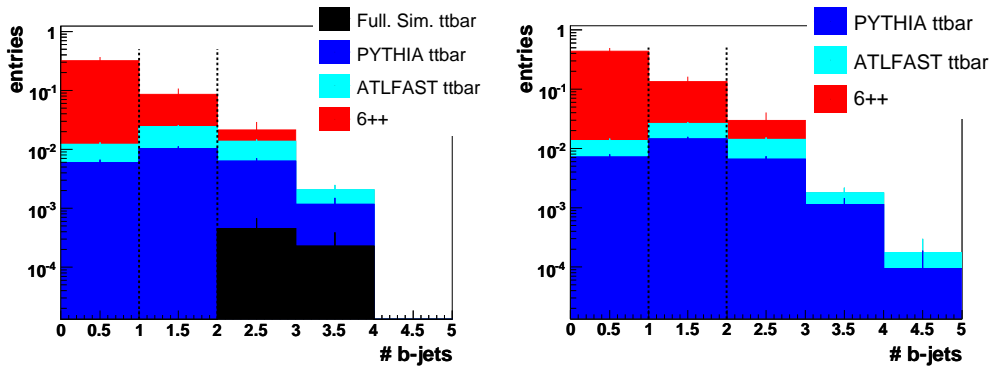


Figure 8.15: Number of b -tagged jets in calorimeter (left) and track (right) events. The two vertical lines show that with an additional single or double b -tag most of the remaining 6-jet background events can be removed. The distributions are illustrated with stacked histograms.

As the b -tagging strongly depends on the proper alignment of the detectors, which

¹⁰These numbers are based on the results from the PYTHIA $t\bar{t}$ events.

¹¹In this start-up period of the LHC $3.7 \cdot 10^6$ fully hadronic $t\bar{t}$ events are expected. This number has been multiplied by the $t\bar{t}$ efficiencies for getting the number of remaining $t\bar{t}$ events in the first LHC year.

cannot be guaranteed at the start-up of the LHC and the ATLAS detector, the b -tagging can only be a supplement to this study and therefore, was applied only at the end of this cut analysis. The histograms show that, if b -tagging works properly, the S/B ratio could be ameliorated up to 1/2 or unity for track or cell events (see double b -tag, Figure 8.16 bottom). With the additional double b -tag the 6-jet background events are then suppressed by a factor of $\approx 10^6$. The corresponding efficiencies for the additional single b -tag and the double b -tag can be found in Table 8.6 and 8.7.

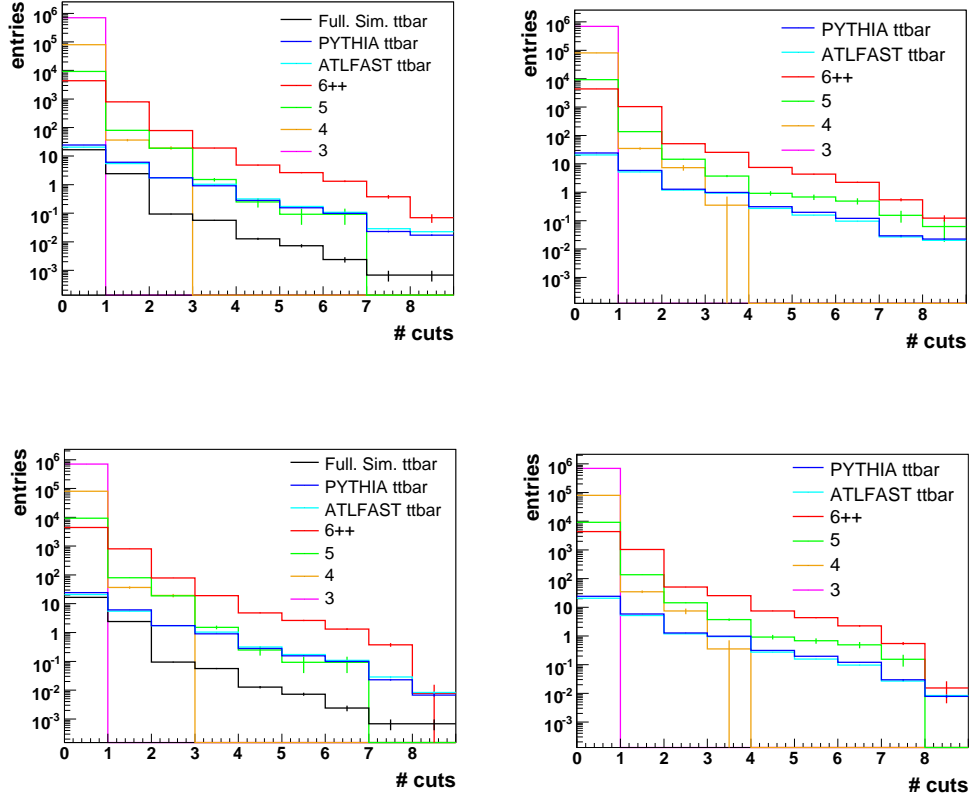


Figure 8.16: Cut-Flow histogram for events reconstructed from cell entries (left) and particle tracks (right). Top: With additional single b -tag (last bin). Bottom: With additional double b -tag (last bin).

$\int L dt = 10 \text{ fb}^{-1}$	ε (PYTHIA $t\bar{t}$)	ε (ATLFast $t\bar{t}$)
Tracks (single b -tag)	$9 \cdot 10^{-4}$	$1 \cdot 10^{-3}$
Cells (single b -tag)	$7 \cdot 10^{-4}$	$1 \cdot 10^{-3}$
Tracks (double b -tag)	$3 \cdot 10^{-4}$	$4 \cdot 10^{-4}$
Cells (double b -tag)	$3 \cdot 10^{-4}$	$4 \cdot 10^{-4}$

Table 8.6: Efficiency ε for $t\bar{t}$ events in case of an additional single or double b -tag. The relative statistical uncertainty comes to $\frac{\Delta\varepsilon_i}{\varepsilon_i} = 0.002$, respectively.

$\int L dt = 10 \text{ fb}^{-1}$	ε_{6++}	ε_5	ε_4	ε_3
Tracks (single b -tag)	$3 \cdot 10^{-5}$	$7 \cdot 10^{-5}$	$4 \cdot 10^{-6}$	$4 \cdot 10^{-6}$
Cells (single b -tag)	$2 \cdot 10^{-5}$	$3 \cdot 10^{-6}$	$4 \cdot 10^{-6}$	$4 \cdot 10^{-6}$
Tracks (double b -tag)	$3 \cdot 10^{-6}$	$3 \cdot 10^{-6}$	$4 \cdot 10^{-6}$	$4 \cdot 10^{-6}$
Cells (double b -tag)	$2 \cdot 10^{-6}$	$3 \cdot 10^{-6}$	$4 \cdot 10^{-6}$	$4 \cdot 10^{-6}$

Table 8.7: Efficiency ε for background events in case of an additional single or double b -tag with $\frac{\Delta\varepsilon_{6++}}{\varepsilon_{6++}} = 0.001$ and $\frac{\Delta\varepsilon_{3,4,5}}{\varepsilon_{3,4,5}} = 0.002$, respectively.

The S/B ratios for the additional cut on the number of reconstructed b -jets are presented in Table 8.8. When applying the double b -tag in addition to the previous cuts (Table 8.1), the resulting efficiencies for the $t\bar{t}$ events show that in the first year of the LHC a number of 1110 $t\bar{t}$ events would remain for both events reconstructed from calorimeter cells and charged particle tracks.

$\int L dt = 10 \text{ fb}^{-1}$	S/B (PYTHIA $t\bar{t}$)	S/B (ATLFAST $t\bar{t}$)
Tracks (single b -tag)	$\frac{1}{8}$	$\frac{1}{9}$
Cells (single b -tag)	$\frac{1}{4}$	$\frac{1}{3}$
Tracks (double b -tag)	$\frac{1}{2}$	$\frac{1}{2}$
Cells (double b -tag)	$\frac{1}{1}$	$\frac{1}{1}$

Table 8.8: Signal to background (S/B) ratios when a b -tag cut is applied in addition to the previously presented cuts.

Nevertheless, one must not forget that this b -tagging cut is only an extension to the presented cut analysis. It should not be relied on too much taking into account the conditions of the LHC and the ATLAS experiment in the first nominal year.

8.1.1 Interpretation of the results from the cut analysis

The situation in the first nominal year of the LHC is very difficult to assess. Quite a few components of the ATLAS detector might not yet be well configured. Therefore, it cannot be granted that all measured values of any events of interest will be fully reliable at this stage of the experiment.

This cut analysis, however, intends to apply already in the first year of the Large Hadron Collider and assumes a widely uncalibrated detector. Hence, it uses primarily quantities which are accessible at the very beginning of the ATLAS experiment and does in addition not rely on a sophisticated allocation of jets and partons for the calculation of the invariant dijet and trijet masses.

At any rate, the presented analysis and its results are strongly dependent on the modeling of the QCD multijet background. So far, the real properties of the background events (and even of the $t\bar{t}$ signal) at the LHC can only be guessed. The actual features

and the shape of the events will not be predictable in detail until the first real data will be available. The introduced cut analysis helps to characterize the properties of the events but it is only one possible approach to separate signal and background, as even slightly different properties of the events could change the whole result of any cuts and any cut analysis applied. In addition, caution is always advised when calculating the S/B ratios, as they are extremely sensitive to the number of remaining events and the corresponding scaling factors, which can be changed easily by modifying cuts, events' features and the number of the analyzed events.

At any rate, the cuts presented in this thesis and the corresponding results make clear that, even at the very beginning of the LHC at a low integrated luminosity of 10 fb^{-1} , it should be possible to extract more than 3000 fully hadronic $t\bar{t}$ events per year from the QCD multijet background. In this context signal to background ratios of 1/13 to 1/26 should be realistic.

Once the detector is properly aligned and all components act reliably, more sophisticated variables, like the identification of jets originating from b -quarks, can be used for the selection. Thus, the S/B ratios can be expected to become substantially enhanced with improving data quality (see Table 8.8).

8.2 Separation by the determination of the top-mass peak

This section treats the determination of the top-mass peak in fully hadronic $t\bar{t}$ events. In contrast to the cut analysis, presented in Section 8.1, a smaller signal to background ratio with a larger amount of surviving signal and background events is intended for a more realistic assessment of the impact and the remaining amount of the background events after the (pre)selection. The remaining number of signal and background events can be used to estimate the $t\bar{t}$ and QCD 6-jet events cross sections.

Again, the selected cuts account for the characteristics of the $t\bar{t}$ and background events, considering the technical possibilities in the start-up period of the LHC, as already described in Section 8.1. However, for the determination of a top-mass peak, which is more dependent on the quality of the studied quantities, a better calibrated detector must be assumed than for the case of the previously presented cut analysis.

The principle of this top-mass determination is based on a sophisticated allocation of the jets to their mother particles, thus, W bosons and b -quarks and above all the two top quarks.

At the beginning of the top-mass peak determination a cut on the number of jets was applied again¹² ($N_{\text{jets}} = 6$). Thereafter, for each combination of jets¹³ a χ^2 was calculated in the following way:

$$\chi^2 = (m_{top1} - m_{top2})^2 + (m_{W1} - m_W)^2 + (m_{W2} - m_W)^2,$$

where m_{top1} and m_{top2} are the calculated trijet masses for the current trijet combinations and m_{W1} and m_{W2} are the corresponding dijet masses for the current jet combination. m_W is the mass of the W boson ($m_W = 80 \text{ GeV}$ [3]).

The jet combination delivering the best, thus minimal χ^2 , was used as input for the

¹²The jets are all located within $|\eta_{jet}| < 3$ according to the technical ATLAS specification [32].

¹³There is a total number of 720 possible combinations for the events with exactly six final state jets.

calculation of the invariant masses and the determination of the top-mass peak.

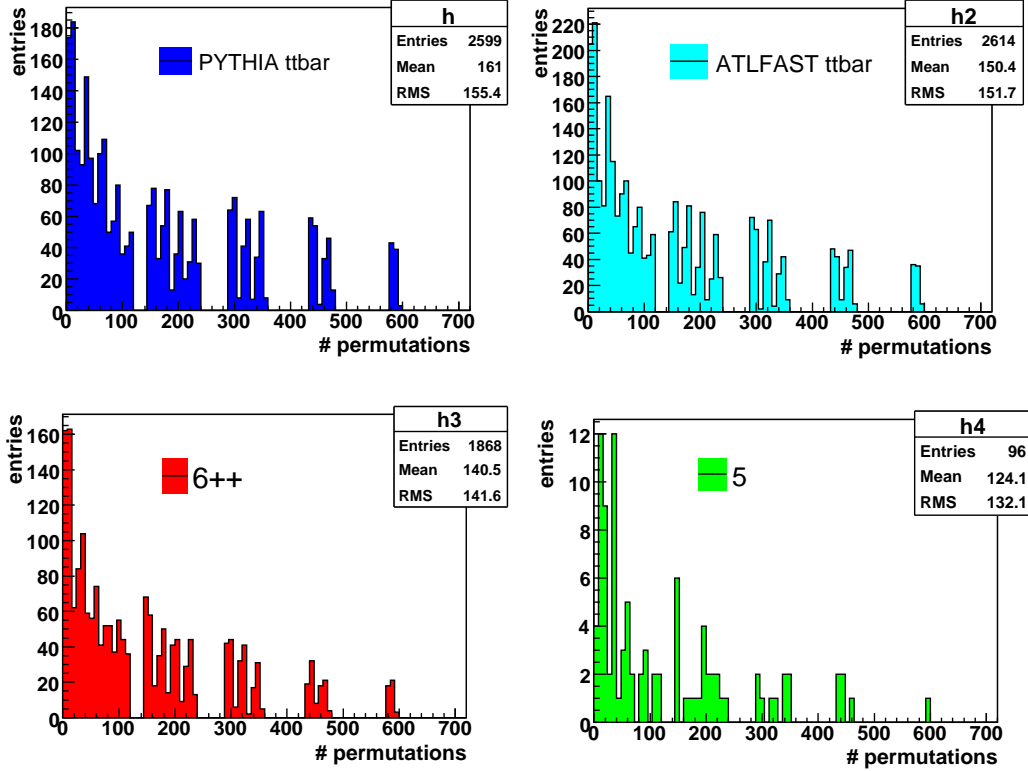


Figure 8.17: Number of permutations for $t\bar{t}$ and background events after which the best jet combination was found to form the two top quarks in an event. Top left: PYTHIA $t\bar{t}$ events. Top right: ATLFAST $t\bar{t}$ events. Bottom left: (Inclusive) QCD 6-jet events. Bottom right: QCD 5-jet events. Only events with $|\eta_{jet}| < 3$ and $N_{jets} = 6$ have been permuted.

Figure 8.17 top shows that in most cases the initial jet configuration for the allocation of the six jets to the two top quarks in $t\bar{t}$ events is the jet arrangement with the minimum χ^2 . As initial configuration of jets, however, the same configuration as for the cut analysis, described in the previous section, was chosen. Hence, the assumption that the highest energetic jets in an event are very likely to be the jets originating from the b -quarks seems mostly to be appropriate. The remaining four jets – which originate consequently from the decay of the two W bosons – are then combined with the two highest energetic (b -quark) jets to form the two top quarks.

After the best combination of jets has been found further selection cuts were applied to reduce the QCD multijet background. The chosen cuts aim to have only little effect on the shape and the characteristics of the background events in order to get a realistic estimation of the remaining background at the end of the separation.

Figure 8.18 shows the reconstructed masses of the two top quarks after the first two cuts ($N_{jets} = 6$ and $|\eta_{jet}| < 3$) have been applied. To simplify matters only the PYTHIA $t\bar{t}$ events have been used for the determination of the top-mass peak as the ATLFAST $t\bar{t}$ events differ only marginally from the PYTHIA $t\bar{t}$ sample (see previous

sections and also Chapter 7). The events have been reconstructed from calorimeter cell entries¹⁴. The $t\bar{t}$ sample shows clearly the top-mass peak at about 174 GeV, indicated by the magenta line. The 3-jet QCD events have already been eliminated by the first cuts.

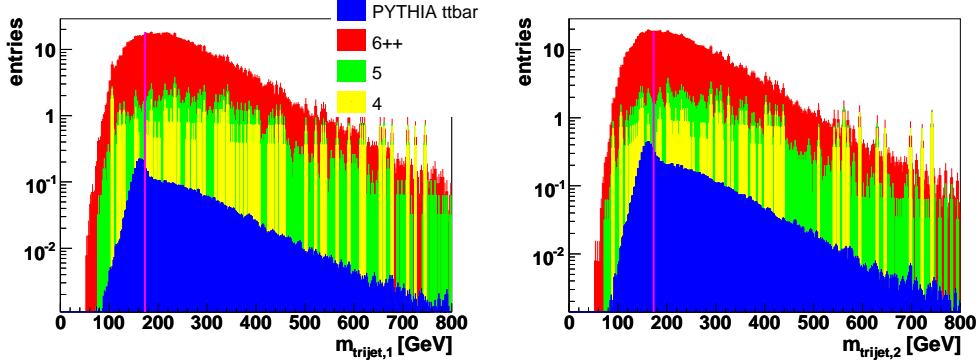


Figure 8.18: Reconstructed masses $m_{trijet,1}$ and $m_{trijet,2}$ of the two top quarks after the cut on the number of the jets ($N_{jets} = 6$) and the pseudorapidity of the jets ($|\eta_{jet}| < 3$). The events have been reconstructed from calorimeter cell entries. The histograms for signal and background events are added in stacked histograms. The magenta line indicates the mass of the top quark at about 174 GeV.

According to the fact that fully hadronic $t\bar{t}$ events tend to larger jet transverse momenta than QCD background events (see Section 8.1, Figure 8.4), lower limits were applied to the transverse momenta of the six jets, as already done in the cut analysis presented in the previous section. For the determination of the top-mass peak, however, looser cuts were chosen as a larger number of remaining $t\bar{t}$ (and also background) events is intended. Consequently, the following lower limits for transverse momenta p_T of the jets, which are also listed in Table 8.9, have been selected:

$$p_{T,jet1} > 90 \text{ GeV}, \quad p_{T,jet2} > 70 \text{ GeV}, \quad p_{T,jet3} > 50 \text{ GeV}$$

$$p_{T,jet4} > 45 \text{ GeV}, \quad p_{T,jet5} > 35 \text{ GeV}, \quad p_{T,jet6} > 25 \text{ GeV}$$

For the next cut the variable $\Delta p_{z,top} = p_{z,top1} - p_{z,top2}$ was determined, as presented in Figure 8.19. Obviously, the p_z of each of the two reconstructed top quarks in the $t\bar{t}$ events is very similar, pointed out by the peak around zero in Figure 8.19 left. In 6-jet background events the p_z for the two reconstructed top quark candidates varies and there is no distinct peak in the distribution for the background events. Therefore, only values of $-200 \text{ GeV} \leq \Delta p_{z,top} \leq 200 \text{ GeV}$ were chosen to skip a large amount of background events while keeping most of the $t\bar{t}$ events.

¹⁴For the determination of the top-mass peak only calorimeter cell events were used as they show a more distinct peak at 174 GeV than the events reconstructed from charged particle tracks, which is illustrated in Figure 8.8. This is caused by the fact that the particle track events contain only the charged and thus $\frac{2}{3}$ of all particles.

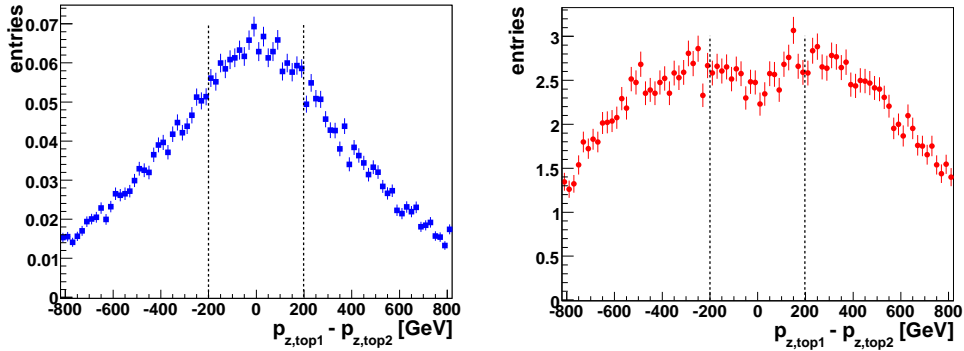


Figure 8.19: $\Delta p_{z,top}$ in $t\bar{t}$ (left) and QCD 6-jet background (right) events calculated after the $p_{T,jets}$ -cuts. The cut position is indicated by the black vertical lines.

The remaining number of events after the cuts on the transverse momenta of the jets and the $\Delta p_{z,top}$ cut is illustrated in the two histograms for the reconstructed top-masses (Figure 8.20).

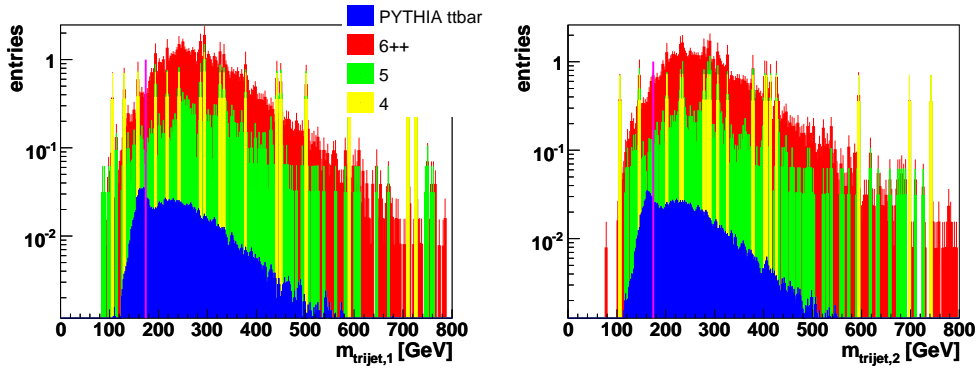


Figure 8.20: Reconstructed masses of the two top quarks after the $p_{T,jets}$ cuts and the $\Delta p_{z,top}$ cut (stacked histograms). The magenta line marks the position of the generated top-mass.

The main part of the 4-jet background events has been eliminated by the applied cuts. The characteristics of the 6-jet background events seem to be preserved after the application of the first cuts. The QCD 6-jet events still dominate the distributions. Thus, a cut on the sum of the transverse momenta of the six chosen jets ($\sum p_{T,6jets} > 120$ GeV) was applied in the next step, as presented in Figure 8.21. This cut removes nearly all remaining 4-jet and 5-jet QCD events and also discards a large amount of the 6-jet background events.

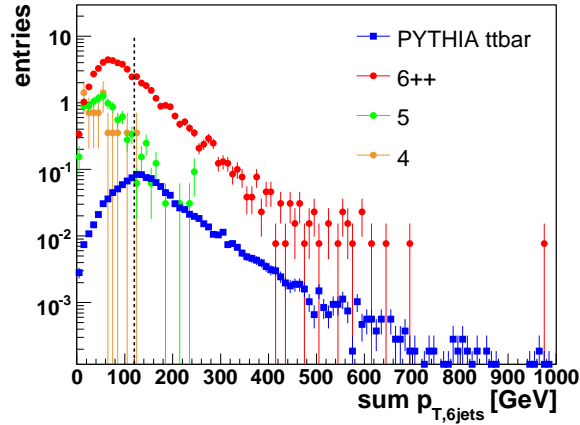


Figure 8.21: Sum of the transverse momenta of the six chosen jets. The black line shows that events with $\sum p_{T,6jets}$ of less than 120 GeV are discarded.

In the next step (after cutting away the events at $p_{T,6jets} > 120$ GeV) the values for the reconstructed dijet masses (reconstructed masses of the two W bosons in the events) have been limited to $70 \text{ GeV} < m_{dijet} < 90 \text{ GeV}$, as demonstrated in Figure 8.22.

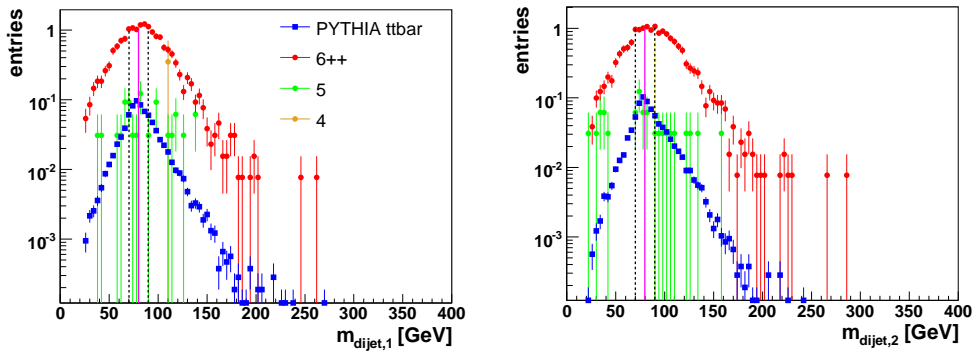


Figure 8.22: Reconstructed dijet masses for $t\bar{t}$ and background events plotted after the cut at $p_{T,6jets} > 120$ GeV. The magenta line indicates the mass of the W boson of 80 GeV [3], the two black lines illustrate the position of the cut on the reconstructed dijet masses: $70 \text{ GeV} < m_{dijet} < 90 \text{ GeV}$.

Due to the sophisticated allocation of the jets to their mother particles and the introduction of new or modified cuts, the W -mass peak in the $t\bar{t}$ events is clearer visible than for the reconstruction of the dijet masses in the previously presented cut analysis (Figure 8.7). The background events are widely spread around the value of the W boson-mass and can be reduced further by the cut on the reconstructed dijet masses. As – in this phase of the cut analysis – the remaining $t\bar{t}$ events show a tendency to

larger aplanarity values than the background events (Figure 8.23)¹⁵, the aplanarity was cut at small values: $A > 0.05$.

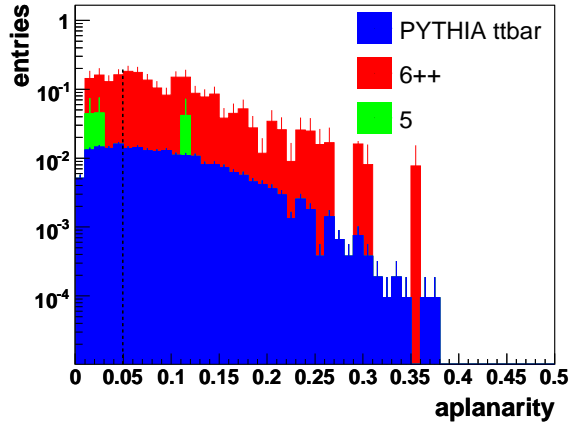


Figure 8.23: Aplanarity distribution for fully hadronic $t\bar{t}$ events and the residual background events presented with a stacked histogram. A cut was applied at small aplanarity values: $A > 0.05$ (black line). The histogram shows the aplanarity distributions after the cut on the reconstructed dijet masses.

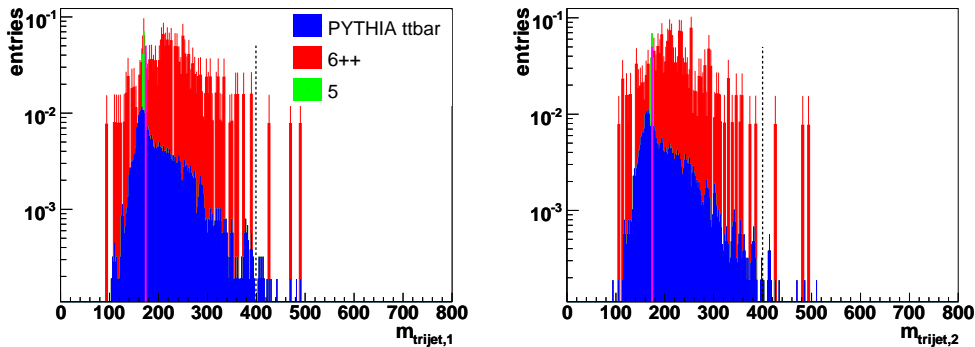


Figure 8.24: Reconstructed masses of the two top quarks after the cut on the aplanarity (stacked histograms). The $t\bar{t}$ events peak around the value of the top-mass (magenta line). Events with reconstructed top-masses above 400 GeV were discarded (black line).

Figure 8.24 shows the reconstructed top quark masses after the cut on the aplanarity. The QCD 6-jet events tend clearly to larger trijet masses than the $t\bar{t}$ events. This is also obvious from Figure 8.25, which presents a two dimensional diagram for the two reconstructed top-masses. The entries are more or less located around a line through the origin for both the $t\bar{t}$ and the QCD 6-jet events which shows the correlation of the presented two trijet masses.

¹⁵see also Section 8.1, Figure 8.12.

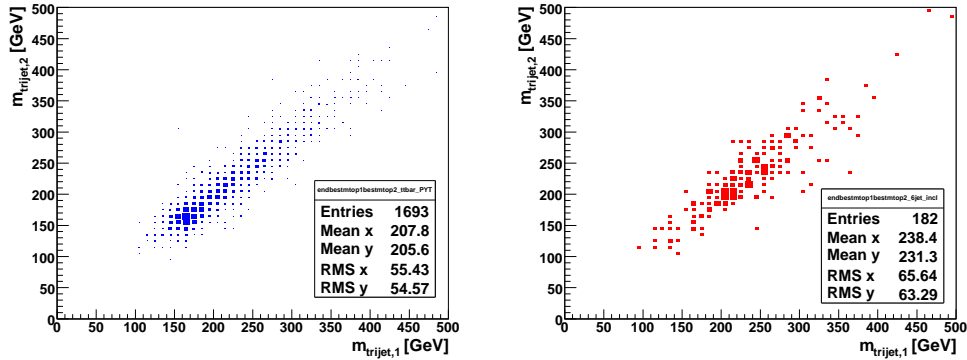


Figure 8.25: Reconstructed masses of the two top quarks after the cut on the aplanarity illustrated by a two dimensional histogram. The box area corresponds to the number of entries. Left: $t\bar{t}$ events. Right: QCD 6-jet background events.

After applying all cuts the reconstructed mass of the top quark was limited¹⁶ to values below 400 GeV. After the cut at $m_{\text{trijet}} < 400$ GeV a Landau function was fitted to the remaining QCD 6-jet events. This helps to assess the amount and the characteristics of the main part of the background events after the application of separation cuts. The corresponding distribution including the fit of the 6-jet background events is provided in Figure 8.26.

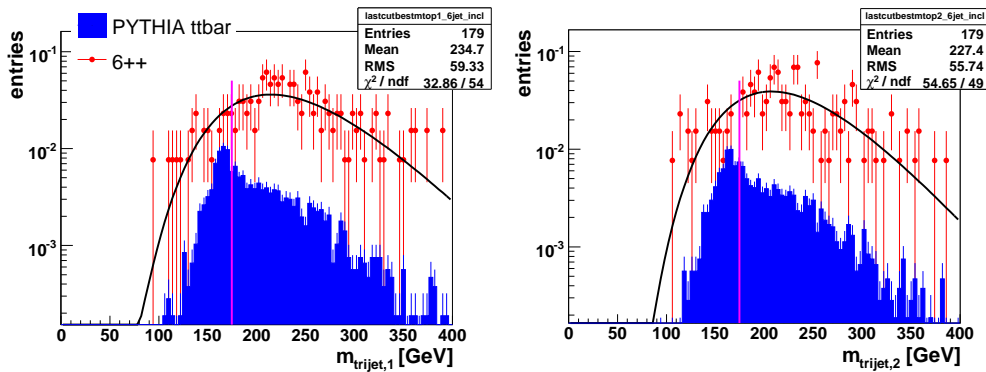


Figure 8.26: Reconstructed masses of the two top quarks after cutting $m_{\text{trijet}} < 400$ GeV. The residual QCD 6-jet events have been fitted with a Landau function.

Obviously, the background events are spread around a maximum at about 220 GeV. Therefore, the distribution for the QCD 6-jet events is clearly shifted to larger reconstructed top quark masses than it is the case for the $t\bar{t}$ signal events. Nonetheless, even after the separation cuts, which reduce the 6-jet background events by a factor

¹⁶This limitation does not really affect the separation of the $t\bar{t}$ events from the background but was chosen to illustrate the fit to the remaining background events in a better way, which was applied in the range of 0 GeV – 400 GeV.

of about 10^{-4} (see Table 8.11), it is quite difficult to distinguish the $t\bar{t}$ signal from the 6-jet background events.

A summary of all cuts can be found in Table 8.9. Table 8.10 shows how many events are still left after the cut analysis, while Table 8.11 lists the corresponding efficiencies.

	Cuts
#0	$ \eta_{\text{jet}} < 3$
#1	$N_{\text{jets}} = 6$
#2	$p_{T,\text{jet}1} > 90 \text{ GeV}$, $p_{T,\text{jet}2} > 70 \text{ GeV}$ $p_{T,\text{jet}3} > 50 \text{ GeV}$, $p_{T,\text{jet}4} > 45 \text{ GeV}$ $p_{T,\text{jet}5} > 35 \text{ GeV}$, $p_{T,\text{jet}6} > 25 \text{ GeV}$
#3	$-200 \text{ GeV} \leq \Delta p_{z,\text{top}} \leq 200 \text{ GeV}$
#4	Sum $p_{T,\text{jet}} > 120 \text{ GeV}$
#5	$70 \text{ GeV} < m_{\text{dijet}} < 90 \text{ GeV}$
#6	Aplanarity > 0.05
#7	$m_{\text{trijet}} < 400 \text{ GeV}$

Table 8.9: Summary of all cuts applied to the $t\bar{t}$ and background events.

	PYTHIA $t\bar{t}$	6++	5	4	3
# initial events	$259 \cdot 10^3$	$578 \cdot 10^3$	$302 \cdot 10^3$	$228 \cdot 10^3$	$224 \cdot 10^3$
# remaining events	1674	179	1	-	-

Table 8.10: Number of PYTHIA $t\bar{t}$ and background events which are left after applying the introduced cuts.

$\int L dt = 10 \text{ fb}^{-1}$	$\varepsilon_{t\bar{t}}$	ε_{6++}	ε_5	ε_4	ε_3
	$6 \cdot 10^{-3}$	$3 \cdot 10^{-4}$	$3 \cdot 10^{-6}$	$4 \cdot 10^{-6}$	$4 \cdot 10^{-6}$

Table 8.11: Efficiency ε for $t\bar{t}$ and background events. The relative statistical uncertainty amounts to $\frac{\Delta\varepsilon}{\varepsilon} = 0.002$ for the $t\bar{t}$ as well as the 3-jet, 4-jet and 5-jet background events, while $\frac{\Delta\varepsilon_{6++}}{\varepsilon_{6++}}$ comes to 0.001.

The cut-flow histogram (Figure 8.27) illustrates that the 3-jet and 4-jet background events could be eliminated very easily, as already demonstrated in the previous section. The 6-jet background events, however, still dominate the distributions and in contrast to the results for the cut analysis in Section 8.1 there are also remaining 5-jet background events due to the softer separation cuts. However, as the characteristics of the 5-jet background events are sufficiently different from those of the $t\bar{t}$ events and

due to the tiny statistics of the residual events, the remaining 5-jet background does not really pose a problem for the separation of the $t\bar{t}$ signal from the background.

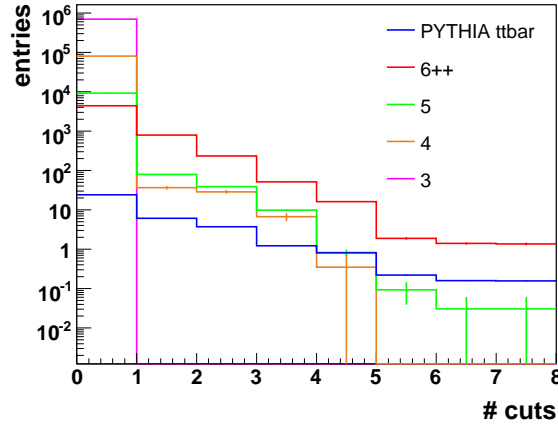


Figure 8.27: Cut-flow histogram for PYTHIA $t\bar{t}$ and QCD multijet background events.

The signal to background ratio of the cut analysis for the determination of the top-mass peak amounts to $S/B = \frac{1}{9} \pm 0.009$ if no error is assumed for the remaining 5-jet QCD events¹⁷, as presented in Table 8.12. If an upper limit of 4.74 events¹⁸ is estimated for the remaining number of 5-jet QCD events the signal to background ratio amounts to $S/B = \frac{1}{10}$ (Table 8.12).

$\int L dt = 10 \text{ fb}^{-1}$	S/B	S/B (upper limit for 5-jet)
	$\frac{1}{9} \pm 0.009$	$\frac{1}{10}$

Table 8.12: Signal to background (S/B) ratio. Note, that for the calculation of the S/B ratio the scaling factors of 81.8 for the 6-jet QCD events and 327 for the 5-jet QCD events must be considered for scaling the background events to the luminosity of the $t\bar{t}$ events. If an upper limit of 4.74 events (at 95 % CL [3]) for the remaining 5-jet background events is considered the S/B ratio amounts to $\frac{1}{10}$.

Due to the looser separation cuts at this cut analysis, the remaining 6-jet QCD and $t\bar{t}$ statistics is sufficient for specifying the corresponding surviving cross sections. The results for this cross section calculation can be found in Table 8.13. As expected the cross sections reflect exactly the calculated S/B ratio of $\frac{1}{9}$.

In summary, also after the presented top-mass peak separation with adapted selection cuts (except from b -tagging) and the optimal allocation of the jets to their mother particles, the $t\bar{t}$ signals are still dominated by the 6-jet QCD background.

¹⁷This assumption is reasonable due to the almost negligible number of remaining 5-jet background events.

¹⁸Due to the small statistics, this limit was estimated with Poisson statistics for a confidence level of 95 % [3].

This situation will become even more difficult when the distributions of signal and background cannot be examined separately any more but the $t\bar{t}$ signal is to be extracted from real data. Then the first step is to assign the available distributions and event characteristics to the different types of events, thus $t\bar{t}$ signal or QCD background.

$\sigma_{rest,t\bar{t}} = \sigma_{t\bar{t}} \cdot \epsilon_{t\bar{t}}$	$\sigma_{rest,6++} = \sigma_{6++} \cdot \epsilon_{6++}$
1 pb	9 pb

Table 8.13: Cross sections for the $t\bar{t}$ and QCD 6-jet background events calculated with the production cross sections (see Table 7.1 and Table 7.2) and the efficiencies for the $t\bar{t}$ and QCD 6-jet events (Table 8.11).

In order to demonstrate the top-mass peak in a better way, the remaining $t\bar{t}$ events and the 6-jet background events, represented in Figure 8.26, were both scaled¹⁹ by a factor of about 10000 corresponding to an integrated luminosity of 1560 pb^{-1} . In the next step the scaled signal was added to the scaled background distribution to pretend a distribution which is expected from real data and which does not allow an instant allocation of the contained events to the signal or the background any more. The corresponding distribution was then fitted with a Landau function and in addition with a Gauss function, which was chosen to describe the top-mass peak. The result is shown in Figure 8.28. The two distributions for the reconstructed top quark masses clearly show the top peak at about 174 GeV.

For estimating the statistical uncertainty of the $t\bar{t}$ cross section at different integrated luminosities the function $\frac{\Delta S}{S} \sim \frac{\Delta \sigma_{t\bar{t}}}{\sigma_{t\bar{t}}}$ was determined by means of the remaining $t\bar{t}$ and 6-jet background events in a selected area around the reconstructed top-mass peak ($\approx 157 \text{ GeV} - \approx 177 \text{ GeV}$). Defining

$$N_{t\bar{t}} =: S$$

and

$$N_{6-jet} =: B$$

such that

$$N := S + B.$$

ΔN and ΔS were calculated using Gauss error propagation

$$\Delta N = \sqrt{\sqrt{S}^2 + \sqrt{B}^2}$$

$$\Delta S = \sqrt{(\Delta N)^2 + \sqrt{B}^2}.$$

The corresponding distribution for $\frac{\Delta S}{S}$ at different integrated luminosities is shown in Figure 8.30, where the displayed graphs represent the mean of the two values for $\frac{\Delta S}{S}$ for the two reconstructed top quarks.

¹⁹This was not a mere scaling of the few remaining events but the shape of the remaining background, as determined from the Landau fit shown in Figure 8.26, was kept.

At phase 1, which will be reached by autumn 2008 [30], an integrated luminosity of $\int L dt \approx 3 \text{ pb}^{-1}$ will be available. By the end of 2008 the luminosity will rise to 1 fb^{-1} (stage 2 [30]), while after one year of LHC a luminosity of 10 fb^{-1} is predicted.

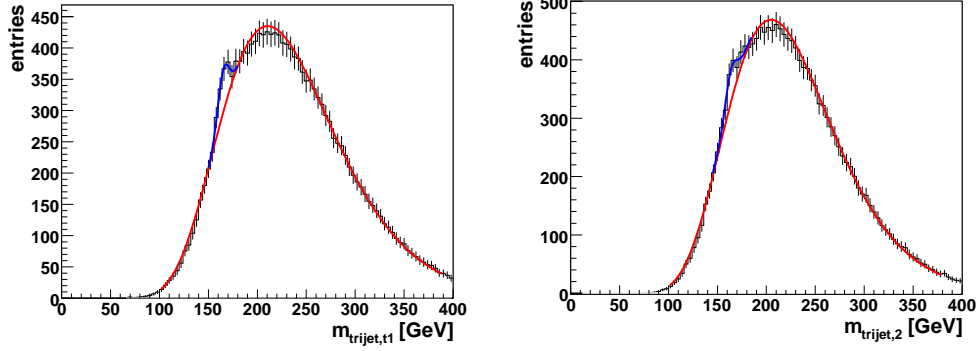


Figure 8.28: Added distributions for the remaining $t\bar{t}$ and 6-jet background events presenting the two reconstructed top quark masses. The $t\bar{t}$ and 6-jet background events have been scaled by a factor of about 10000 in order to demonstrate the top-mass peak.

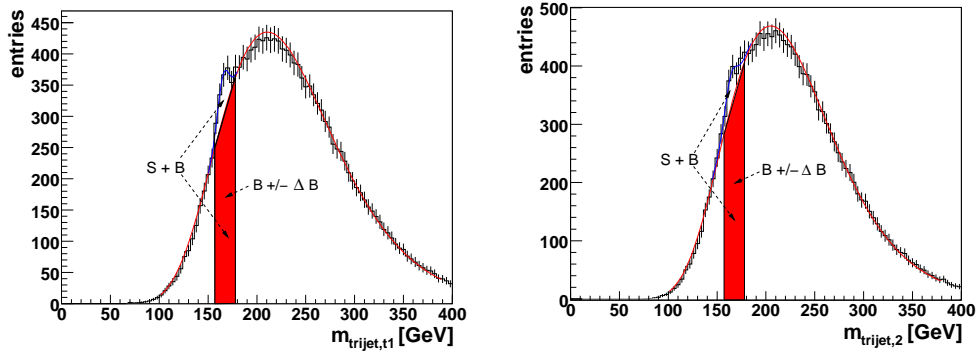


Figure 8.29: Added distributions for the remaining $t\bar{t}$ and 6-jet background events presenting the two reconstructed top quark masses. The integral of the Landau fit for the QCD 6-jet events in the selected area was used to obtain the number of remaining QCD 6-jet events and the corresponding errors $B \pm \Delta B$ in order to determine $\frac{\Delta S}{S}$ by means of the applied fit function at an assumed luminosity of 1560 pb^{-1} (see red symbol in Figure 8.30).

An additional calculation of $\frac{\Delta S}{S}$, using the Landau fit (Figure 8.26) which describes the 6-jet background events, was performed at the assumed integrated luminosity of $\int L dt = 1560 \text{ pb}^{-1}$ (see red symbol in Figure 8.30). The integral of the fit function was used to determine the value for $B \pm \Delta B$ in the previously selected area of $157 \text{ GeV} - 177 \text{ GeV}$, as shown in Figure 8.29. With the integral of the histogram for the added QCD 6-jet events and the $t\bar{t}$ events (Figure 8.29) the total number of remaining events $S + B$ in the given area has been calculated. Thus, a second value for $\frac{\Delta S}{S}$ could be determined using the smaller error ΔB provided by the fit function. The calculated

value agrees very well with the results obtained with the method for calculating $\frac{\Delta S}{S}$ outlined previously, as illustrated in Figure 8.30. For a logarithmic description of the different luminosities (Figure 8.30 right) the distribution describes – as expected – a straight line.

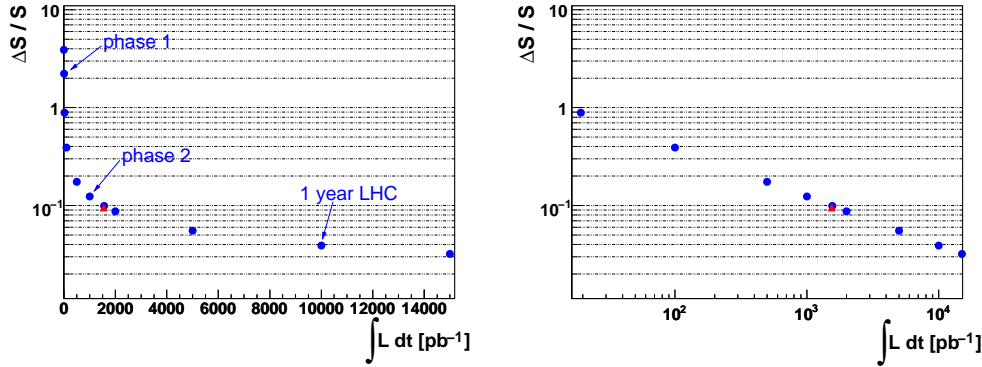


Figure 8.30: $\frac{\Delta S}{S} \sim \frac{\Delta\sigma_{\bar{t}t}}{\sigma_{\bar{t}t}}$ for fully hadronic $t\bar{t}$ events at different integrated luminosities. The red symbol represents the value obtained by means of the Landau fit function describing the remaining 6-jet background events. "phase 1" and "phase 2" represent the luminosities reached by autumn 2008 and by the end of 2008, respectively [85]. After one year of LHC an integrated luminosity of about 10 fb^{-1} will be achieved ("1 year LHC"). For a logarithmic description of the x-axis (right) the entries show the characteristics of a straight line with slope $-\frac{1}{2}$.

Figure 8.30 shows that at about 19 pb^{-1} , which equals the luminosity derived from the production cross section of the 6-jet QCD background events, the $t\bar{t}$ cross section can be determined only with an error of about 100 %. In phase 1, comprising even smaller luminosities ($\int L dt \approx 3 \text{ pb}^{-1}$ [30]), a relative uncertainty of about 225 % will only be possible. Nevertheless, with rising luminosity the accuracy ameliorates very quickly and at 10 fb^{-1} a statistical accuracy of about 4 % will be achieved for the determination of the cross section of fully hadronic $t\bar{t}$ events.

8.2.1 Interpretation of the top-mass peak results

The determination of the top-mass peak by means of a cut analysis using adapted cuts and a sophisticated allocation of the jets to their mother particles shows due to the small remaining statistics (Table 8.10) that it will be very difficult to reconstruct the top-mass peak from fully hadronic $t\bar{t}$ decays at the very beginning of the LHC and the ATLAS experiment. However, the scaled distributions of $t\bar{t}$ and background events, which correspond to an integrated luminosity of $\int L dt = 1560 \text{ pb}^{-1}$, show that after reaching phase 2 of the LHC²⁰ the statistics of the remaining $t\bar{t}$ events will be large enough to estimate and extract the top-mass peak from the QCD multijet background events. Therefore, even at the high luminosities reached at the LHC and despite the fact that – in contrast to the events at the Tevatron – the top quark and QCD events are produced with a certain boost along the beam axis it will be possible to find a top-mass

²⁰At phase 2 luminosities of about 1000 pb^{-1} will be available [30].

peak from fully hadronic $t\bar{t}$ events – using a sophisticated selection to reduce the backgrounds for the $t\bar{t}$ events.

At stage 2 of the collider experiment the $t\bar{t}$ cross section can be determined with an error of approximately 9 – 10 %, while after one year of the LHC at integrated luminosities of about 10 fb^{-1} a statistical accuracy for the cross section determination of fully hadronic $t\bar{t}$ events of $\approx 4 \%$ will be possible. This error for the cross section determination will still further decrease with the rising integrated luminosities (i.e. 3 % at $\int L dt = 15 \text{ fb}^{-1}$, see Figure 8.30) during the run-time of the LHC and the ATLAS experiment.

Chapter 9

Summary

Due to its large mass of around 174 GeV the top quark has an exceptional position among the quarks of the Standard Model. With the start of the LHC with very high collision energies of up to 14 TeV it will be possible to measure and analyze the properties of the top with much higher accuracy than in previous experiments, for example at the Tevatron. Additionally, because of the high luminosities provided by the LHC, top quark properties can be investigated also in final states which are affected by significant background processes. For instance, the fully hadronic $t\bar{t}$ decays, which account for almost half of the total $t\bar{t}$ decays, can be studied in the background environment of strong interactions.

The theory of Quantum Chromo Dynamics, which describes the strong interaction between colour-charged particles, is one of the most interesting but complicated parts of the Standard Model. Thus, a realistic estimation of the real properties of QCD multijet events at LHC energies and also a prediction of the influence of these events on the fully hadronic $t\bar{t}$ events might be difficult. Nevertheless, simulation studies of QCD events help to assess the properties of fully hadronic $t\bar{t}$ and QCD events in the absence of real data.

This thesis deals with the characteristics of fully hadronic $t\bar{t}$ decays and QCD multijet background events as well as the separation of the $t\bar{t}$ signal from the background in the first year of the ATLAS experiment at the LHC. Since in the start-up period the ATLAS detector will neither be completely understood nor fully calibrated, the analysis of the events is based on the few physical quantities available from the very beginning of the ATLAS experiment. Fully hadronic $t\bar{t}$ events, comprising six or more highly energetic jets in the final state, and QCD multijet events have a very similar final state topology. Since the QCD events have a much larger cross section, they dominate the $t\bar{t}$ events by several orders of magnitude. Hence, it is a huge challenge to separate the $t\bar{t}$ signal from the background, requiring a diligent study of the characteristics of both kinds of events and the application of sophisticated separation cuts which are adapted to both the high collision energies at the LHC and the available information in the start-up period.

In this study different kinds of Monte Carlo generators and simulation programs have been used for the production and further processing of the simulated events. The jet reconstruction has been performed with the k_T algorithm in exclusive mode, which is especially suitable for the reconstruction of proton-proton collision events at hadron colliders which comprise many jets in the final state. The characteristics of the simu-

lated signal and background events have been studied and compared. Following this comparison a cut-based selection of the $t\bar{t}$ signal events was developed such that a top-mass peak could be observed. Depending on the applied cuts a suppression factor for the 6-jet QCD background events of 10^4 to 10^6 could be reached, while a $t\bar{t}$ selection efficiency of about one permill was maintained.

The results of the cut analysis show that already in the first nominal year of the LHC at an integrated luminosity of 10 fb^{-1} it will be possible to separate more than 3000 $t\bar{t}$ events from the QCD background. This number is very large when compared to the 100's of fully hadronic $t\bar{t}$ events which are selected at the Tevatron per year at full luminosity. As soon as the ATLAS detector is properly aligned, even more sophisticated cuts – like the identification of jets originating from b -quarks – can be applied which facilitate the identification of the $t\bar{t}$ events (and aid with the elimination of QCD events). This will further increase the number of remaining fully hadronic $t\bar{t}$ events yielding a signal to background ratio of unity.

In addition, this thesis confirms that already in the start-up period of ATLAS and despite the production of $t\bar{t}$ events with non-negligible transverse momentum (p_T) due to the large LHC collision energies, it is possible to reconstruct a top-mass peak in fully hadronic $t\bar{t}$ events when using elaborate separation cuts to reduce the QCD background events. By means of the results of the top-mass peak reconstruction it can also be concluded that with an integrated luminosity of 10 fb^{-1} the $t\bar{t}$ production cross section can be measured with a relative statistical uncertainty of 4 %.

Appendix A

Limitation of the phase space for the production of fully hadronic $t\bar{t}$ events in PYTHIA

As indicated in Section 6.2.1 the PYTHIA switch CKIN(3,100.) [13], which sets a lower limit of 100 GeV to the momentum transfer q in the hard $2 \rightarrow 2$ process (see Figure A.1 left), cuts the phase space for the production of the $t\bar{t}$ events. This leads to a $t\bar{t}$ production cross section which is almost by factor two smaller than for events produced with a considerably smaller lower limit¹ of the p_T transfer in the hard interaction [13].

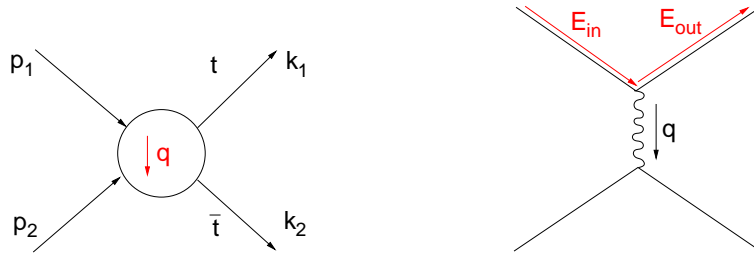


Figure A.1: Left: Illustration of the hard $2 \rightarrow 2$ process for the production of a pair of top quarks. p_1 , p_2 denote the incoming partons, k_1 and k_2 are the outgoing partons. q is the momentum transfer in the hard $2 \rightarrow 2$ process. Right: Energy transfer in the hard scattering.

With CKIN(3,100.) the momentum transfer q in the hard scattering comes to

$$|q| = |p_1 - k_1| = |k_2 - p_2| \geq 100 \text{ GeV} ,$$

where p_1 , p_2 denote the incoming partons and k_1 , k_2 the outgoing partons in the hard $2 \rightarrow 2$ process. Therefore, it applies that

$$|p_2|^2 = |k_2 - q|^2 = k_2^2 - 2k_2q + q^2$$

¹For comparison a lower limit of 10 GeV was tested and the results were compared with the 100 GeV sample.

and

$$|p_1|^2 = |k_1 + q|^2 = k_1^2 + 2k_1q + q^2 .$$

With $k_1^2 = k_2^2 = m_t^2$, the centre-of-mass energy in the hard collision equals to²

$$(k_1 + k_2)^2 = (p_1 + p_2)^2 \geq 4m_t^2 ,$$

where s is the centre-of-mass energy squared.

Therefore, the resulting distribution for p_2^2 versus p_1^2 is a hyperbola, as indicated in Figure A.2.

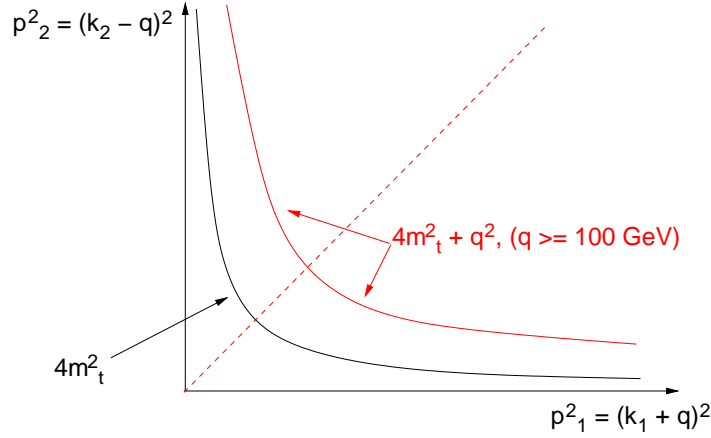


Figure A.2: Allowed region in the phase space. If no lower limit is applied to the momentum transfer ($q^2 = (0 \text{ GeV})^2$), the allowed region is situated on the right of the black hyperbola. For the case $q^2 \geq (100 \text{ GeV})^2$ the allowed region in the phase space is situated on the right of the red hyperbola.

A lower limit for the momentum transfer q (in this case $q^2 \geq (100 \text{ GeV})^2$) leads to a shift of the hyperbola to the right ($4m_t^2 \rightarrow 4m_t^2 + q^2$), as illustrated in Figure A.2. Thus, the phase space between the black and the red hyperbola is discarded completely by the CKIN 100-cut and as a consequence, the phase space for the production of the $t\bar{t}$ events becomes smaller.

The reduction depends on the value chosen for the momentum transfer q . The larger q the smaller is the remaining phase space for the generation of the fully hadronic $t\bar{t}$ events. Consequently, a sample generated with $q \geq 10 \text{ GeV}$ has a cross section which is at about factor 2 larger than for the $t\bar{t}$ events generated with $q \geq 100 \text{ GeV}$ [13].

Nevertheless, the reduction of the phase space and the resulting smaller cross section do not influence the characteristics of the produced events, as it is obvious from Figures A.3 and A.4.

In this regard Figure A.3 shows the number of reconstructed jets and the transverse momentum of the jets for an ATLFAST $t\bar{t}$ sample generated with CKIN 100 ($q^2 \geq (100 \text{ GeV})^2$) and for a sample generated with CKIN 10 ($q^2 \geq (10 \text{ GeV})^2$). Apart from the fact that the CKIN 10 sample (illustrated in brown) prevails a slightly larger number of soft jets than the CKIN 100 sample, the distributions agree well

²For this equation the limiting case $E_k = m_t$ was assumed, i.e. t -production at threshold.

in shape. The difference in the height of the distributions is due to the different production cross section, caused by the limitation of the phase space.

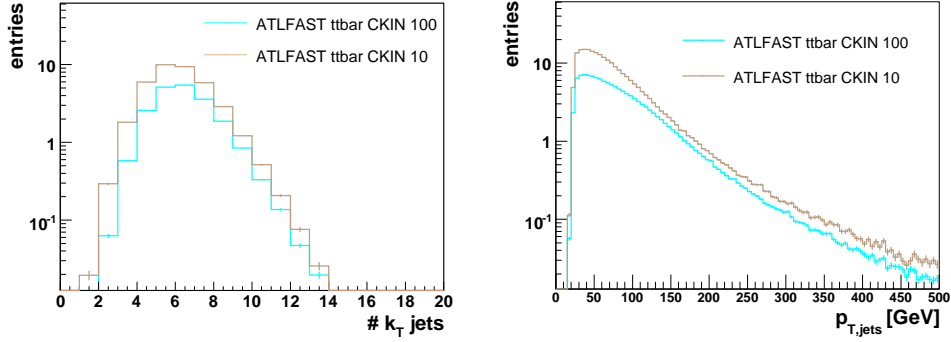


Figure A.3: Number of jets within $|\eta| < 3$ (left) and transverse momentum of the jets (right) for ATLFast $t\bar{t}$ samples generated with $q^2 \geq (10 \text{ GeV})^2$ (brown) and $q^2 \geq (100 \text{ GeV})^2$ (light blue).

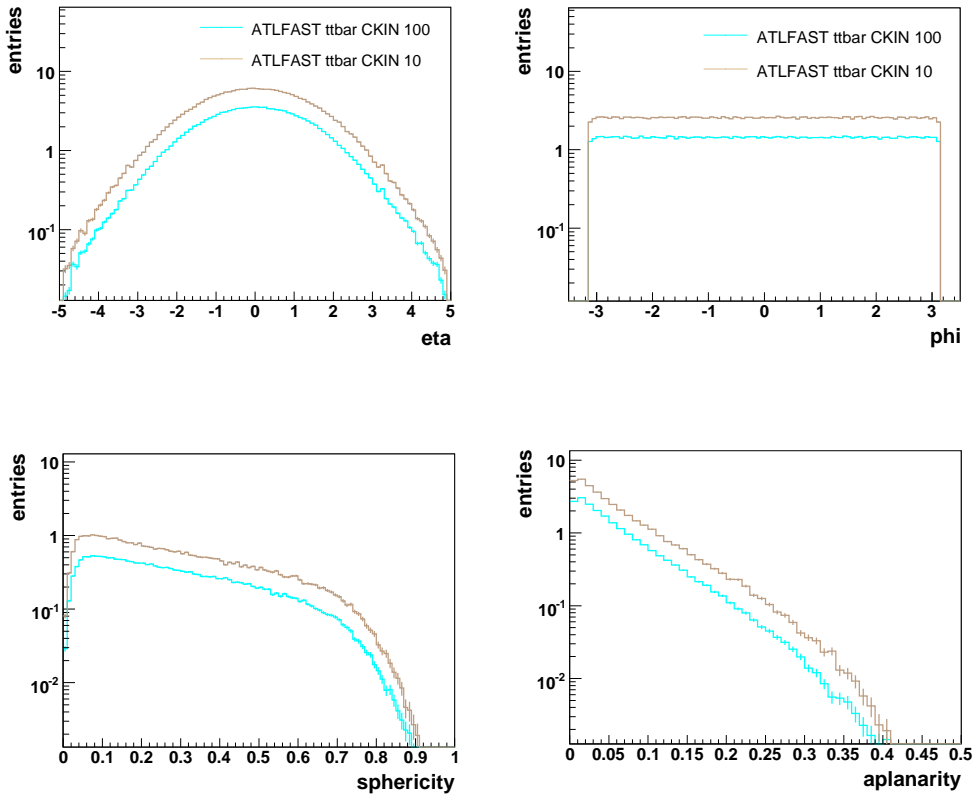


Figure A.4: Distributions for ATLFast $t\bar{t}$ samples with $q^2 \geq (10 \text{ GeV})^2$ and $q^2 \geq (100 \text{ GeV})^2$. Top left: η of the jets. Top right: ϕ of the jets. Bottom left: Sphericity. Bottom right: Aplanarity. The CKIN 10 sample is illustrated in brown, the CKIN 100 sample is shown in light blue.

Figure A.4 shows the η and ϕ distributions of the jets in the generated $t\bar{t}$ events. Illustrated in brown is the CKIN 10 sample, the light blue line shows the CKIN 100 sample. Besides, Figure A.4 represents the distributions for the sphericity and the aplanarity. All distributions for CKIN 10 and CKIN 100 agree very well for the shape. Hence, the larger value which was chosen for the lower limit of the momentum transfer q for the hard $2 \rightarrow 2$ reaction does not change the characteristics of the produced events, but delivers only a smaller production cross section for the generated events due to the smaller phase space available.

Appendix B

QCD multijet background events reconstructed with the Cone Algorithm

This Appendix lists the results for a jet reconstruction of QCD multijet background events with the Cone algorithm [41, 42] from calorimeter cell entries [86]. The Cone algorithm was applied in default configuration with a fixed Cone size of $R = 0.4$. It was only used as an extension to this study and was not relied on as the standard reconstruction scheme. The algorithm was not configured for the reconstruction of the studied QCD events. Thus, one may regard the following only as a supplement to the previous results for the QCD multijet events reconstructed with the k_T algorithm (Chapter 7 and 8).

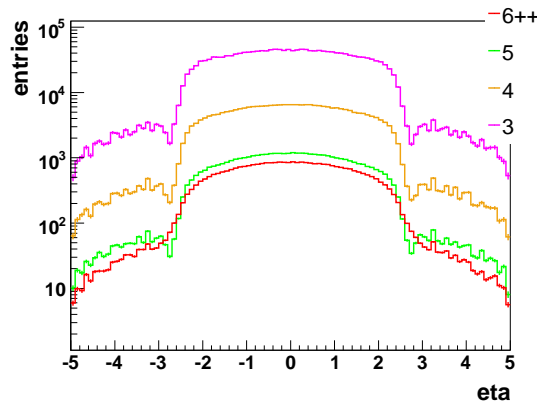


Figure B.1: η distribution for events reconstructed with a standard Cone algorithm from calorimeter cell entries.

The η distribution for those QCD events reconstructed with a standard Cone algorithm is represented in Figure B.1, also featuring additional entries for $|\eta| > 3$ as the k_T -algorithm events reconstructed from cell entries (Figure 7.8). These entries are

due to the jet-parton matching in PYTHIA 6.2 and the processing of the background events in the simulation program ATLFast.

Figure B.2 shows the ϕ distribution of the Cone algorithm events, which is in very good agreement with the results obtained from the events reconstructed with the k_T algorithm.

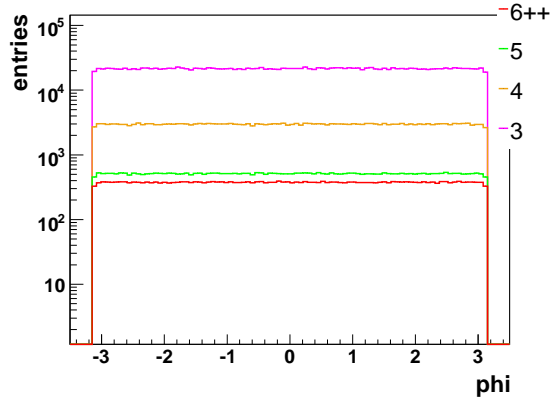


Figure B.2: ϕ distribution for QCD multijet events reconstructed with the Cone algorithm from calorimeter cells.

The number of jets reconstructed with the Cone algorithm is represented in Figure B.3. The distribution is clearly shifted to higher jet multiplicities in comparison to the distributions for the reconstruction with the k_T algorithm (see Figure 7.12).

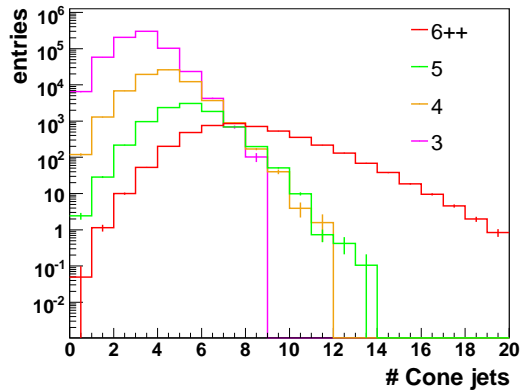


Figure B.3: Number of jets reconstructed with the Cone algorithm.

The shift occurs especially in the case of 6++ final state partons, where considerably more than 20 jets are found by the Cone algorithm. This is, amongst other reasons, due to the Cone size $R = 0.4$ chosen for this reconstruction, which has not been optimized for the jet reconstruction in QCD multijet events.

The number of identified b -jets is shown in Figure B.4. Jets reconstructed with the

Cone algorithm are slightly more often b -tagged than k_T jets (Figure 7.16), especially in the case of events with a small parton multiplicity (three and four final partons). This might be a consequence of the fact that the Cone algorithm reconstructs a generally larger number of jets in the events (see Figure B.3). For a small number of b -tagged jets the samples with lower parton multiplicity contain again much more b -jets than the samples with five or six final state partons.

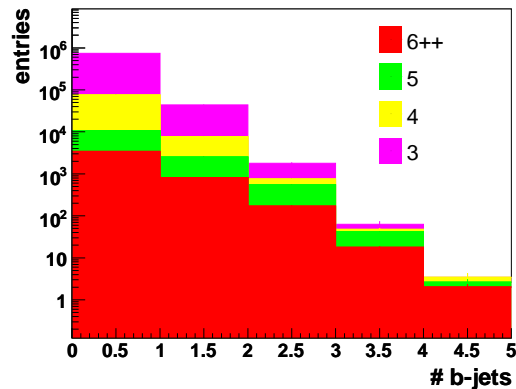


Figure B.4: Number of b -quark jets reconstructed with the Cone algorithm (stacked histogram).

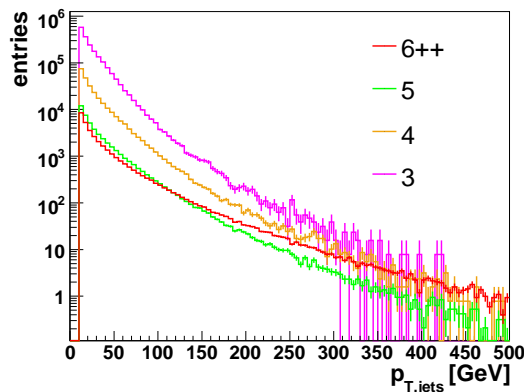


Figure B.5: Transverse momentum p_T of the jets in 3-jet, 4-jet, 5-jet and 6-jet QCD events reconstructed with the Cone algorithm.

Regarding the p_T distribution for a reconstruction with the Cone algorithm (see Figure B.5) one can state a good agreement with the jet- p_T of the k_T -algorithm events reconstructed from cells (Figure 7.10) for large transverse momenta. For small jet p_T , however, there is a deviation: The Cone Algorithm seems to reconstruct a larger number of soft jets.

The distributions for p_x , p_y and p_z of the jets, which are illustrated in Figure B.6, are narrow indicating again that more soft jets are found by the Cone algorithm.

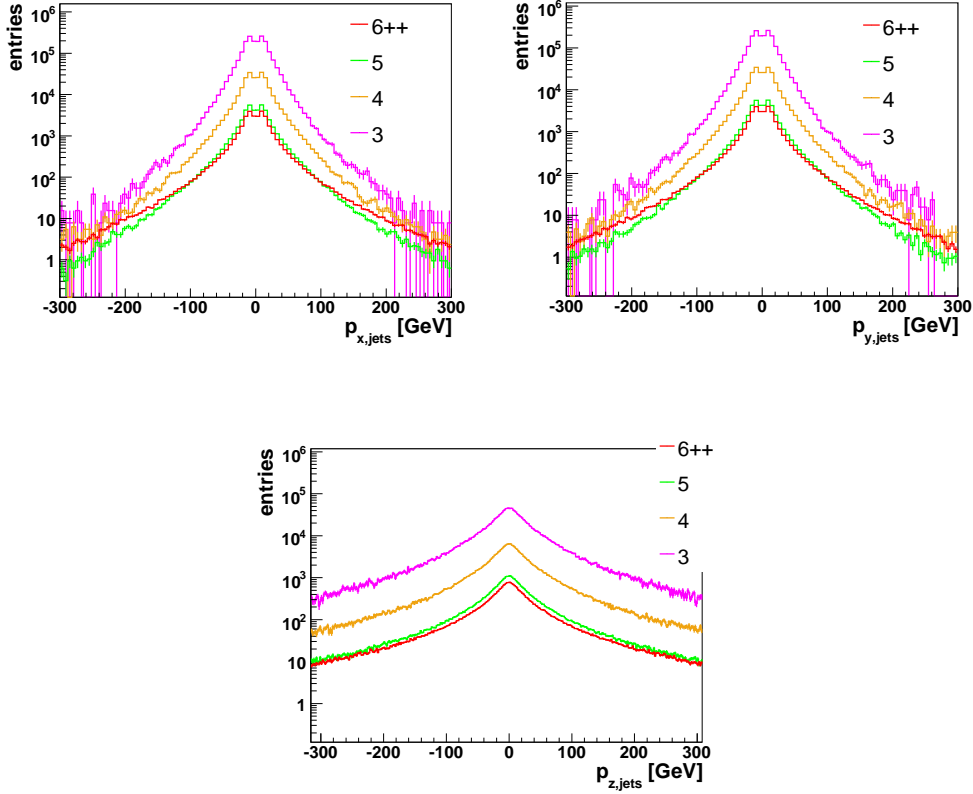


Figure B.6: Jet momenta in QCD multijet events reconstructed with the Cone algorithm. Top left: p_x . Top right: p_y . Bottom: p_z .

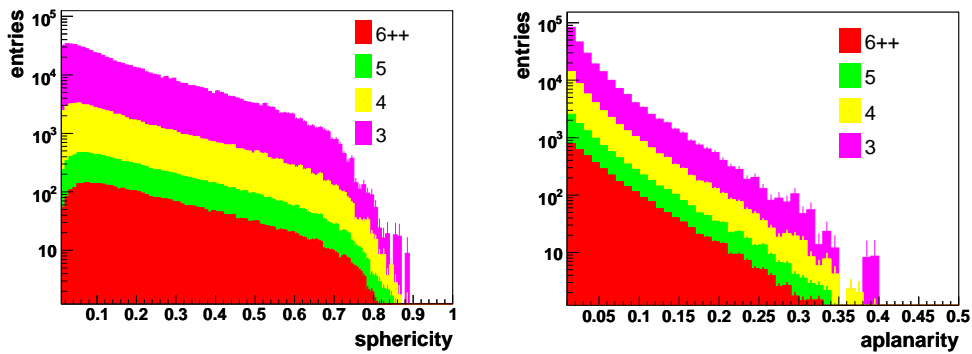


Figure B.7: Sphericity (left) and aplanarity (right) for QCD multijet events reconstructed with the Cone algorithm, illustrated by stacked histograms.

The event shapes sphericity and aplanarity are illustrated in Figure B.7. Altogether one

can say that the sphericity and aplanarity distributions slightly tend to smaller values than for the events reconstructed with the k_T algorithm (Figures 7.20 and 7.21).

Appendix C

Pulser test of ATLAS BOS-MDT muon chambers at the cosmic ray measurement facility of the LMU

C.1 Abstract

At the cosmic ray measurement facility of the Ludwig-Maximilians-University (LMU) in Munich ATLAS BOS-MDT muon chambers have been calibrated. In this context the pulser test was developed in order to test the functionality of the read-out electronics, to identify noisy channels and channels which receive no signals due to bad electrical connection.

With attenuation distributions, showing the characteristic relation between the applied attenuation and the hits counted for each mezzanine card and its channels, the amount of electronic noise as well as cross-talk between disconnected tubes and their neighbouring channels can be estimated.

C.2 Introduction

The pulser test provides a simple means to check whether all electronics channels of the muon chambers are working after mounting the electronics.

Up to 18 mezzanine cards are mounted on each chamber. Each of these cards is divided into 24 read-out channels. For the pulser test rectangular signals with amplitudes of up to 5 V are applied to the High-Voltage (HV) connector of the chamber. The signals, which are attenuated between 0 dB and 42 dB, are fed into the muon chambers on the High-Voltage side. The remaining signals are picked-up at the read-out (RO) side of the chambers and are digitized using the standard MDT read-out system [87]. The output of all (in maximum) 432 channels is monitored.

The pulser test has been developed and performed at the cosmic ray measurement facility of the LMU. It was also applied to the calibrated chambers stored in the interim storage at Eching and for the final testing of the muon chambers at CERN.

C.3 Setup of the pulser test

The setup of the pulser test is illustrated in Figure C.1. A given number of main trigger signals – created by a random generator – is sent to the HV side of the chamber. The signals pass a noise filter, which is set to eliminate interfering signals. The main trigger then initiates 5 V rectangle pulses at the pulse generator (pulser). An attenuator is applied to reduce the pulses' amplitudes by up to 42 dB. At 6 dB 50% of the input remains, at 40 dB only 0.01% of the signal amplitude is still applied to the chamber. At the read-out side of the chamber the pulses are counted and analyzed using the MDT standard read-out comprising a mezzanine card with dedicated ASD (amplifier-shaper-discriminator) chips [87].

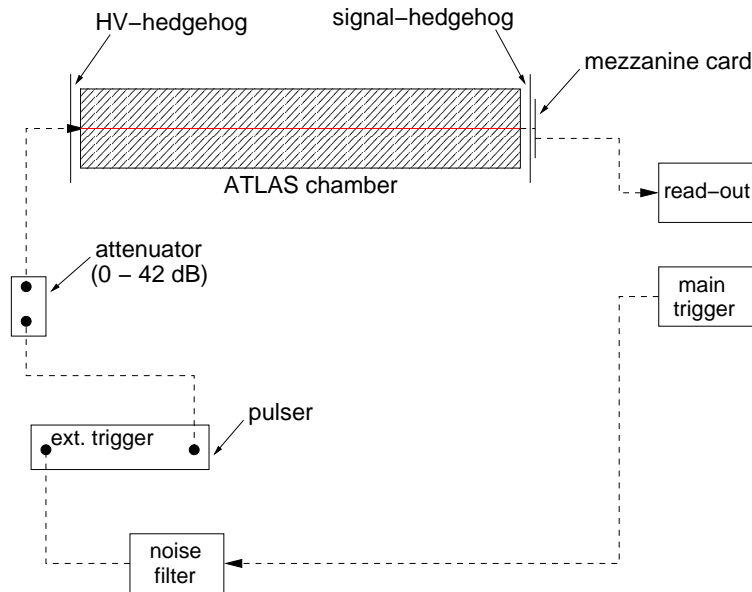


Figure C.1: Setup for the pulser test.

At the read-out side of the chamber the pulses are counted and analyzed using the MDT standard read-out comprising a mezzanine card with dedicated ASD (amplifier-shaper-discriminator) chips [87].

C.4 Measurements and results

This section presents the characteristic distributions for the applied attenuations and the number of counted pulses at the RO side of the muon chambers. Additionally, the cross-talk between neighbouring tubes as well as a pulser test on single tubes is discussed.

C.4.1 Attenuation distributions of mezzanine cards and single channels

Figure C.2 shows an attenuation distribution for mezzanine card 1 of chamber BOS_3A_02 (apin013).

Per chosen attenuation 10000 main trigger signals were generated and applied to channels of the mezzanine cards. The pulses were counted as hits by each channel. As shown in Figure C.2, the number of pulse counts (hits) remains stable up to an attenuation of about 30 dB. Above this threshold the distribution is declining quickly but does not drop to zero at once as one would expect if there were no electronic noise. At 42 dB no signal is observed anymore.

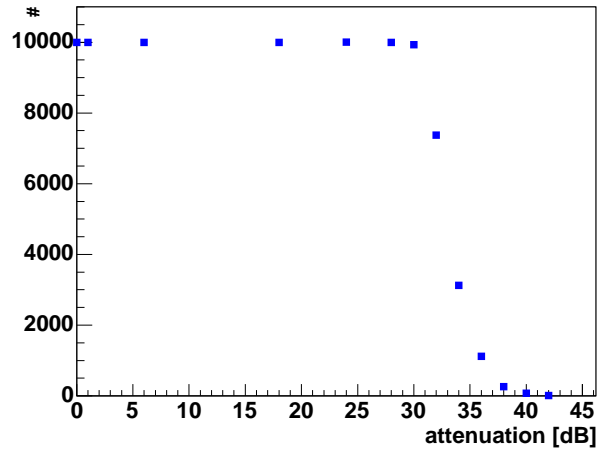


Figure C.2: Attenuation distribution for mezzanine card 1 of muon chamber BOS_3A_02.

The measured attenuation distribution of a typical channel on mezzanine card 1 is represented in Figure C.3 left. The distribution was fitted with an inverse error function and a threshold value was determined at 90% of the number of main trigger signals, which is emphasized by the red lines in Figure C.3 left.

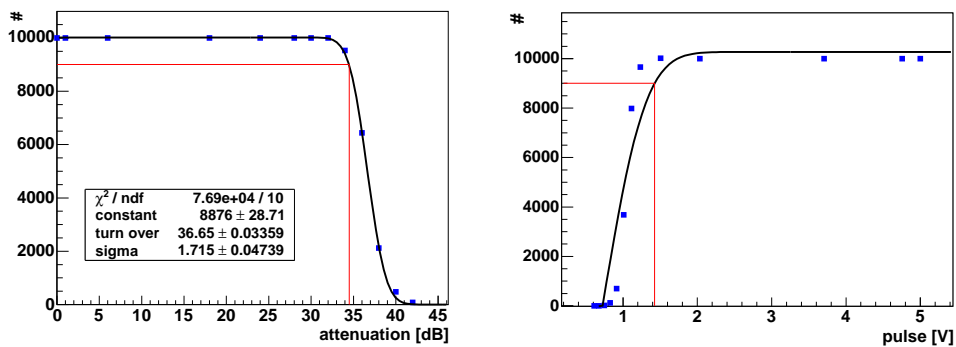


Figure C.3: Left: Attenuation for channel 1 of mezzanine card 1. The distribution was fitted with an inverse error function. The red lines mark the value of 90% of the input signal. Right: Hits versus the remaining pulse at the different attenuations. An error function was overlaid. The red vertical line indicates that the remaining signal amounts still to 90% when the incoming pulse is attenuated to 1.5 V.

For this specific channel the threshold is located at an attenuation of about 34 dB. Figure C.3 right shows the number of hits versus the level of the incoming pulse. An error function was overlaid to guide the eye.

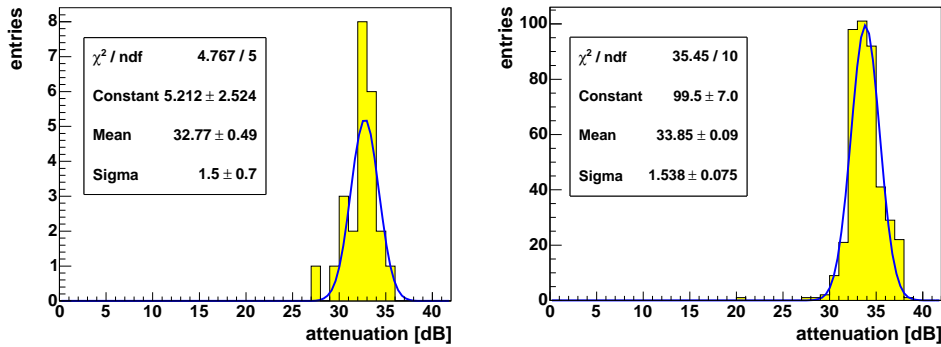


Figure C.4: Left: Attenuation distribution for all 24 channels of mezzanine card 1, chamber BOS_3A_02. Right: Attenuation distribution for all 432 channels of chamber BOS_3A_02.

The remaining channels of mezzanine card 1 show comparable threshold values, as can be seen in Figure C.4 left. All thresholds are located between 27 dB and 36 dB corresponding to the known spread of ± 6 mV of the ASD chips' internal discriminator thresholds [87, 88] according to the BMC database [89]. An attenuation distribution for all channels of chamber BOS_3A_02 is shown in Figure C.4 right.

C.4.2 Cross-talk between tubes

At the few chambers with disconnected tubes – i.e. the sense wire in the tube is electrically insulated from the read-out electronics – the cross-talk between single tubes can be studied. For this purpose the chamber was pulsed and the attenuation curve for the disconnected tube was determined, which is expected to show no signal at all.

The hit distribution at an attenuation of 0 dB for a mezzanine card with one disconnected tube is shown in Figure C.5. All channels see 10000 pulse signals, except from channel 23 which sees about 4800 pulse signals at the attenuation of 0 dB. As tube 23 is completely disconnected from High-Voltage and gas it should receive no signals at all. Consequently, the observed hits are due to cross-talk between the disconnected channel and the nearby tubes.

Figure C.6 represents the corresponding attenuation curve of the disconnected tube 23. The cross-talk between the disconnected tube and the surrounding tubes amounts to about 48% at 0 dB attenuation. The cross-talk hits already disappear at an attenuation of 6 dB. Therefore, it is negligible compared to the typical signal amplitude of 300 mV on the input to the read-out mezzanine card [87].

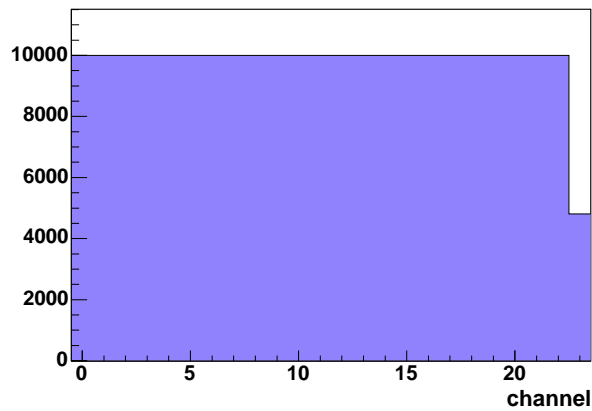


Figure C.5: Hit distribution for mezzanine card 10, chamber BOS_1C_06, at an attenuation of 0 dB. Channel 23 is disconnected.

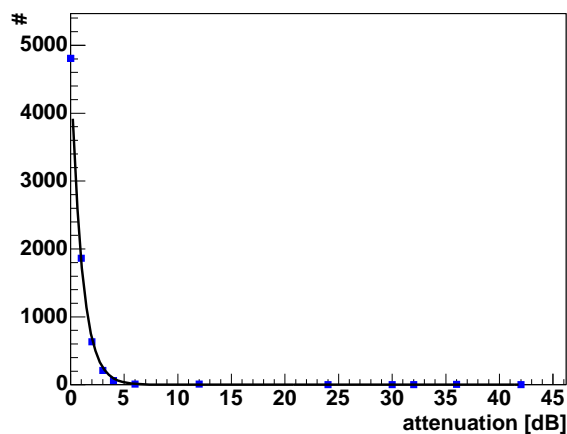


Figure C.6: Attenuation curve of the disconnected channel 23, mezzanine card 10, BOS_1C_06.

C.4.3 Pulser test on single tubes

For more detailed studies of cross-talk between tubes a pulser test on single tubes has been carried out. For this purpose the Faraday cages and the hedgehog cards at the HV side of the muon chambers have been dismantled and the pulses were sent directly to a single tube.

Figure C.7 illustrates the hit distribution for a pulser test on tube 22, mezzanine card 10 of chamber BOS_1C_06 at an attenuation of 6 dB. In contrast to the pulser test of the complete chamber BOS_1C_06, where the observed cross-talk between the tubes disappears at an attenuation of 6 dB (see Figure C.6), one can observe a lot of cross-

talk at 6 dB and even beyond, as shown in Figure C.8. Especially the tubes 13 to 15 and tube 6 show much cross-talk (see Figure C.7).

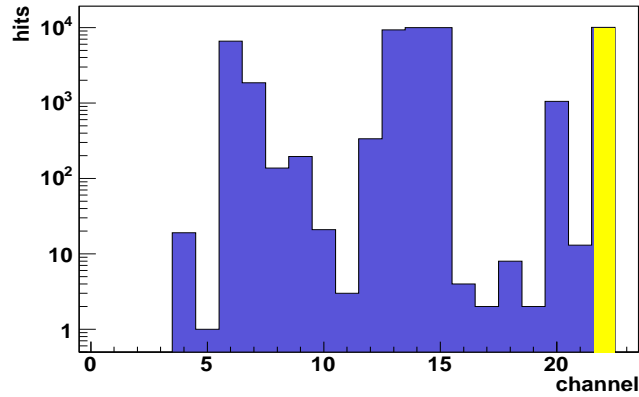


Figure C.7: Hit distribution for a pulser test on single tube (tube 22) on mezzanine card 10, chamber BOS_1C_06, at 6 dB.

The reason for this is apparent looking at the tubes' channel map, shown in Figure C.9. As tube 22 is pulsed, above all the nearby tubes (especially tube 14 and tube 15) receive a lot of signals. The nearby tube 23 shows no signal as the tube is disconnected. The signal is relayed to channel 13 as well as to channel 6 and 7. The reason for the increased cross-talk to the neighbouring tubes – in comparison to the pulser test of a complete chamber – is that the tubes themselves are less grounded due to the removal of the Faraday cages and hedgehog cards.

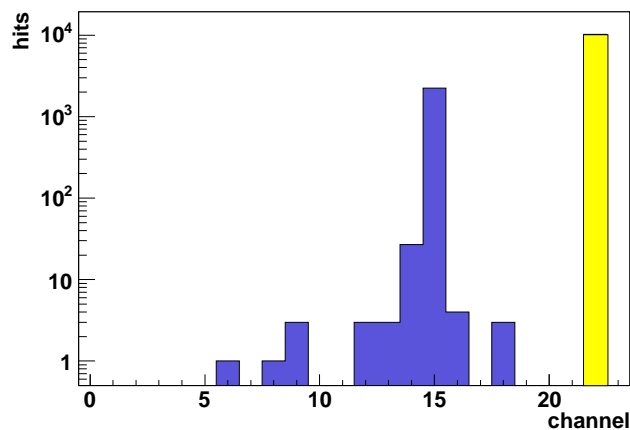


Figure C.8: Hit distribution for a pulser test on single tube (tube 22) on mezzanine card 10, chamber BOS_1C_06, at 16 dB.

The signals are then relayed from one tube to another by capacitive coupling, where maximum capacitive coupling occurs for spatially neighbouring channels, as illustrated by the channel map (Figure C.9). This leads, hence, to the large cross-talk of channels 14, 15 and 20.

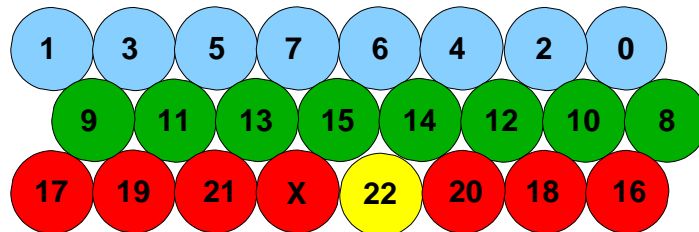


Figure C.9: Map of channels for C-type chambers, lower multi-layer.

The equivalent network for capacitive coupling between neighbouring tubes is shown in Figure C.10. Ideally, the neighbouring tubes are completely decoupled by a vanishing grounding resistance. If the Faraday cages and hedgehog cards are removed, however, the grounding resistance increases as the grounding is provided at the opposite side of the tubes by the read-out electronics only, and the signals are relayed from one tube to another.

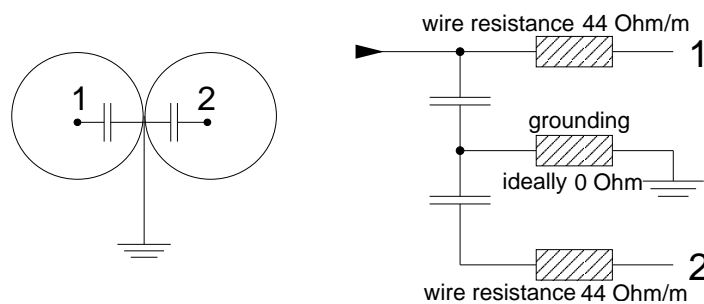


Figure C.10: Capacitive coupling between two neighbouring tubes.

In order to check if the added transmission of signals is indeed caused by the lower grounding of the tubes, the ground pins of the tubes in layer two, i.e. the layer containing among others the tubes 14 and 15, have been connected with each other by a wire and have finally been connected with ground.

The resulting hit distribution of the pulser test on tube 22 is shown in Figure C.11. With this additional ground connection tube 14 and 15 show no signal any more at an attenuation of 6 dB. Only tube 6 and 20, which do not belong to layer two and which have not been supplementary grounded, still show cross-talk at 6 dB. At an attenuation of 12 dB the cross-talk has almost disappeared as can be seen in Figure C.11 below.

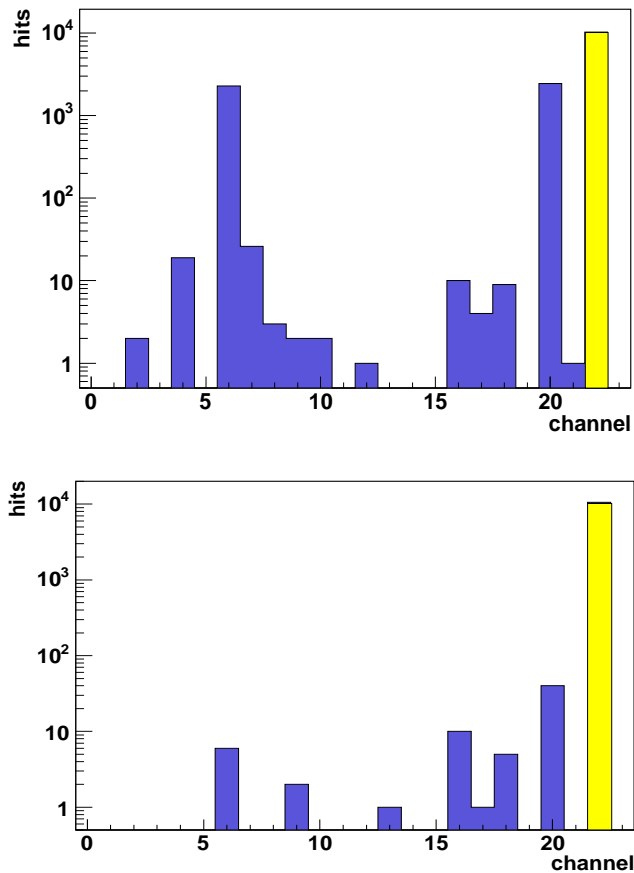


Figure C.11: Top: Hit distribution for pulser test on single tube (tube 22), on mezzanine card 10, chamber BOS_1C_06, at 6 dB. The tubes are additionally grounded. Bottom: Hit distribution for pulser test on single tube (tube 22), on mezzanine card 10, chamber BOS_1C_06, at 12 dB and additional grounding.

Thus, the pulser test on single tubes proves that bad grounding leads to large cross-talk between the tubes. The standard grounding schema (restored by the pulser test on single tubes with the additional grounding), however, guarantees minimum cross-talk. Consequently, the pulser test on a single tube is comparable to the pulser test of a complete chamber, if the grounding of the tubes is ensured after removing the Faraday cages and the hedgehog cards.

C.4.4 Comparison between pulser test at chambers in the cosmic ray measurement facility and in the preparation room

There is a difference between the pulser test of a chamber in the cosmic ray measurement facility and a chamber in the preparation room, where the electronics is mounted to the chambers.

Due to the additional grounding of chambers in the cosmic ray measurement facil-

ity the cross-talk between disconnected tubes and their neighbouring tubes is slightly smaller than in the preparation room, as one can see in Figure C.12.

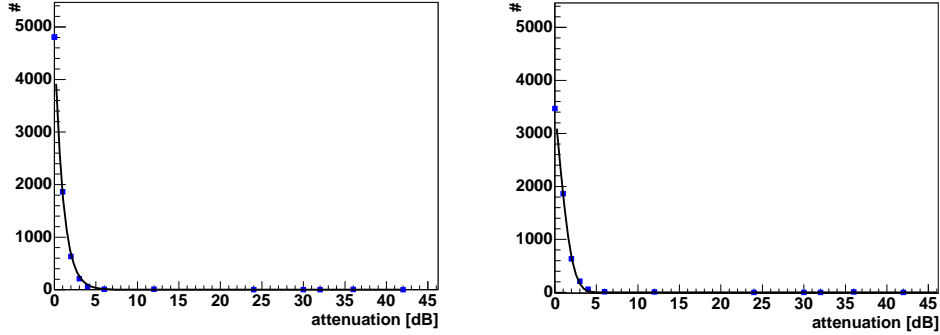


Figure C.12: Left: Attenuation curve for disconnected channel 23 in the preparation room - the cross-talk at 0 dB amounts to about 48%. Right: Attenuation for channel 23 while the chamber is in the cosmic ray facility. With the additional grounding the cross-talk mounts only up to 37% of the input signal at 0 dB attenuation.

While the cross-talk is about 48% for the chamber in the preparation room (Figure C.12 left), the chamber in the cosmic ray facility shows only 37% cross-talk at 0 dB attenuation (Figure C.12 right). Nevertheless, the characteristics of the attenuation curves remain the same in both cases and the cross-talk disappears at an attenuation of about 6 dB both in the cosmic ray measurement facility and in the preparation room.

C.5 Comparison to simulation

The height of the output pulses at the RO side of the muon chambers was simulated by Fast Fourier analysis of the periodic pulse, applying a simplified equivalent network as a voltage divider and synthesizing the output signal. The corresponding equivalent network for the calculation is shown in Figure C.13.

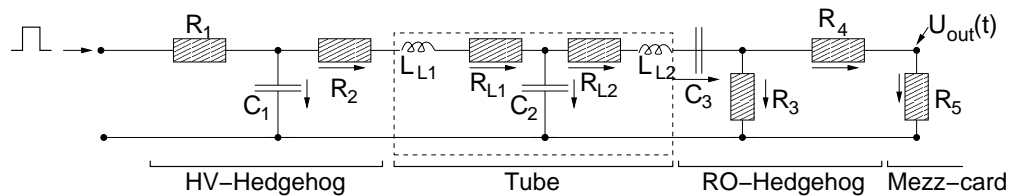


Figure C.13: Simplified equivalent network for the pulser test of an ATLAS muon chamber. $R_1 = 1 \text{ M}\Omega$, $R_2 = 383 \text{ }\Omega$, $R_3 = 10 \text{ k}\Omega$, $R_4 = 10 \text{ }\Omega$, $R_5 = 240 \text{ }\Omega$, $R_{L1} = R_{L2} = \frac{1}{2} \cdot 44 \frac{\Omega}{\text{m}} \cdot 3.75 \text{ m}$, $L_{L1} = L_{L2} = \frac{1}{2} \cdot 5.12 \text{ }\mu\text{H}$, $C_1 = 470 \text{ pF}$, $C_2 = 8.7 \frac{\text{pF}}{\text{m}} \cdot 3.75 \text{ m}$ and $C_3 = 470 \text{ pF}$. $R_5 = 240 \text{ }\Omega$ effects that the mezzanine cards use a differential read-out of $U(t)$ with $120 \text{ }\Omega$ input impedance per line.

For the simulation of the mezzanine card the preamplifier and the shaper stages of the ASD chip (see Figure C.14) were represented by frequency-dependent phase-shift and gain [87, 90], as indicated in Figures C.16, C.17 and C.18.

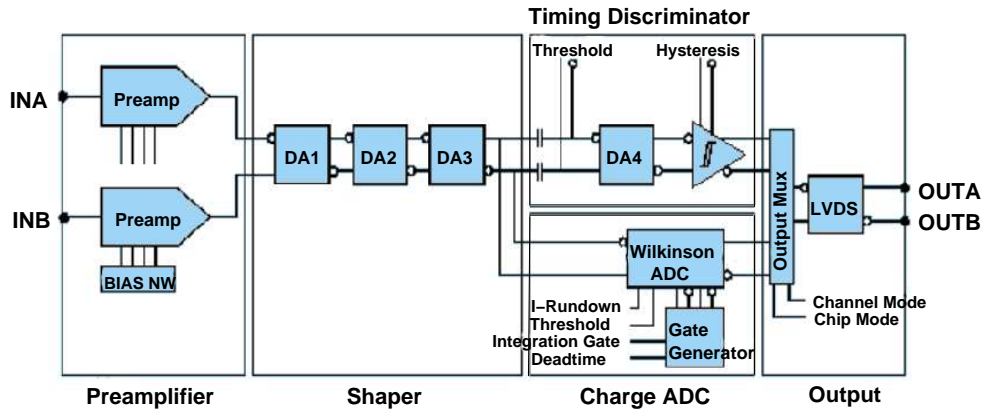


Figure C.14: MDT-ASD channel block diagram [87]. The signal flow calculation includes the preamplifier and shaper stages DA1 - DA4.

An input pulse of 5 V for tubes with a length of 3.75 m, a diameter of 3.0 cm and wire diameter of $50\ \mu\text{m}$ therefore leads to a diminished pulse of about 210 mV at maximum at the RO side of the chamber (i.e. pins INA and INB in Figure C.14), as shown in Figure C.15. This resulting pulse at the input to the discriminator stage DA4 of the ASD chip (see Figure C.14) is finally compared with the internal threshold value [87] of 38 mV, which is indicated by the red line in Figure C.15. If the incoming signal exceeds this internal threshold an output pulse is recorded.

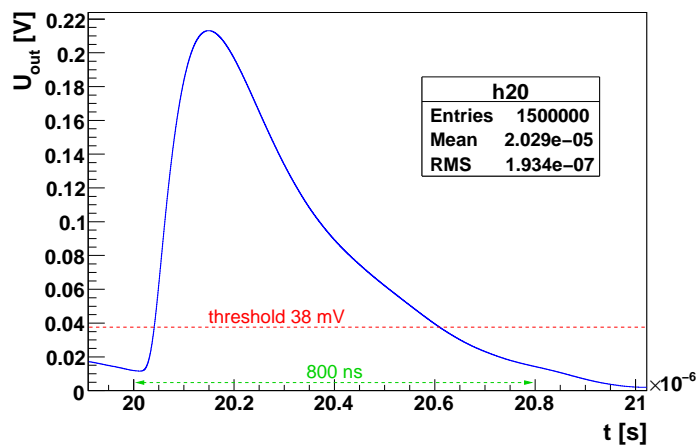


Figure C.15: Voltage at the input to DA4 of the ASD chip on the mezzanine card of a muon chamber for $U_0 = 5\ \text{V}$.

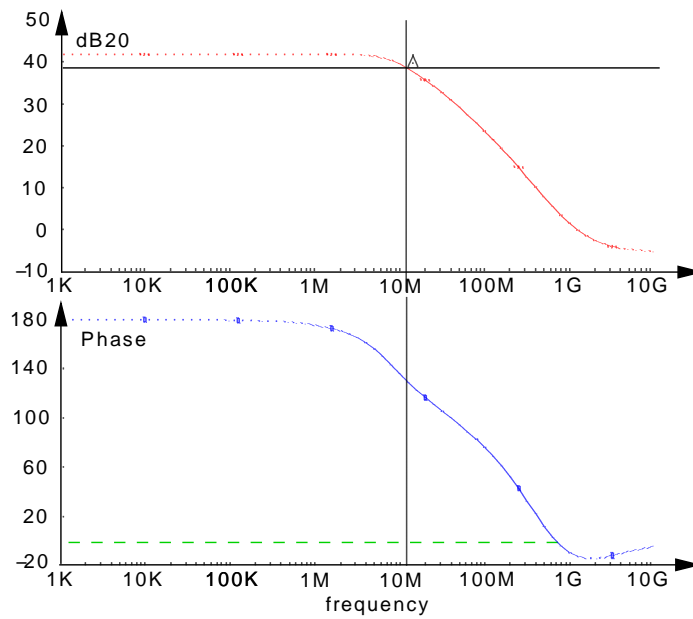


Figure C.16: Preampifier frequency response [87]. A small signal gain is observed at 41.75 dB. The initial phase shift of 180° decreases to zero at 700 MHz (green line) [87].

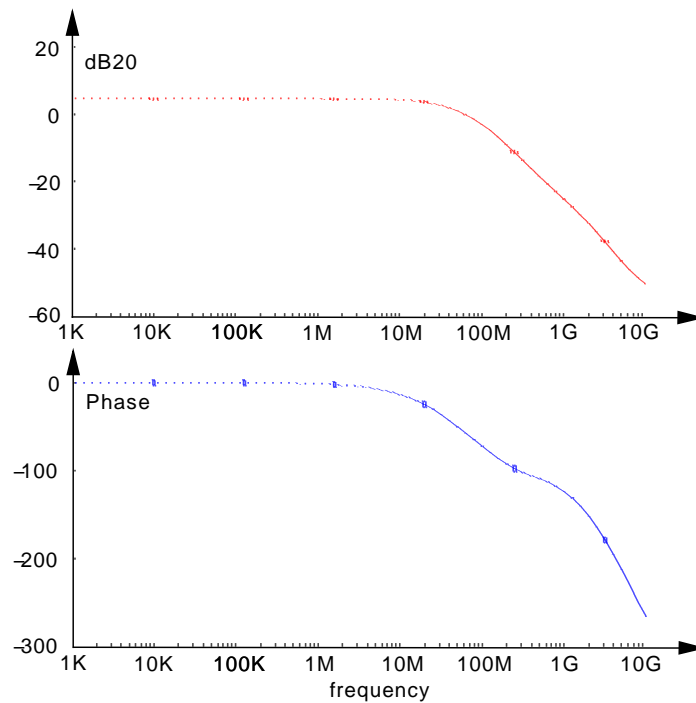


Figure C.17: Differential amplifier DA1 frequency response [87]. The small signal gain is 4.5 dB. The initial phase shift of 0° decreases to -180° at 3 GHz [87].

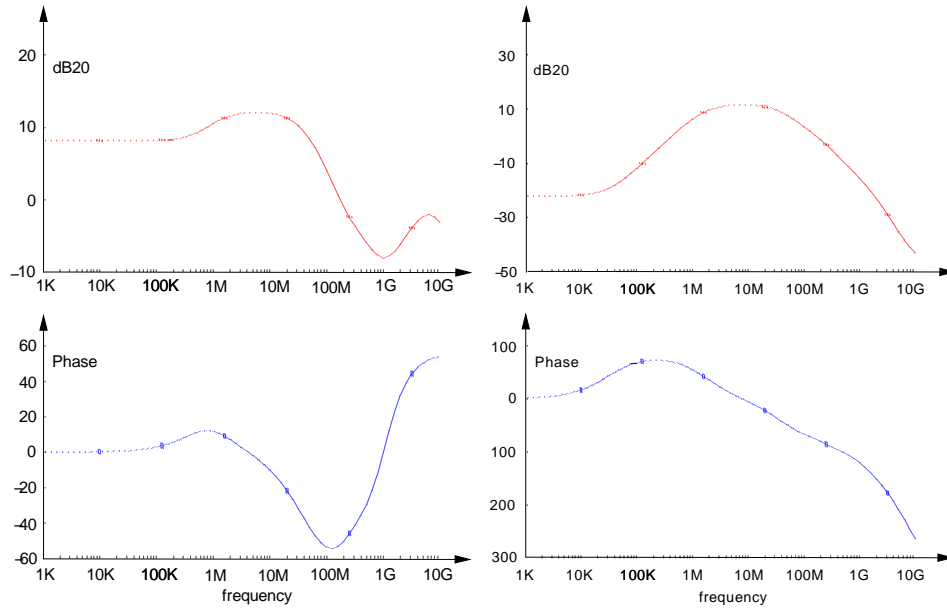


Figure C.18: DA2 AC characteristics (left) and DA3 AC characteristics (right) [87]. The voltage gain peaks for 11 dB at 5 – 10 MHz (left) and for 10 dB at 5 – 10 MHz (right), respectively [87].

The relation between the output signal U_{out} and the applied attenuation is shown in Figure C.19. For an internal threshold of 38 mV (illustrated by the red lines) the signal fails to exceed the threshold at an attenuation of 15 dB which is not in perfect agreement with the estimated threshold values for the muon chambers of 27 – 36 dB, shown by Figure C.4.

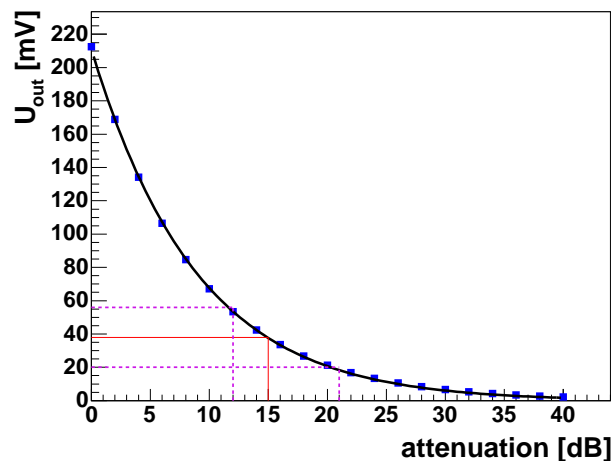


Figure C.19: Relation between the maximum output voltage U_{out} and the applied attenuation. The signal exceeds the internal threshold of 38 mV up to an attenuation of about 15 dB (indicated by the red lines). Considering the internal offset of the channels and the corresponding errors the internal threshold amounts to only 20 mV (for –18 mV in maximum, corresponding to the lower magenta lines) or to 56 mV (for +18 mV in maximum, corresponding to the upper magenta lines). In this case the threshold is crossed at attenuations of up to 21 dB or to 12 dB, respectively.

However, considering in addition the channels' internal offset [89] of up to ± 12 mV and the corresponding errors of ± 6 mV, the signal is recorded up to an attenuation of about 21 dB in maximum (-18 mV \rightarrow internal threshold of 20 mV) or to 12 dB in minimum ($+18$ mV \rightarrow internal threshold of 56 mV). This range from 12 – 21 dB reasonably corresponds to the range of 27 dB to 36 dB, found by the measurement.

A reason for the deviation from the measured values might be – apart from errors in measurement – due to the simplified description of the equivalent network of the pulser test which of course cannot cover all details of the true signal line. Especially the documented input resistance R_5 (see Figure C.13) is considered as a pure ohmic resistance of $2 \cdot 120 \Omega$ for the DC characteristics of the equivalent network. It should, however, also include the true AC input impedance of the unfolded cascode preamplifiers [87] which might be larger next to the DC working point [91].

C.6 Summary and conclusion

The pulser test is a useful tool to probe the read-out electronics with simple means. Disconnected tubes as well as defective hedgehog or mezzanine cards can easily be identified.

An attenuator is used to apply any attenuations between 0 dB and 42 dB at the 5 V pulse and therefore, to attenuate the incoming signals which are then counted and analyzed at the RO side of the chamber.

For an attenuation of 0 dB the observed cross-talk between two channels amounts to 48% if the pulser test is carried out in the preparation room, while the chambers in the cosmic ray measurement facility are additionally grounded and thus, show a lower cross-talk of only 37%. In both cases the cross-talk between disconnected tubes and their neighbouring tubes can be neglected if adequate grounding is ensured. The pulser test on single tubes confirms this conclusion on the additional grounding of the tubes. Using an approximate four-pole calculation the equivalent network and the output signals of the pulser test have been simulated by means of Fast Fourier transformation. The results of the simulation reasonably correspond with the measurements – considering the channels' internal offset and the corresponding errors as well as possible errors in the description of the equivalent network.

List of Figures

2.1	Fundamental interaction Feynman diagrams of the QCD	6
2.2	Running of the strong coupling constant α_s	7
2.3	Hadronization of quarks and gluons	8
2.4	Cluster model of hadronization	9
2.5	String model of hadronization	9
2.6	Composition of the proton	10
2.7	The structure function	10
2.8	Illustration of the parton density function	11
2.9	Gluon distribution at different Q^2	12
2.10	Feynman diagrams for the $t\bar{t}$ production	13
2.11	Additional Feynman diagram for the $t\bar{t}$ production at the Tevatron. . .	13
2.12	Branching fractions of the $t\bar{t}$ decay	14
2.13	Feynman diagram for the fully hadronic $t\bar{t}$ decay	15
3.1	Schematic overview of the LHC	18
3.2	The ATLAS detector	19
3.3	The ATLAS muon spectrometer	20
3.4	ATLAS electromagnetic and hadronic calorimeter	21
4.1	Illustration of QCD multijet background events	24
4.2	W/Z production with additional jets.	25
5.1	Schematic drawing of a $t\bar{t}$ event	29
5.2	pp scattering in different phases.	30
5.3	Block diagram: Jet reconstruction steps of the exclusive mode of the k_T algorithm	34
5.4	Comparison between k_T and Cone Algorithm I	35
5.5	Comparison between k_T and Cone Algorithm II	35
5.6	Illustration of an arbitrary merging of cones by the Cone algorithm. Infrared divergences	36
5.7	Collinear divergences in the jet reconstruction with the Cone algorithm	36
6.1	Comparison between "own" b -quark events and b -quark events generated with the ALPGEN $Q\bar{Q}+4$ jets mode	40
6.2	p_T distribution for own b -quark events divided by the distribution for the ALPGEN $Q\bar{Q}+4$ jets mode b -quark events	41
6.3	Number of offers in inclusive QCD 6-jet events	44

6.4	Feynman diagram of a fully hadronic $t\bar{t}$ event	45
6.5	Illustration of the differences between LO and NLO	47
6.6	Example of a Feynman diagram for a QCD six-jets background event	48
6.7	Concept of the Athena Framework	50
7.1	Number of offers in inclusive and exclusive QCD 6-jet events and Number of reconstructed jets in an inclusive and an exclusive 6-jet background sample	55
7.2	Distributions for modified routine UPVETO and for the standard set- ting of UPVETO I	56
7.3	Distributions for modified routine UPVETO and for the standard set- ting of UPVETO II	56
7.4	Jet multiplicity and sphericity distribution for an (exclusive) 5-jet sam- ple for modified and standard UPVETO	57
7.5	d_{Cut} determination for jet reconstruction from calorimeter cells and charged particle tracks for fully hadronic $t\bar{t}$ events	58
7.6	Comparison of d_{Cut} values for $t\bar{t}$ and 6-jet background events for a jet reconstruction from cell entries and charged particle tracks	59
7.7	ϕ distributions of the jets in $t\bar{t}$ and QCD background events for a re- construction from cells	62
7.8	η distribution of the jets in $t\bar{t}$ and QCD background events for a recon- struction from cell entries	62
7.9	η distribution of the jets in $t\bar{t}$ and QCD background events for a recon- struction from tracks	63
7.10	Transverse momenta of the jets in $t\bar{t}$ and QCD background events for cells	63
7.11	Transverse momenta of the jets in $t\bar{t}$ and QCD background events for tracks	64
7.12	Number of reconstructed jets in $t\bar{t}$ and QCD background events for cells	64
7.13	Number of reconstructed jets in $t\bar{t}$ and QCD background events for tracks	65
7.14	η versus the number of reconstructed jets fully hadronic $t\bar{t}$ events re- constructed from cell entries	65
7.15	η versus the number of reconstructed jets for QCD background events reconstructed from cell entries	66
7.16	Number of b -tagged jets in $t\bar{t}$ and QCD background events (cells)	66
7.17	η versus the number of b -tagged jets for $t\bar{t}$ events reconstructed from cells	67
7.18	η versus the number of b -tagged jets for QCD background events re- constructed from cells	68
7.19	Number of hadrons in $t\bar{t}$ and background events	68
7.20	Sphericity in events reconstructed from calorimeter cells and charged particle tracks	69
7.21	Aplanarity in events reconstructed from cells and tracks	69
7.22	ϕ and η of the jets in $t\bar{t}$ events from full and fast simulation	70
7.23	Transverse momenta of the jets and number of jets in $t\bar{t}$ events from full and fast simulation	71

7.24	η versus the number of reconstructed jets in fast and fully simulated fully hadronic $t\bar{t}$ events	72
7.25	Number of b -tagged jets in $t\bar{t}$ events from full simulation and fast simulation	72
7.26	η versus the number of b -jets in fast and fully simulated fully hadronic $t\bar{t}$ events	73
7.27	Sphericity in fast and fully simulated $t\bar{t}$ events	73
7.28	d_{Cut} determination for $t\bar{t}$ events on generator level	74
7.29	Number of multiple events in $t\bar{t}$ multijet events	76
7.30	Jet multiplicity in $t\bar{t}$ and 6-jet background events with and without pile-up.	76
7.31	Lego plot of a fully hadronic $t\bar{t}$ event with and without pile-up events	77
7.32	p_T of hadrons and pseudorapidity η of jets for $t\bar{t}$ events with and without pile-up.	77
7.33	p_T of hadrons and pseudorapidity η of jets for 6-jet background events with and without pile-up.	78
7.34	Jet multiplicity in $t\bar{t}$ events with and without pile-up after applying the cuts.	78
7.35	Transverse momentum of the jets in $t\bar{t}$ events with and without pile-up	79
7.36	Number of hadrons in $t\bar{t}$ events with and without pile-up	80
7.37	Jet multiplicity and transverse momenta of hadrons in $t\bar{t}$ pile-up events obtained from own settings and reproduced with settings in [80]	81
8.1	Comparison between the sphericity of fully hadronic $t\bar{t}$ and 6-jet events at the Tevatron and at the LHC.	84
8.2	Comparison between the aplanarity of fully hadronic $t\bar{t}$ and 6-jet events at the Tevatron and at the LHC.	84
8.3	Number of reconstructed jets with first cut on the pseudorapidity	85
8.4	Transverse momenta of the six chosen jets in the event (cells)	86
8.5	Transverse momenta of the six chosen jets in the event (tracks)	87
8.6	Sum of the six jets' p_T for events reconstructed from cells and tracks	88
8.7	Invariant dijet masses for calorimeter cell events	90
8.8	Invariant trijet masses for calorimeter cell and charged particle track events	91
8.9	Scalar jet- p_T sum for the 3-jet combinations forming the top quarks in the event: Calorimeter cell events	92
8.10	Scalar jet- p_T sum for the 3-jet combinations forming the top quarks in the event: Charged particle track events	92
8.11	Sketch of an event with maximal sphericity and aplanarity ($S = 1$ and $A = \frac{1}{2}$).	93
8.12	Event shapes for calorimeter cell events	94
8.13	Event shapes for charged particle track events	95
8.14	Cut-Flow histogram for events reconstructed from cell entries and particle tracks	96
8.15	Number of b -tagged jets in calorimeter and track events	98
8.16	Cut-Flow histogram for events reconstructed from cell entries and particle tracks	99

8.17	Number of permutations for $t\bar{t}$ and background events	102
8.18	Reconstructed masses of the two top quarks after the cut on the number and the pseudorapidity of the jets	103
8.19	$\Delta p_{z,top}$ in $t\bar{t}$ and QCD 6-jet background events	104
8.20	Reconstructed masses of the two top quarks after the $p_{T,jets}$ cuts and the $\Delta p_{z,top}$ cut	104
8.21	Sum of the transverse momenta of the six chosen jets	105
8.22	Reconstructed dijet masses for $t\bar{t}$ and background events	105
8.23	Aplanarity distribution for fully hadronic $t\bar{t}$ events and the residual background events	106
8.24	Reconstructed masses of the two top quarks after the cut on the aplanarity	106
8.25	Reconstructed masses of the two top quarks after the cut on the aplanarity	107
8.26	Reconstructed masses of the two top quarks after cutting $m_{trijet} < 400$ GeV	107
8.27	Cut-flow histogram for PYTHIA $t\bar{t}$ and QCD multijet background events	109
8.28	Added distributions for the remaining $t\bar{t}$ and 6-jet background events, presenting the two reconstructed top quark masses I	111
8.29	Added distributions for the remaining $t\bar{t}$ and 6-jet background events, presenting the two reconstructed top quark masses II	111
8.30	$\frac{\Delta S}{S} \sim \frac{\Delta \sigma_{ii}}{\sigma_{ii}}$ for fully hadronic $t\bar{t}$ events at different integrated luminosities	112
A.1	Illustration of the hard $2 \rightarrow 2$ process for the production of a pair of top quarks	117
A.2	Limitation of the phase space for $q \geq 100$ GeV	118
A.3	Number of jets and transverse momentum of the jets for ATLFAS $t\bar{t}$ samples, generated with $q^2 \geq (10 \text{ GeV})^2$ and $q^2 \geq (100 \text{ GeV})^2$	119
A.4	Distributions for ATLFAS $t\bar{t}$ samples with $q^2 \geq (10 \text{ GeV})^2$ and $q^2 \geq (100 \text{ GeV})^2$	119
B.1	η distribution for events reconstructed with a standard Cone algorithm from calorimeter cell entries.	121
B.2	ϕ distribution for QCD multijet events reconstructed with the Cone algorithm from calorimeter cells.	122
B.3	Number of jets reconstructed with the Cone algorithm.	122
B.4	Number of b -quark jets reconstructed with the Cone algorithm (stacked histogram).	123
B.5	Transverse momentum p_T of the jets in 3-jet, 4-jet, 5-jet and 6-jet QCD events reconstructed with the Cone algorithm.	123
B.6	Jet momenta in QCD multijet events reconstructed with the Cone algorithm. Top left: p_x . Top right: p_y . Bottom: p_z	124
B.7	Sphericity (left) and aplanarity (right) for QCD multijet events reconstructed with the Cone algorithm, illustrated by stacked histograms.	124
C.1	Setup for the pulser test.	128
C.2	Attenuation distribution for mezzanine card 1 of muon chamber BOS_3A_02.	129

C.3	Attenuation distribution for channel 1 of mezzanine card 1 and the corresponding hit distribution.	129
C.4	Attenuation distribution of chamber BOS_3A_02	130
C.5	Hit distribution for mezzanine card 10, chamber BOS_1C_06 (apin047), at an attenuation of 0 dB	131
C.6	Attenuation curve of the disconnected channel 23, mezzanine card 10, BOS_1C_06.	131
C.7	Hit distribution for a pulser test on single tube at 6 dB	132
C.8	Hit distribution for a pulser test on single tube at 16 dB	132
C.9	Map of channels for C-type chambers, lower multi-layer	133
C.10	Capacitive coupling between two neighbouring tubes.	133
C.11	Hit distribution for pulser test on single tube with additional grounding	134
C.12	Attenuation curve for disconnected channel 23 in preparation room and cosmic ray facility	135
C.13	Simplified equivalent network for pulser test of an ATLAS muon chamber	135
C.14	MDT-ASD channel block diagram	136
C.15	Voltage at the input to DA4 of the ASD chip on the mezzanine card of a muon chamber for $U_0 = 5$ V.	136
C.16	Preamplifier frequency response	137
C.17	Differential amplifier DA1 frequency response	137
C.18	DA2 AC characteristics and DA3 AC characteristics	138
C.19	Relation between the maximum output voltage and the applied attenuation	138

List of Tables

2.1	The three particle generations in the Standard Model	4
2.2	Interactions in the Standard Model of elementary particle physics . . .	4
2.3	States of the colour-octet	5
4.1	Different final states in W/Z pair production processes	26
4.2	Branching fractions for the hadronic decay of the τ lepton	27
6.1	Hard $2 \rightarrow 2$ processes available in the N Jets option	40
6.2	Choice of factorization and renormalization scale for the N Jets code .	42
6.3	Input variables for the generation of a weighted six-jet sample.	43
6.4	Switches for the simulation of $t\bar{t}$ multijet events with PYTHIA	46
6.5	General switches for the configuration of PYTHIA	46
6.6	Settings for processing ALPGEN background events in PYTHIA	49
6.7	Standard implementation of the k_T algorithm in PYTHIA 6.2 stand- alone and ATLAS software	53
7.1	Number of available fully hadronic $t\bar{t}$ events	60
7.2	Number of generated QCD multijet events and b -quark events	61
7.3	Number of QCD multijet events and b -quark events for jet reconstruc- tion with the Cone algorithm	61
8.1	Summary of all cuts applied to the $t\bar{t}$ and background events	96
8.2	Number of $t\bar{t}$ events which are left after applying the introduced cuts .	97
8.3	Number of background events which are left after applying the intro- duced cuts	97
8.4	Efficiency for background events	97
8.5	Signal to background ratios	98
8.6	Efficiency for $t\bar{t}$ events in case of an additional single or double b -tag .	99
8.7	Efficiency for background events in case of an additional single or double b -tag	100
8.8	Signal to background ratios for an additional b -tag	100
8.9	Summary of all cuts applied to the $t\bar{t}$ and background events	108
8.10	Number of PYTHIA $t\bar{t}$ and background events which are left after ap- plying the introduced cuts	108
8.11	Efficiency for $t\bar{t}$ and background events	108
8.12	Signal to background ratio	109
8.13	Cross sections for the remaining $t\bar{t}$ and QCD 6-jet background events .	110

Bibliography

- [1] B. Povh, K. Rith, C. Scholz, and F. Zetsche. *Teilchen und Kerne*. Springer-Verlag, 1997.
- [2] M. Erlebach. Studien zu Multijet Ereignissen am Tevatron, 2004. Diplomarbeit der Fakultät für Physik der Ludwig-Maximilians-Universität München.
- [3] Particle Data Group (PDG). Particle Physics Booklet, 2006. Journal of Physics G 33, 1.
- [4] U. Egede. *The search for a standard model Higgs at the LHC and electron identification using transition radiation in the ATLAS tracker*. PhD thesis, Lund University, 1997. LUNFD6/(NFFL-7150).
- [5] H. D. Politzer and S. Wolfram. Bounds on particle masses in the Weinberg – Salam model. 1979. Phys. Lett. 82B, 242-246.
- [6] M. D. Tonasse. Charged fermion masses with Yukawa coupling strength universality. 2001. hep-ph/0112187.
- [7] R. Barate et al. Search for standard model Higgs boson at LEP. *Phys. Lett. B*, 2003. CERN-EP2003-011.
- [8] M. Schmanau. Die SU(3) Color und Quark Confinement, 2003. IEKP-KA/2003.
- [9] O. Biebel. Studien der Quanten-Chromo-Dynamik mit Collider-Experimenten, SoSe 2002. Vorlesung an der LMU München.
- [10] B. R. Webber. Fragmentation and hadronization. Theory Division, CERN, 1211 Geneva 23, Switzerland.
- [11] Y. L. Dokshitzer and B. R. Webber. *Phys. Lett. B352, 451*, 1995. hep-ph/9504219.
- [12] A. Buijs. A fragmentation model applied to exclusive final states in photon-photon collisions, 1986. SLAC-PUB-4037.
- [13] T. Sjöstrand, L. Lönnblad, S. Mrenna, and P. Skands. *PYTHIA 6.2 Physics and Manual*, 2002. hep-ph/0108264.
- [14] Proton. http://zms.desy.de/e548/e550/e6025/e76/imageobject181/hermes_proton_hr_ger.jpg.

- [15] P. Hansson. The parton model, 2004. <http://www.particle.kth.se/~perh/files/partonModel.pdf>.
- [16] S. Richter. Das Quark-Parton-Modell oder die Struktur des Protons. http://www.hs.uni-hamburg.de/~st2b102/seminare/ss06/richter_folien.pdf#search=%22Parton%20Modell%22, 2006. December 2006.
- [17] R.K. Ellis, W.J. Stirling, and B.R. Webber. *QCD and Collider Physics*. Cambridge University Press, 2003.
- [18] CTEQ. <http://www.phys.psu.edu/~cteq/>.
- [19] O. Biebel. 8: QCD, Jets, Strukturfunktionen. <http://www.mppmu.mpg.de/>, WiSe 2003/2004. Vorlesungsreihe Angewandte Physik: Teilchenphysik mit höchsten-energetischen Beschleunigern (TEVATRON und LHC).
- [20] K. Ellis. Quantum Chromo Dynamics at the LHC, Lecture I: Proton structure and parton showers. <http://theory.fnal.gov/people/ellis/Talks/Frascati1.pdf#search=%22proton%20structure%20function%20LHC%22>, May 2006. Frascati Spring School.
- [21] The DØ Collaboration. Observation of the top quark. 1995. Phys. Rev. Lett. 74, 2632 - 2637.
- [22] The CMS Collaboration. Observation of the top quark production in $p\bar{p}$ collisions with the CDF detector at Fermilab. 1995. FERMILAB-PUB-95/022-E.
- [23] E. Q. Varnes. Measurements of top quark decay properties. 2006. FERMILAB-CONF-06-078-E.
- [24] V. Chekelian. Standard model physics at HERA. 2001. hep-ex/0107053.
- [25] P. Azzi. Top physics at hadronic colliders, 2006. Nordic LHC Physics Workshop.
- [26] K. Marten. Top physics capabilities at the LHC, 2004. Talk at the 6th international conference of hyperons, charm & beauty hadrons, Chicago.
- [27] M. Benke, I. Efthymiopoulos, M. L. Mangano, and J. Womersley. Top quark physics. 2000. hep-ph/0003033.
- [28] B. Abott, M. Abolins, V. Abramov, B. S. Acharya, I. Adam, M. Adams, S. Ahn, H. Aihara, and G. A. Alves. Measurement of the top quark pair production cross section in $p\bar{p}$ collisions using multijet final states. 2001. Phys. Rev. D60, (2001) 012001.
- [29] F. Rauscher. *Untersuchung des Verhaltens von Driftrohren bei starker γ Bestrahlung sowie Vermessung von Driftrohrkammern mit Hilfe von Myonen der kosmischen Höhenstrahlung*. PhD thesis, Ludwig-Maximilians-Universität, 2005.
- [30] P. Lebrun. Status of the LHC project, 2007. Talk in the MPI Kolloquium.

-
- [31] ATLAS at work, ATLAS detector components. <http://physics.bu.edu/ATLAS/ATLAS-info/aaw-component.html>.
- [32] ATLAS Collaboration. ATLAS Detector and Physics Performance – Technical Design Report, Volume I, 1999. ATLAS TDR 14, CERN/LHCC/99-14.
- [33] P. Schwemling. ATLAS electromagnetic calorimetry and performance of electron/photon detection. 2004. Eur. Phys. J C 34 (2004), page 01.
- [34] P. Krieger. The ATLAS liquid argon calorimeter. 2005. IEEE Nuclear Science Symposium Conference Record, 0-7803-9221-3/05.
- [35] I. Borjanovic, I. Efthymiopoulos, F. Fassi, P. Grenier, P. Homola, V. Kostioukhine, R. Leitner, I. Mendas, D. Pallin, D. Popovic, P. Roy, V. Simak, L. Simic, G. Skoro, and J. Valenta. Investigation of top mass measurements with the ATLAS detector at LHC. 2004. hep-ex/0403021.
- [36] S. Tapprogge. QCD at LHC with ATLAS, 2001. Talk at the 2nd Workshop on Very High Multiplicity Physics, Dubna.
- [37] ATLAS Collaboration. ATLAS Detector and Physics Performance – Technical Design Report, Volume II, 1999. ATLAS TDR 15, CERN/LHCC/99-15.
- [38] R. Bonciani, S. Catani, and M. Mangano. NLL resummation of the heavy-quark hadroproduction cross section. 1998. Nucl. Phys. B 529 (424-450).
- [39] California Institute of Technology, University of California at San Diego, University of California at Santa Barbara, and University of Colorado et. al., 1994. http://www.lns.cornell.edu/public/CLEO/CLEO3/cleo3/proposal/idtf_prop_unix.html.
- [40] J.M. Butterworth, J.P. Couchman, B.E. Cox, and B.M. Waugh. KtJet: A C++ implementation of the k_T clustering algorithm. 2002. hep-ph/0210022.
- [41] A. Gupta. Jet algorithms in Athena, 2003. ATLAS Physics Workshop; Athens.
- [42] S. D. Ellis. Successive combination jet algorithm for hadron collisions. 1993. hep-ph/9305266.
- [43] V.D. Elvira. Jet measurements at $D\bar{D}$ using a k_T algorithm. 2002. hep-ex/0209073.
- [44] B. Andrieu. Jet finding algorithms at Tevatron, 2004. XXXIV International Symposium on Multiparticle Dynamics (ISMD04), Sonoma County.
- [45] M. Martinez. CDF at IFAE, 2004. IFAE Seminar.
- [46] S. Catani, Yu. L. Dokshitzer, M. H. Seymour, and B. R. Webber. Longitudinally-invariant k_\perp clustering algorithms for hadron-hadron collisions. 1993. Nucl. Phys. B406 (1993) 187.
- [47] M. L. Mangano, F. Piccinini, and A. D. Polosa. ALPGEN, a generator for hard multiparton processes in hadronic collisions. 2003. hep-ph/0206293.

- [48] S. Catani, F. Krauss, R. Kuhn, and B. R. Webber. QCD matrix elements + parton showers. 2001. hep-ph/0109231.
- [49] F. Caravaglios, M. L. Mangano, M. Moretti, and R. Pittau. A new approach to multi-jet calculations in hadron collisions. 1998. hep-ph/9807570.
- [50] F. Caravaglios and M. Moretti. An algorithm to compute born scattering amplitudes without feynman graphs. 1995. hep-ph/9507237.
- [51] M. Mangano. Merging multijet matrix elements and shower evolution in hadronic collisions. <http://cern.ch/~mlm/talks/lund-alpgen.pdf>, 2004. presentation at Lund University.
- [52] F. Piccinini. Monte Carlo tools for LHC, 2006. Talk at the Italo-Hellenic School of Physics, Lecce.
- [53] B. Cooper. Experience with matched samples, 2004. Presentation at FNAL, University College London.
- [54] F. Krauss, 2006. Private communication.
- [55] L. Dixon. QCD at Colliders Lecture 3, 2005. Prospects in Theoretical Particle Physics, Institute for Advanced Study, Princeton, <http://www.admin.ias.edu/pitp/2005files/Lecture%20notes/dixon-3.pdf>.
- [56] J. Huston, B. Kersevan, and D. Soper. NLO event generators and cross sections, 2007. Talk at Les Houches.
- [57] S. Dittmaier, P. Uwer, and S. Weinzierl. NLO QCD corrections to $t\bar{t}$ +jet production at hadron colliders, 2007. hep-ph/070312.
- [58] H. Plochow-Besch. PDFLIB; proton, pion and photon parton density functions, parton density functions of the nucleus, and α_s calculations; User's manual. 2000. CERN-ETT/TT 2000.04.17.
- [59] J. Pumplin, D. R. Stump, J. Huston, H. L. Lai, P. Nadolsky, and W K Tung. New generation of parton distributions with uncertainties from global QCD analysis. 2002. hep-ph/0201195.
- [60] ROOT An Object-Oriented Data Analysis Framework. <http://root.cern.ch/>.
- [61] The HEPEVT standard, URL last visited: December 2006. http://cepa.fnal.gov/psm/simulation/mcgen/lund/pythia_manual/pythia6.3/pythia6301/node39.html.
- [62] Python Software Foundation. Python programming language – official website, Last visited: June 2007. <http://www.python.org/>.
- [63] The Gaudi Collaboration. <http://proj-gaudi.web.cern.ch>.
- [64] A. Brandt. Simulation and reconstruction of muons at the munich ATLAS cosmic test facility with Athena, 2003. Diplomarbeit der Fakultät für Physik der Ludwig-Maximilians-Universität München.

- [65] M. Obermaier. Integration of calibration and alignment procedures for the reconstruction of muons in the ATLAS experiment, 2005. Diplomarbeit der Fakultät für Physik der Ludwig-Maximilians-Universität München.
- [66] S. Dean and P. Sherwood. <http://www.hep.ucl.ac.uk/atlas/atlfast/>.
- [67] E. Richter-Was, D. Froidevaux, and L. Poggioli. ATLFAST 2.0 a fast simulation package for ATLAS. 1998. ATL-PHYS-98-131.
- [68] Geant 4. <http://geant4.web.cern.ch/geant4/>.
- [69] R. Mameghani. Branching ratio of fully leptonic to semi leptonic $t\bar{t}$ decays, 2006. Seminar talk at the Abteilungsseminar LS Schaile, Ludwig-Maximilians-University München.
- [70] AthenaAwareNTuple. <https://twiki.cern.ch/twiki/bin/view/Atlas/AthenaAwareNTuple>.
- [71] A. Rimoldi and A. Dell'Acqua. The full detector simulation for the ATLAS experiment: status and outlook. 2003. physics/0306086.
- [72] F. Hubaut, E. Monnier, P. Pralavorio, B. Resende, and C. Zhu. Comparison between full and fast simulations in top physics. 2006. ATL-PHYS-PUB-2006-017.
- [73] Panda monitor. <http://gridui01.usatlas.bnl.gov:25880/server/pandamon/query?mode=listtask>.
- [74] C. Clement, C. Gerber, G. Otero, M. A. Pleier, E. Shabalina, and J.-R. Vlimant. Measurement of the $t\bar{t}$ production cross-section at $\sqrt{s} = 1.96$ TeV in the electron+jets final state using a topological method, 2005. http://atlas.physics.arizona.edu/~johns/teaching/phys586/xsec_ejets_topo_note.pdf.
- [75] Atlfast Team. Jetmaker, 2005. <http://www.hep.ucl.ac.uk/atlas/atlfast/AtlfastAlgs/JetMaker.html>.
- [76] T. Sjöstrand, L. Lönnblad, S. Mrenna, and P. Skands. *PYTHIA 6.3 Physics and Manual*, 2003. hep-ph/0308153.
- [77] Update notes PYTHIA version 6.3, 2006. <http://www.thep.lu.se/~torbjorn/pythia/pythia6327.update>.
- [78] R. Brun, F. Rademakers, S. Panacek, I. Antcheva, and D. Buskulic. *ROOT Users Guide 4.08*, 2004.
- [79] S. Frixione and B. R. Webber. The MC@NLO 3.1 event generator. 2005. Cavendish-HEP-05/09.
- [80] V. Tano. *A study of QCD processes at low momentum transfer in hadron-hadron collisions*. PhD thesis, Rheinisch-Westfälische Technische Hochschule Aachen, 2001.

-
- [81] U. Baur, T. Plehn, D. Rainwater, and theory Group of the Fermi National Accelerator Laboratory. Determining the Higgs boson self coupling at hadron colliders. 2002. hep-ph/0211224.
- [82] R. Field. Minimum Bias at CDF and CMS, 2006. Talk at the CMS Min-Bias Meeting.
- [83] F. Blekman and M. Vreeswijk. Dataset and topological analysis used in the $t\bar{t} \rightarrow$ hadrons production cross section analyses using p14 data. 2004. DØnote4333.
- [84] A. Everett, A. Savin, T. Doyle, S. Hanlon, and I. Skillicorn. Event shape update, 2003. ZEUS meeting.
- [85] LHC commissioning, 2007. <http://lhc-commissioning.web.cern.ch/lhc-commissioning/>.
- [86] M. Lambacher, O. Biebel, and F. Fiedler. Generation of QCD multijet background events with ALPGEN version 2.03 and ATLFAST version 11.0.41, 2007. ATL-PHYS-INT-2007-007.
- [87] C. Posch, E. Hazen, and J. Oliver. MDT-ASD, CMOS front-end for ATLAS MDT. *ATLAS Muon Note*, 2002. ATL-MUON-2002-003.
- [88] M. Erlebach et al. Pulser test of ATLAS muon chambers. *BL Annual report 2005*, 2005.
- [89] Harvard BMC database. <http://hepldb.harvard.edu/>.
- [90] Y. Arai, R. Ball, G. Brandenburg, J. Chapman, E. Hazen, J. Oliver, and C. Posch. On-chamber readout system for the ATLAS MDT muon spectrometer. *IEEE Transactions on Nuclear Science*, Vol. 51, No. 5, 2004.
- [91] U. Tietze and C. Schenk. *Halbleiter-Schaltungstechnik*. Springer Verlag, 2002. Page 318.

Acknowledgments

It was an interesting, fruitful experience and I have learned a lot. Many people have come along with me. Some of them I want to mention and thank especially at this place.

Special thanks to my "Doktorvater" Otmar Biebel for his continuous encouragement and for always being there. He made this thesis possible and he ever gave me support, answering my many questions and spending patiently lots of time on giving me feedback and new ideas.

Thanks to Prof. Dorothee Schaile, who has always supported me since my first days at university.

I would like to thank Frank Fiedler for his patience and his answers to the lots of questions I had.

Raimund Ströhmer, Johannes Elmsheuser, Frank Fiedler, John Kennedy and above all Otmar Biebel carefully reviewed the chapters of this dissertation and gave me very helpful feedback, thanks a lot for that.

Thanks to Matthias Schott who gave me a hand on improving my fits and for many more tips which enhanced my work.

I would like to thank Cedric Serfon, with whom I have shared an office, for his assistance with Athena and for the good atmosphere in our office.

Thanks to Doris Merkl, Felix Rauscher and Ralf Hertenberger for supporting me with the pulser test.

Thanks to all my colleagues of the Lehrstuhl Schaile for a nice and fruitful time.

Britta Tiller, Matthias Schott, Raphael Mameghani, Daniela Görisch and Gabriele Reiter really became friends during my time at the Lehrstuhl Schaile. Their open and friendly disposition (and the small tea breaks) enhanced a lot the working atmosphere and brought more fun into my work. Thanks a lot for your encouragement, for listening and discussing and for always cheering me up again.

Frau Franz, thank you for your encouragement and our small "lunchtime talks".

Many thanks to Frank Berghaus who has reprocessed my background events and who has kindly provided me his joboption files. He rode to rescue by making tricky problems and questions more understandable.

I would also like to thank Prof. Martin Faessler who acts as second evaluator of this thesis.

Thanks particularly to the one without whom this would have never been possible, my husband Michael. Thank you for your love and patience.

I am deeply grateful to my mom Inge, who has always believed in me. I rely on your support and your wisdom up to this day. You live on in our hearts.

Thank you to my family for their support, above all my father Dieter, who has continuously incited me to do my best. Thanks to Heidi and Franz for listening and being there at all times.

Finally, I would also like to say thanks to my friends. They stood by my side even in hard times.

Curriculum Vitae

Marion Lambacher
LMU Department für Physik
Am Coulombwall 1
85748 Garching
Email: Marion.Erlebach@physik.uni-muenchen.de

Personal information

Place of birth: Pfarrkirchen
Date of birth: 13.06.1979
Marital status: Married
Nationality: German

Education

1985 – 1989: Grundschule Pfarrkirchen
1989 – 1998: Gymnasium Pfarrkirchen
1998 – 2004: Study of physics at the Ludwig-Maximilians-Universität München
Diploma thesis at the DØ experiment: Studien zu Multijet Ereignissen am Tevatron

Doctorate

Since 2004 at the Ludwig-Maximilians-Universität München
Fields of research: Top quark physics and Quantum Chromo Dynamics
Dissertation at the ATLAS experiment: Study of fully hadronic $t\bar{t}$ decays and their separation from QCD multijet background events in the first year of the ATLAS experiment

Working experience

2004 – 2005: Cooperation at the cosmic ray measurement facility of the Ludwig-Maximilians-Universität München
2005 – 2006: Tutor for students of the FII practical at the Ludwig-Maximilians-Universität München

Memberships

2003 – 2005: Deutsche Physikalische Gesellschaft
Since 2003: DØ collaboration
Since 2004: ATLAS collaboration
Since 2004: Graduiertenkolleg Particle Physics at the Energy Frontier of New Phenomena
Since 2005: International Max Planck Research School (IMPRS) on Elementary Particle Physics

Languages

German: Mother language
English: Professional knowledge
French: Advanced knowledge
Italian: Basic knowledge
Latin: Großes Latinum

